

HIRDLS

TC-LOC-12

HIGH RESOLUTION DYNAMICS LIMB SOUNDER

Originator: Howard E. Morrow

Date: 24 May 96

Subject/Title: **Comprehensive Optical Performance Analysis**

Description/Summary/Contents:

1.

Keywords: [keyword 1], [keyword 2], etc

Purpose of this Document:
(20 char max.)

Reviewed/Approved by:			
Date (yy-mm-dd):			

**Palo Alto Research Laboratory, Cage Code 65113
Lockheed Martin Missiles & Space
3251 Hanover Street
Palo Alto, CA 94304-1191
United States of America**

EOS

Table of Contents for
TC-LOC-12
HIRDLS Comprehensive Optical Performance Analysis
(for the HIRDLS Imager) ?

1.0 Introduction	8
1.1 Purpose and scope	8
1.2 Related documents	8
2.0 Interface to the STH (int2sth.doc).....	9
2.0.1 Scan Mirror.....	9
2.0.2 Detector	9
2.0.3 Space View Aperture	9
2.1 Annotated XY projection layout	10
3.0 Prescription(s) & Layout (presc.doc).....	12
3.1 Coordinate system for the optical design.	12
3.2 Description of the optical design.....	12
3.2.1 Element by element location in IRCF global coordinates.	12
3.2.2 Element by element location in scan mirror global coordinates.	12
3.2.3 Element by element prescription and clear apertures	12
3.3 Axial ray traces.....	12
3.3.1 Axial ray in instrument global coordinates.....	12
3.3.2 Axial ray in element local coordinates	12
3.3.3 Axial ray in scanner global coordinates.....	12
3.4 Annotated graphics of full optical assembly, several views	12
3.4.1 Oblique view	12
3.4.2 Close-up of chopper area.....	12
4.0 First Order Properties (1st-ord.doc).....	13
4.1 Focal length, method, by channel	13
4.1.1 Method of computing focal length	13
4.1.2 Focal length of the HIRDLS imager.....	14
4.2 F/number for each channel.....	15
4.2.1 Method of computing F/number.....	15
4.1.2 The imager exit pupil	15
4.1.3 Imager F/number for each channel	16
4.3 Object FOV angles, channel by channel	17

4.4 Optical sub groups and selected elements.....	18
4.5 Aperture and f/nbr of parent off-axis mirrors.....	18
4.5.1 Primary mirror, full aperture parent.....	19
4.5.2 Secondary mirror, full aperture parent.....	19
4.5.3 IFC mirror, full aperture parent	20
5.0 Pupils, Fields, and their Images (pup&fld.doc)	22
5.1 Quality and location of the image of each <i>pupil</i> on its next conjugate	22
5.1.1 The image of the PDB on the ILS	23
5.1.2 The image of the ILS on the SAS	24
5.1.3 The image of the ILS on the PDB	25
5.2 Quality and location of the image of each <i>field</i> on its next conjugate	25
5.2.1 The image of FS1 on FS2	26
5.2.2 Image of IFOVs on FS1, & FS2	27
5.3 Image of the SAS onto the PDB	28
5.3.1 SAS footprints projected into the PDB	29
5.3.2 Entrance pupil area, channel by channel	29
5.4 Diffraction aspects of the pupil and field images	30
5.5 Beam clearances near aperture edges.....	Error! Bookmark not defined.
6.0 Footprints and Apertures (footpr.doc).....	31
6.1 Define critical, maximum, and mechanical apertures	31
6.1.1 Mechanical aperture	31
6.1.2 Maximum clear aperture	31
6.1.3 Critical clear aperture	31
6.1.4 Apertures and performance specifications.....	31
6.2 Maximum and Critical clear apertures, surface by surface.....	31
6.2.1 Scan Mirror.....	32
6.2.2 Primary Mirror.....	32
6.2.3 Secondary Mirror.....	33
6.2.4 Germanium lens 1	33
6.2.5 Fold Mirror	34
6.2.6 Germanium lens 2	35
6.2.7 Vacuum window	35
6.2.8 Cold Shield	36
6.3 Beam Geometry at FS2 and Warm Filters.....	36
6.4 Beam Geometry at Cold Filters	38
6.5 Angle-of-incidence histograms on selected surfaces.....	38
6.6 Footprint on main box aperture	38

7.0 Chopper Waveform (chopwavf.doc)	40
7.1 Method of illumination simulation	40
7.1.1 Uniformity of Illumination	40
7.1.2 Relative amplitude of illumination.....	40
7.1.3 Extraction of the signal profiles	40
7.1.4 Plot of the chopper signal profiles.....	41
.....	43
8.0 Image distortion and detector specification(distort.doc)Error! Bookmark not defined.	
8.1 Detector geometry	Error! Bookmark not defined.
8.1.1 Method of determination	Error! Bookmark not defined.
8.1.2 Ideal detector layout	Error! Bookmark not defined.
8.1.3 Tabulated detector geometry.....	Error! Bookmark not defined.
8.1.4 Earth limb curvature	Error! Bookmark not defined.
9.0 Polarization Raytrace analysis (polariz.doc)	50
Coating specifications (source), h&k for metal	50
Method	52
Axial ray surface by surface, ch 2.....	52
Axial ray each channel at detector.....	52
Pupil polarization aberration, somehow	52
10.0 Ghost Images (ghosts.doc).....	53
10.1 The ghost image geometric concentration ratio	53
10.1.1 Relative transmittance of the ghost beam.....	54
10.1.2 Ghost watts on the detector	54
10.2 Two surface ghosts	54
10.2.1 Selected examples 2 surface ghosts.....	55
10.2.2 Tabulated summary of 2 surface ghosts.....	57
10.3 Selected ghosts from channel 19	59
11.0 LOS vector sensitivity table (los-sens.doc)	62
11.1 Clarification of coordinate directions.....	62
11.2 Element LOS sensitivities to solid body perturbations in IRCF coordinates	62
11.3 Element LOS sensitivities to solid body perturbations in LOCAL coordinates	64
11.3 Selected group LOS sensitivities to solid body shifts in IRCF coordinates....	65
12.0 Diffraction image performance (difperf.doc).....	67

12.1 Introduction	67
12.1.1 Deviation from isoplanatism	67
12.2 Wavefront error and Strehl ratio	69
12.2.1 Through-focus WFE & Strehl ratio behavior of selected channels	70
12.3 MTF at detector Nyquist frequency, with through-focus data.....	73
12.3.1 Relevance of MTF to HIRDLS	73
12.3.2 Computation and display of through-focus MTF data	73
12.4 Vertical Response Profile (VRP) & derived performance data.....	77
12.4.1 Interpretation of the ITS Vertical response requirement sections 3.3.1 and 3.3.3.1	77
12.4.2 Baseline Computed VRP data.	78
12.5 Through-focus VRP data	86
12.5.1 Method of computation (in OPTIMA)	86
12.5.2 Sample through-focus VRP data plots (Channel 10).....	86
12.5.3 FWHM through focus plots for channels 2, 10 and 21	88
12.5.4 Slope at FWHM through focus for channels 2, 10 and 21	89
12.5.5 Relative integrated response under FWHM through focus for Ch. 2, 10 and 21.....	90
12.5.6 Relative integrated response through focus within $\pm .75$ km for Ch 2, 10, & 21	92
12.5.7 Relative integrated response through focus within ± 1.0 km for Ch 2, 10, & 21	93
12.5.8 Relative integrated response through focus for heights ≥ 2.0 km.	94
12.5.9 Tabulated through-focus VRP data for all channels.	94
12.6 VRP stability (ITS 3.3.3.1).....	95
12.6.1 Selected VRP stability “difference data” plots.	95
12.6.2 VRP stability: peak and valley projections.	97
12.6.3 VRP stability focus range for all channels.....	99
13.0 Thermally induced focus error	100
13.1 Telescope elements.....	100
13.1.1 Primary and secondary mirrors.....	100
13.1.2 Two spaces.....	101
13.2 Relay section	101
13.2.1 Germanium elements.....	101
13.2.2 Three spaces	101
13.3.3 Special problem of the dewar assembly (L2 to detector)	102
13.3 Full system with thermally stabilized lenses	102
14.0 Element Null test Configurations (nulltest.doc)	103
14.1 Null testing	103
14.2 Off-axis parabolas: the imager primary, and the IFC mirror	103

14.3 The secondary mirror	103
14.4 Germanium lens 1	103
14.5 Germanium lens 2	105
14.6 The Space View toroid relay mirror	106

Throughput (?) *not assigned*

Coating efficiencies with tolerances

Material coefficients of absorption

Excel spreadsheet of throughput, best, expected, and worst cases

Element specifications (?) *not assigned*

Element drawings with all optical specifications for fab.

IFC Characteristics and Performance

IFC mirror

Image at entrance to BB

Appendix: analysis procedures and macros *not assigned*

Descriptions of analysis procedures

Exhibition of annotated Macros

1.0 Introduction

1.1 Purpose and scope

This document will serve several purposes. It will show in detail that all items in the ITS related to optical performance are met (or not), and indicate margin where applicable. The method used to determine the various performance parameters are explained.

The section on diffraction imager performance shows how conventional measures of performance compare to the Vertical Response Profile requirement in the ITS. These data are taken through focus, giving a top level insight to their sensitivity to focus related errors. There is a special section on thermally induced focus error which may shed new light on the operational stability problem.

Some of the data herein form the performance baseline to be applied in the tolerance budget development. Thus TC-LOC-140 will refer to parts of this document.

The foundations for some of the design details given in TC-LOC-139 are found in this document. For example beam footprints are shown which will justify maximum and critical clear aperture assignments among the optical elements.

The optical engineer will appreciate seeing how the various pupils and fields image upon one another. Performance assurance, as well as optical engineers will find the section on null tests of the lenses and mirrors useful.

Distortion, and the ideal detector map, will be useful to the detector manufacturer.

1.2 Related documents

SP-HIR-13

SP-LOC-139

TC-LOC-140

2.0 Placement and Impact on Structures (int2sth.doc)

The locations of three key elements or features relative to the other structures are controlled by specification of their coordinate values in the Instrument Reference Coordinate Frame (IRCF) (See ITS, 3.1.3). All the optical elements are so disposed within the IRCF that all X,Y,Z coordinate values are positive.

2.0.1 Scan Mirror

The location of the scan mirror at 0° elevation and azimuth is specified and controlled by the IICD, SP-HIR-214, Paragraph TBD, and are shown in figures 2.1-1 and 2.2-1 below for illustrative purposes. The values are also in the BDD, (TC-HIR-99H) Part II, AACCA.

2.0.2 Detector

The detector is located by extending the axial ray 100 mm beyond the detector plane until the ray intersects the Cyrovac Dewar Interface Point (C/D IP). The intersection is achieved by location and orientation of the fold mirror. The location of the C/D IP is specified and controlled by TBD. The location values have been informally agreed, and are in the BDD (TC-HIR-99H) Part I, Drawing under section 3. These values are also found below in figures 2.1-1 and 2.2-1.

2.0.3 Space View Aperture

The space view aperture is a hole in the cold radiator wall of the STH. The center of the aperture is not coincident with the space view axial ray due to aberration in the illumination pattern. The location of this STH hole has been determined by the optical design. The location values have been informally agreed, and are in the BDD (TC-HIR-99H) Part I, Drawing under section 3. The values are also found below in figures 2.1-1 and 2.2-1.

2.0.4 Hotdog Aperture

The hotdog aperture (shaped like curved hotdog!) is located on the hotdog aperture plane, the large rectangle shown in the figures below. The aperture is not shown due to limited capability of the optical analysis software. However the hotdog aperture is specified to clear by 3 mm (TBR) the envelope of all rays defined by the PDB over a field defined by FS1, for the full scan mirror Field Of Regard (FOR) as specified in the ITS (3.5.1.1& 3.5.2.1). The hotdog aperture does not accommodate the IFC view.

2.1 Annotated XY projection layout

The figure 2.1-1 below shows the full optical assembly with only the axial ray for each path. The view is looking along on the -Z axis. Each of the four elements or features are annotated along with coordinate locations for three.

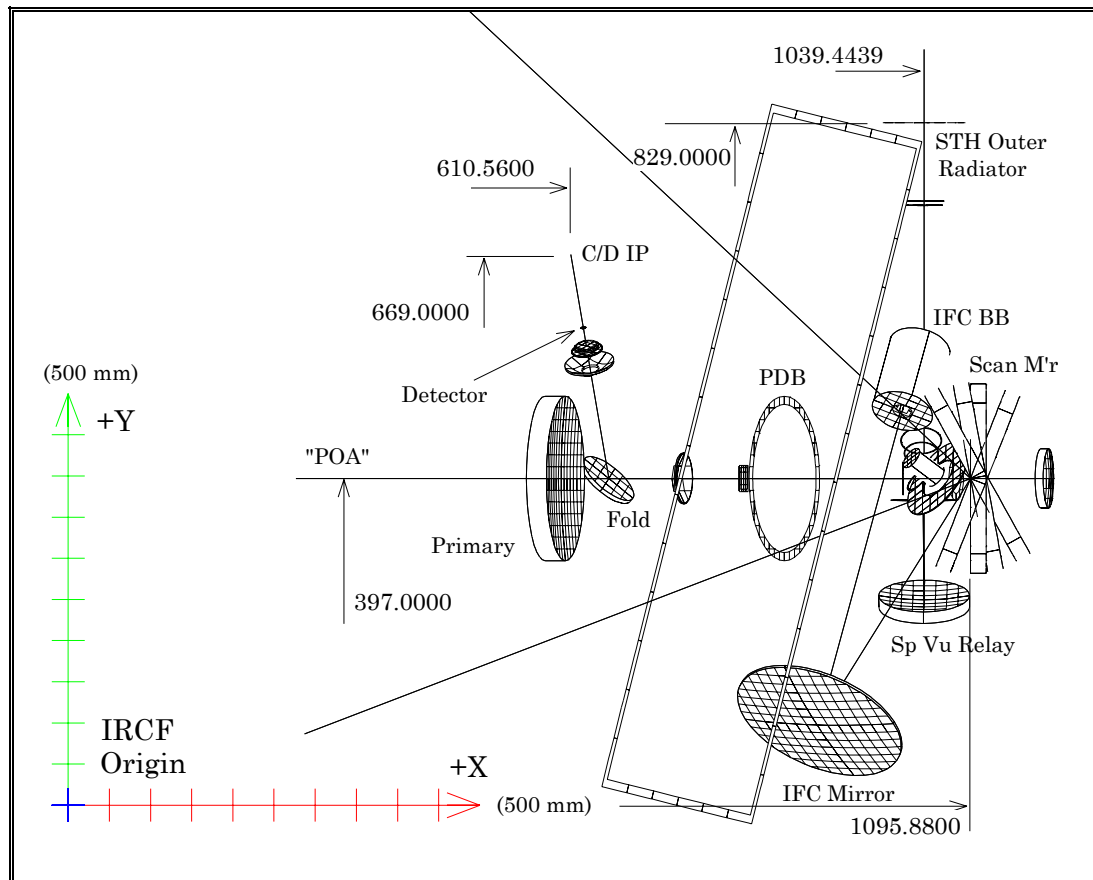


Figure 2.1-1 XY layout showing the 4 major interfaces to structures

The axial ray is shown extended 100 mm beyond the detector where it intersects the C/D IP. The scan mirror is shown with three angles superimposed on the zero degree angle. The X and Y dimensions from the IRCF origin to the scan mirror are shown. The dimensions to the space view hole (identified as the STH Outer Radiator) are also shown. Finally, the large tilted rectangle represents the hotdog plane, but is shown without dimensions.

2.2 Annotated YZ projection layout

The figure 2.2-1 below also shows the full optical assembly with only the axial ray for each path. The view is looking along the +X axis. Each of the four elements or features are annotated with coordinate locations for three.

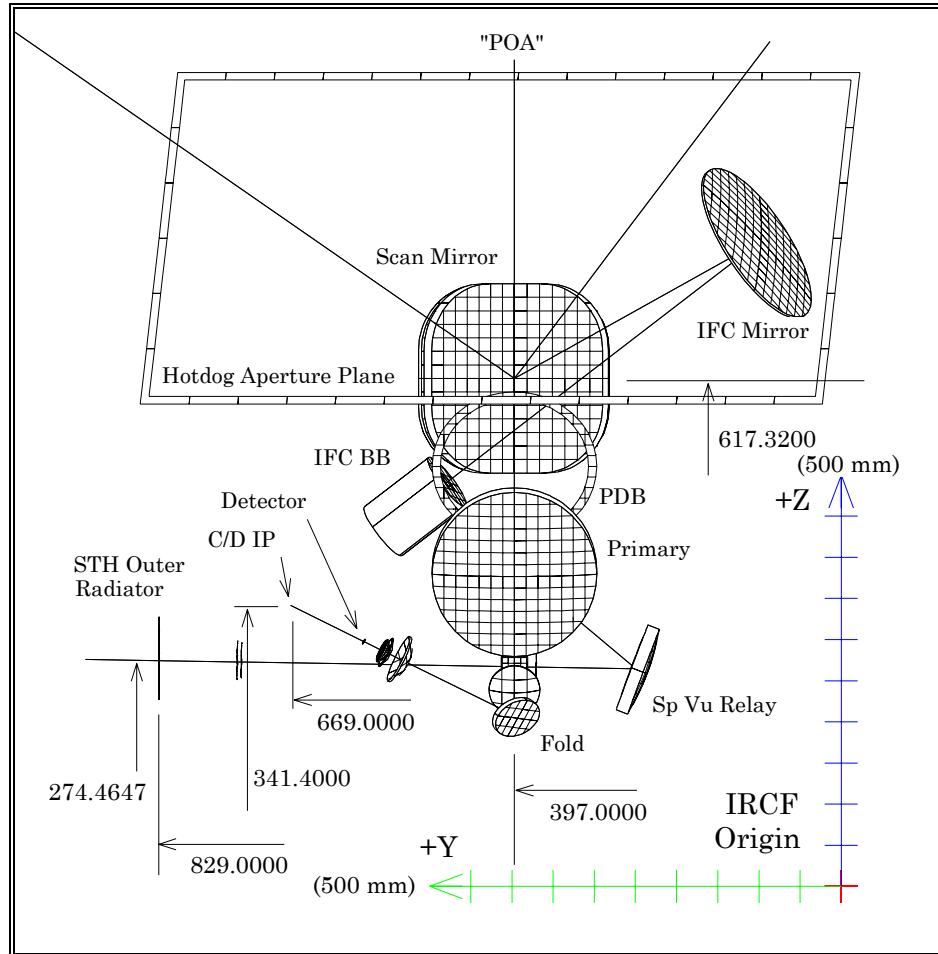


Figure 2.2-1 YZ layout showing the 4 major interfaces to structures

The axial ray is shown extended 100 mm beyond the detector where it intersects the C/D IP. The Y and Z dimensions from the IRCF origin to the scan mirror are shown. The dimensions to the space view hole (identified as the STH Outer Radiator) are also shown. Finally, the large parallelogram represents the hotdog plane, but is shown without dimensions.

3.0 Prescription(s) & Layout (presc.doc)

3.1 Coordinate system for the optical design.

text from 139

3.2 Description of the optical design

text. various ways to describe...

3.2.1 Element by element location in IRCF global coordinates.

table from 139

3.2.2 Element by element location in scan mirror global coordinates.

new table

3.2.3 Element by element prescription and clear apertures

table

3.3 Axial ray traces

definition of axial ray (from 139)

3.3.1 Axial ray in instrument global coordinates

table

3.3.2 Axial ray in element local coordinates

table

3.3.3 Axial ray in scanner global coordinates

table

3.4 Annotated graphics of full optical assembly, several views

3.4.1 Oblique view

ins a new goat

3.4.2 Close-up of chopper area

all new, showing motor, rad trap, FS1, Chopper

4.0 First Order Properties (1st-ord.doc)

Two first order properties of the HIRDLS imager are specified in the ITS. These are tabulated under the following paragraphs:

Property	ITS Paragraph	Req'ment	TCLOC12 Paragraph	Value	Complies?
System Aperture Size	4.4.3.1.2	$>.018 \text{ m}^2$	5.3.2		Yes
Focal Length	4.4.3.2	$247 \pm 3 \text{ mm}$	4.1	245.4 mm	On axis

There are several other first order properties useful to other HIRDLS activities. These are tabulated under the following paragraphs:

Property	Significance	TCLOC12 Paragraph
Image F/number	Radiometric performance	4.2
Object FOV angles	Test planning	4.3
Optical Sub-groups	Testing, engineering	4.4
Parent F/numbers	Optical Engineering; cost driver	4.5

4.1 Focal length, method, each channel

4.1.1 Method of computing focal length

Since HIRDLS is a multi-channel relayed system without rotational symmetry, and with image distortion, the focal length varies with channel number, and is slightly different in the y and x planes.

Of the various methods of computing focal length or EFL, the “plate scale” method is appropriate for the HIRDLS imager because it is an off-axis system. Ray heights h on the image plane are noted for small input angles i , and the focal length f is found from the relation $f = h/\tan(i)$.

For each channel then, a channel axial ray was traced as a local zero reference. A small angle chief ray is then traced in each of the x and y directions 100 microradians away from the axial ray, and the intercepts hx and hy from the reference ray noted in the focal plane. The x and y focal lengths (EFL's) are noted in table 4.1-1 from $f_{x,y} = h_{x,y} * 10^4$.

4.1.2 Focal length of the HIRDLS imager

The following table is a compilation of the HIRDLS imager focal length computed using the method described above. The values should be compared to the ITS 4.4.3.2 requirement of 247 mm \pm 3 mm. In the center of the Composite Field of View (CFOV), Channel 2 does meet the specification at 245.4 mm.

Table 4.1-1 The Imager focal length for each channel.

CHANNEL	Y-EFL	X-EFL
1	243.485	245.218
2	245.398	245.398
3	246.245	245.210
4	245.609	244.581
5	242.124	243.277
6	240.151	244.580
7	237.982	239.352
8	230.911	236.893
9	234.325	243.331
10	230.877	236.862
11	237.945	239.311
12	241.934	240.593
13	241.914	240.569
14	244.032	240.942
15	244.590	240.443
16	243.090	238.956
17	237.970	236.133
18	237.942	236.108
19	243.057	238.918
20	244.546	240.384
21	243.957	240.838
22	232.590	240.639

The 6.3% variation in EFL is due to distortion of the image. While harmless, it will need to be considered during IFOV calibration.

4.2 F/number for each channel

4.2.1 The imager exit pupil

The figure below shows the real-ray exit pupil and the paraxial exit pupil. There are 9 circles of dots representing ray intercepts in the exit pupil. The 9 circles are traced from the corners and sides of the CFOV, plus 1 from the center. If there were no pupil aberration, the dots would lie closer around the dashed circle which represents the paraxial exit pupil.

Thus, the real marginal rays (rays grazing the SAS aperture) are faster (lower F/number) than the paraxial prediction.

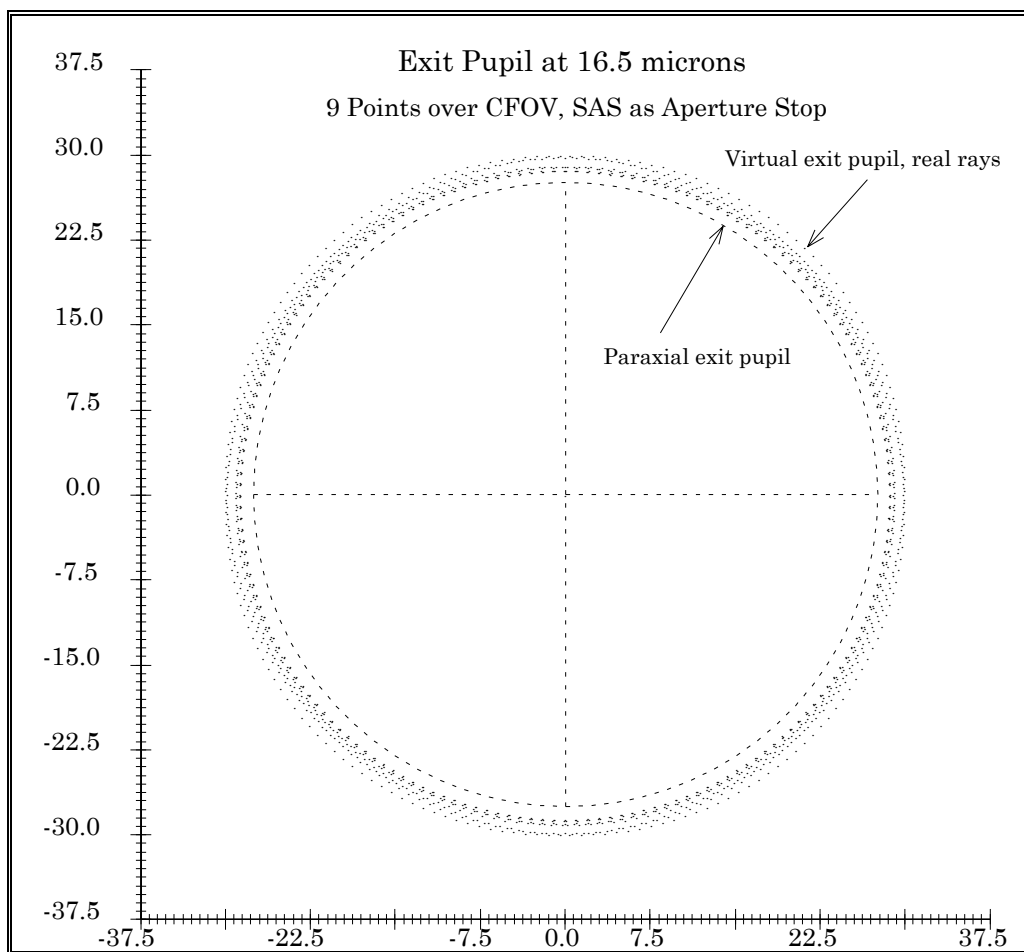


Figure 4.2-1 The imager real-ray exit pupil is reasonably well-formed over the CFOV

4.2.2 Method of computing F/number

Using paraxial methods, the imager F/number is 1.52 for all channels. This is determined by the program recognizing that the SAS aperture is the system aperture stop, and

applying a pseudo-paraxial ray method of raytrace (real rays at small apertures and angles for better accuracy in the presence of aspherics, tilts, decenters, etc.). However, full aperture real rays do not follow the paraxial prediction, so the full aperture F/number has been computed and tabulated for each channel (table 4.2-1 below).

The real F/numbers were computed separately in the y-plane and x-plane directions. By noting the full angle of a pair of rays in each plane, the half-cone angle u was obtained, and the F/number F computed from the definition $F = 1/(2*\tan(u))$.

4.2.3 Imager F/number for each channel

Using the real ray method described in 4.2.2, the following table of imager F/numbers is obtained.

Table 4.2-1 X and Y real-ray F/numbers for the Imager

CHANNEL	Y-F/#	X-F/#
1	1.443	1.444
2	1.445	1.445
3	1.443	1.444
4	1.439	1.442
5	1.432	1.440
6	1.438	1.442
7	1.435	1.433
8	1.429	1.431
9	1.431	1.439
10	1.428	1.430
11	1.435	1.432
12	1.438	1.433
13	1.438	1.433
14	1.439	1.433
15	1.437	1.432
16	1.433	1.431
17	1.426	1.428
18	1.425	1.428
19	1.432	1.430
20	1.436	1.431
21	1.436	1.431
23	1.417	1.432

4.3 Object FOV angles, channel by channel

The channel layout is specified in figure 4.5.1-1 in the ITS, in terms of kilometers. At a distance of 3000 km (ITS 3.3.1), chief rays from the centers of each channel produce field angles as listed in table 4.3-1 below. Channel 0 is the chief ray angle from any corner of the CFOV, and channel 23 is the alignment channel.

Table 4.3-1 Channel by channel object field angles

CHANNEL NUMBER	Y ANGLE		X ANGLE		R ANGLE	
	DEG	MRAD	DEG	MRAD	DEG	MRAD
0	0.525	9.17	0.525	9.17	0.743	12.96
1	-0.172	-3.00	0.000	0.00	0.172	3.00
2	0.000	0.00	0.000	0.00	0.000	0.00
3	0.172	3.00	0.000	0.00	0.172	3.00
4	0.344	6.00	0.000	0.00	0.344	6.00
5	0.516	9.00	0.000	0.00	0.516	9.00
6	-0.344	-6.00	0.000	0.00	0.344	6.00
7	-0.344	-6.00	0.430	7.50	0.550	9.60
8	-0.516	-9.00	0.430	7.50	0.671	11.72
9	-0.516	-9.00	0.000	0.00	0.516	9.00
10	-0.516	-9.00	-0.430	-7.50	0.671	11.72
11	-0.344	-6.00	-0.430	-7.50	0.550	9.60
12	-0.172	-3.00	-0.430	-7.50	0.463	8.08
13	-0.172	-3.00	0.430	7.50	0.463	8.08
14	0.000	0.00	0.430	7.50	0.430	7.50
15	0.172	3.00	0.430	7.50	0.463	8.08
16	0.344	6.00	0.430	7.50	0.550	9.60
17	0.516	9.00	0.430	7.50	0.671	11.72
18	0.516	9.00	-0.430	-7.50	0.671	11.72
19	0.344	6.00	-0.430	-7.50	0.550	9.60
20	0.172	3.00	-0.430	-7.50	0.463	8.08
21	0.000	0.00	-0.430	-7.50	0.430	7.50
23	0.688	12.00	0.000	0.00	0.688	12.00

4.4 Optical sub groups and selected elements

It is of occasional interest to know the magnification, focal length, or F/number of internal sub-groups within the imager. As an example, the germanium relay lenses form a stand-alone optical system with local object, image, magnification, focal length, etc.

The first order parameters in these subgroups find application in optical engineering, internal radiometry, sub-system testing, and numerous other uses.

The table below is an attempt to compose this information in an orderly format.

Table 4.4-1 First-order parameters of selected optical sub-groups

Sub group	Object	Stop	Image	Mag.	EFL	F/number
Primary	3000 km	PDB	FS1	Zero	450.3 ^{1,4}	2.477
Secondary	FS1	ILS	FS2	-2.85	104.1 ^{2,5}	7.479
Pri & Sec	3000 km	ILS	FS2	Zero	1282 ¹	7.479
Pri & Sec	PDB	FS1	ILS	-.213	1282 ¹	9.741
L1	ILS	FS2	SAS	-.631	140.6 ³	60.85 _y & 23.0 _x ⁶
L1 & L2	FS2	SAS	Detect	-.191	60.5 ¹	1.445
Sec, L1 & L2	FS1	SAS	Detect	+.545	276.9 ¹	1.445
Pri, Sec & L1	PDB	FS2	SAS	+.133	3775 ¹	60.64 _y & 22.9 _x
L2	-	-	-	-	31.7 ³	-

Notes:

Magnification is (image height)/(object height) determined from real chief ray trace close to the axial ray.

F/numbers for square aperture stops use the inscribed ellipse to define the marginal ray.

1. EFL determined from real ray traced from infinity at low angle.
2. EFL determined from pseudo-paraxial data, based on real rays.
3. EFL determined from thick lens power formula.
4. Vertex EFL of primary is 430 mm. Quoted value is for actual offset element.
5. Vertex EFL of secondary is 97.5 mm. Quoted value is for actual offset element.
6. F/number on SAS with FS2 envelope (no individual masks) ~ F/6.4

4.5 Aperture and f/nbr of parent off-axis mirrors

The two aspheric mirrors in the imager (primary and secondary), and the IFC mirror may be fabricated from their parents, or turned on a lathe as subaperture pieces. Even in the latter case, the vendor must swing the full aperture. The following three sections offer a quick look at the geometry involved.

4.5.1 Primary mirror, full aperture parent

The full aperture parent for the imager primary mirror is shown as 590 mm in figure 4.5-1 below. This diameter allows an 8 mm margin from the outer edge of the finished mirror to the edge of the parent. At the focus, a full aperture test requires accommodating an F/0.729 beam. Since the diameter of the finished mirror is 200 mm, a subaperture test could be performed at a much more tractable F/2.15.

The layout in the figure suggests several null test geometries because there is no aberration at the focus. The test geometries vary depending on whether the mirror is “seen” in double or single pass, and where the source is.

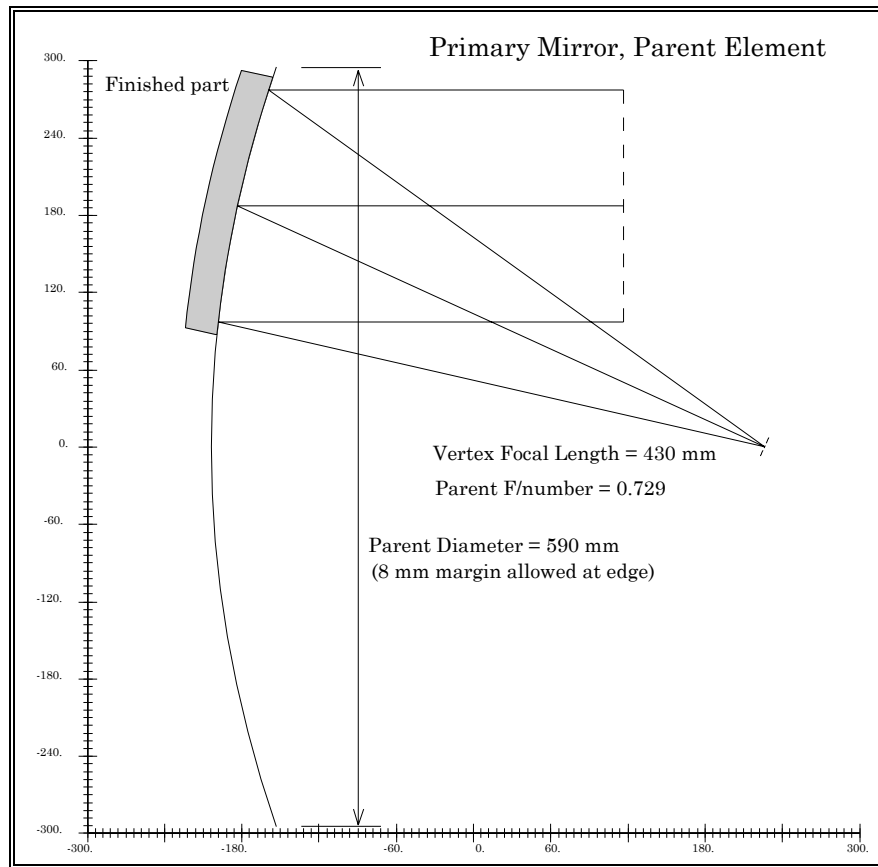


Figure 4.5-1 The parent parabola for the imager primary is 590 mm diameter at F/0.73

4.5.2 Secondary mirror, full aperture parent

As the secondary mirror is an ellipsoid, the test geometry is point to point where the points are the foci of the ellipse. This is the classical stigmatic (aberration free) null test for ellipsoid. As figure 4.5-2 below shows, the test should be feasible without obscuration of the finished mirror. If the full aperture of the parent is tested, the F/numbers at the near and far foci are F/0.619 and F/1.857 respectively. The parent, at a

diameter of 210 mm, has a radial margin of 6.1 mm beyond the outer edge of the required finished mirror.

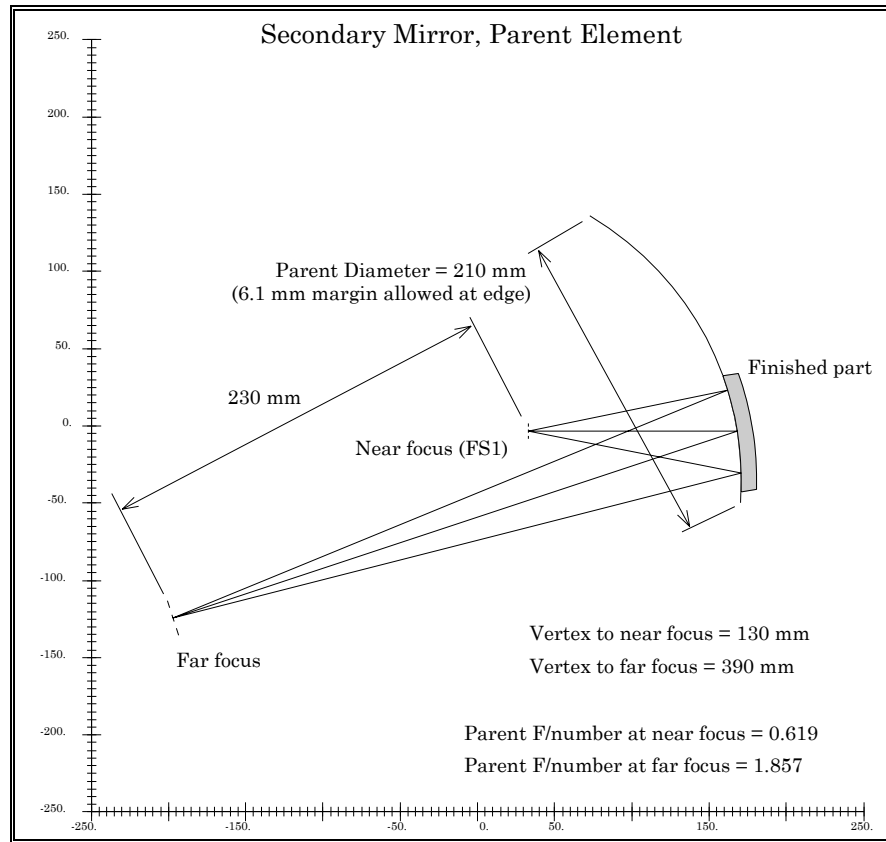


Figure 4.5-2 The parent ellipsoid for the imager secondary is 210 mm diameter

4.5.3 IFC mirror, full aperture parent

The IFC mirror is an off-axis parabola optically quite similar to the imager primary. As shown in figure 4.5-3 below, the parent diameter is 530 mm which includes a 5 mm edge margin beyond the finished mirror. While full aperture testing would require handling an F/0.907 beam, the subaperture test of the finished mirror, at 210 mm diameter, is much more tractable at F/2.3.

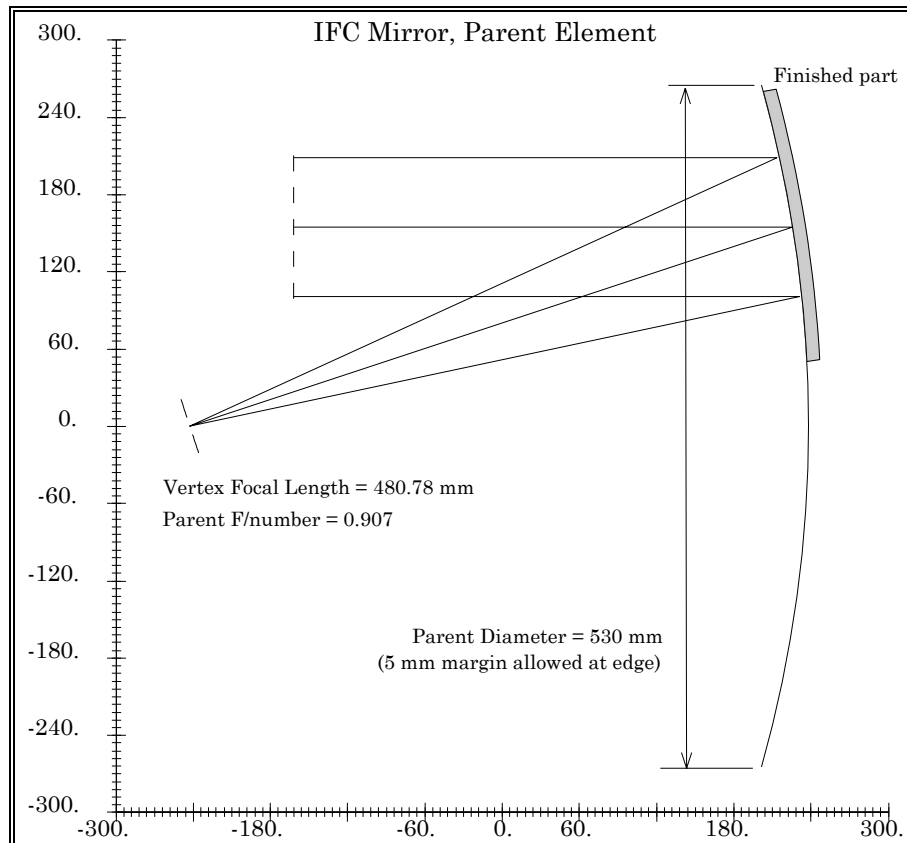


Figure 4.5-3 The parent parabola for the IFC Mirror is 530 mm diameter at F/0.91

5.0 Pupils, Fields, and their Images (pup&fld.doc)

The HIRDLS imager is a *relayed* optical system. That is, there are several pupils (images of the SAS), and several fields (images of the object space). The same is also true of the Space View path, and of the IFC path. The nature of the fields and pupils in the space view path is covered in TC-LOC-11, and is not repeated here. (See section XX in this report for the IFC path.)

In HIRDLS, as well as in other sensitive infrared radiometers, the pupil and field reimaging plays a special role. There is an aperture stop or mask at each pupil and field, with the detectors being the final field stops. As light proceeds into the system, each pupil aperture it encounters is physically smaller than the image of the previous pupil, and the aperture there clips off the image of the illumination from the edge of the previous pupils' aperture. This clipping aperture is called the Lyot stop of the previous aperture. For the HIRDLS imager (as well as for the Space View path), Lyot stopping is implemented at the ILS and the SAS. This performs a critical function for Out of Field straylight control in the imager (see TC-OXF 43 & 48 for details).

All of these features are displayed in the graphics and text in the following sections.

5.1 Quality and location of the image of each *pupil* on its next conjugate

The sizing of each aperture stop is driven by conflicting goals. One is the desire to keep them small to avoid a runaway oversize of the front PDB aperture and associated optical elements. But there is also the need to accommodate geometric aberration, alignment tolerance, and to minimize diffraction leakover, all tending to increase the sizes of the upstream apertures.

Between each pair of aperture stops there is one field stop. The size of this stop also plays an important role as it is the aperture stop controlling the F/number of image formation of the upstream aperture stop edge onto the downstream aperture rim. Larger field stops admit more geometric aberration, while smaller field stops cause more diffraction spreading.

5.1.1 The image of the PDB on the ILS

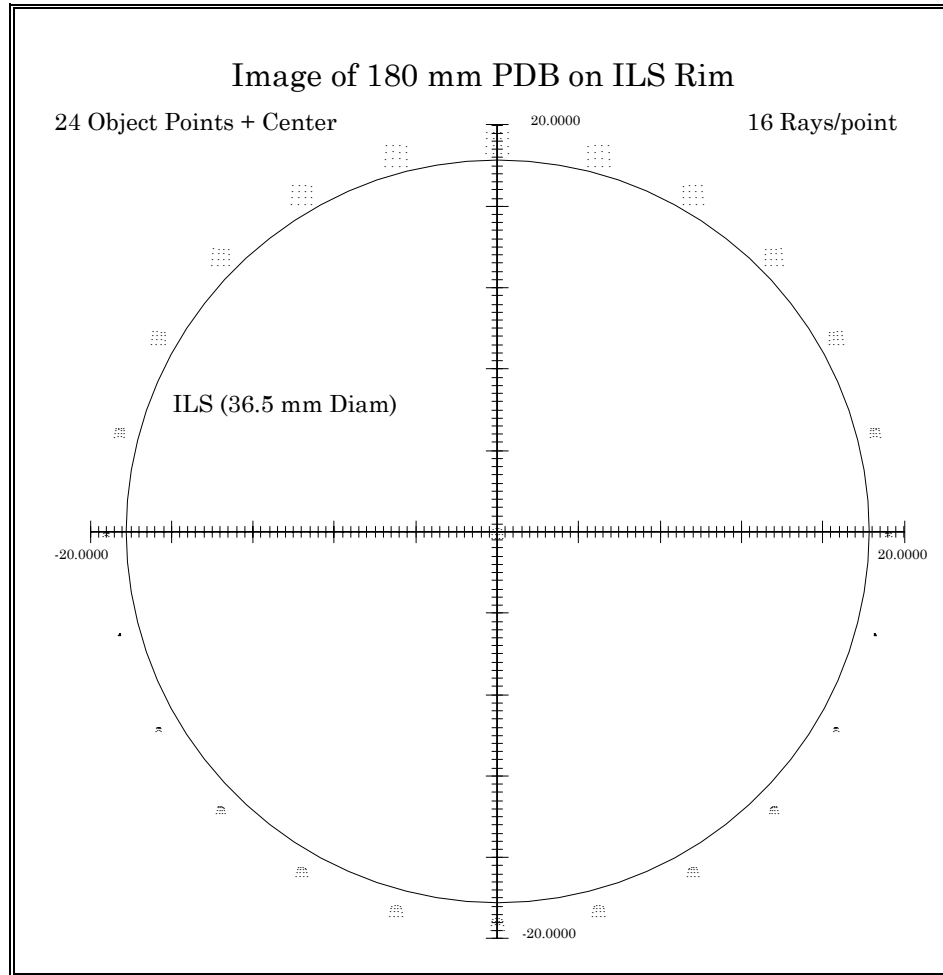


Figure x.x.x 24-point image of the edge of the PDB onto the rim of the ILS

The figure above shows the images of 24 points from around the edge of the PDB onto the rim of the ILS. The aperture for each of the points is the 10 mm square FS1. Thus, some of the images are themselves square due to local focus error.

The “best” image of the PDB is tilted with respect to the ILS, and not quite in best focus in the center of the ILS, with the result that the top and bottom of the image is out of focus by different amounts as seen.

As there is less clearance at the top images than at the bottom images, it may be required that the ILS be slightly recentered to optimize the clearance.

5.1.2 The image of the ILS on the SAS

The image of the ILS edge is formed onto the SAS rim by the germanium lens L1. The image has substantial spherical aberration, but also just the right amount of coma to fold the aberrated rays away from the SAS edge, to the far side of each chief ray intercept. This elegantly permits tight relative sizing between the SAS edge and the ILS image.

This is shown dramatically in figure x.x.x below, where the images of 24 ILS edge points are plotted.

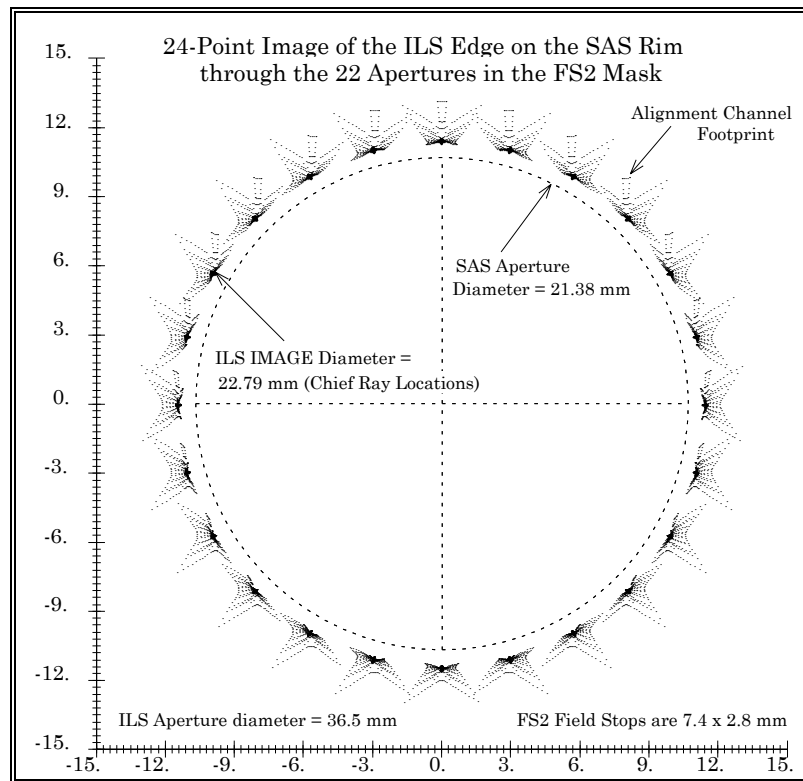


Figure x.x.x The geometric image of the SAS edge clears the ILS edge by 0.7 mm

The geometric footprints shown are the composite formed through all 22 apertures of FS2 (including the alignment aperture, see note on figure). Only the outlines of the FS2 aperture edges were traced - no interior rays were traced.

5.1.3 The image of the ILS on the PDB

Figure x.x.x below shows the reverse of figure x.x.x above. Here rays are traced backwards from 24 points around the edge of the ILS, through FS1 as the aperture stop, and plotted onto the plane of the PDB.

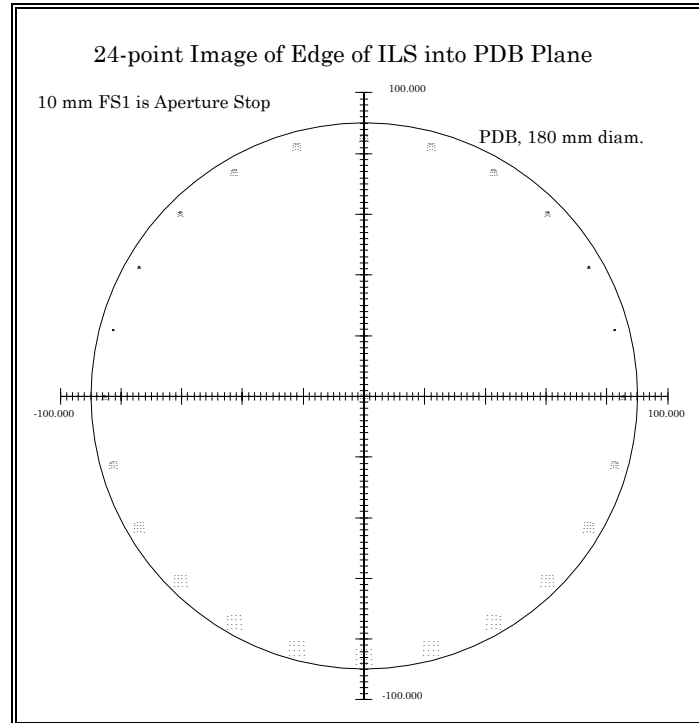


Figure x.x.x 24-point geometric image of the edge of the ILS into the plane of the PDB

The best focus image of the ILS occurs just above the center of the plot, and is tilted.

Uneven top-to-bottom clearance for alignment is again indicated. It is anticipated that this slight decenter would be corrected during alignment.

5.2 Quality and location of the image of each *field* on its next conjugate

Even the field stop sizes are cascaded smaller as the light passes through the system. While it is certainly true that a Lyot-like straylight reduction phenomenon occurs, this has not been estimated for HIRDLS, and size cascading for field stops is less rigorous than for pupil stops.

5.2.1 The image of FS1 on FS2

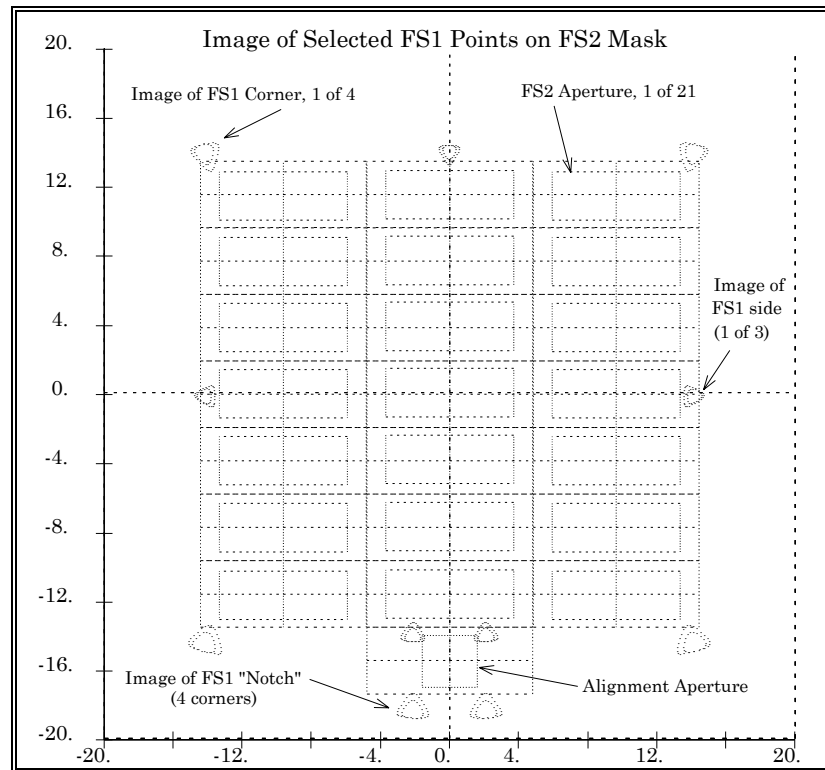


Figure x.x.x The geometric image of FS1 onto the FS2 mask shows negligible leakage into the mask apertures.

FS1 is imaged onto FS2 via the secondary mirror with the ILS as the local aperture stop.

The alignment channel requires a notch in FS1 and a special aperture in FS2.

Figure x.x.x above shows how key points in FS1 image onto FS2. The four corners of the main FS1 mask, the notch, and the center points of three sides are shown imaged onto FS2

The peculiar shapes shown as images are just the outlines of the aberrated images. (Rays were traced around the rim of the ILS. A second set was traced around the 0.7 zone in the ILS to gain some feel for the distribution of energy in the aberrated image.) The figure shows that, geometrically at least, virtually no light from the edges of FS1 can get past the FS2 mask apertures, assuming accurate alignment.

Even if there is some leakage, the detector footprints within the masks are substantially smaller than the masks in FS2.

5.2.2 Image of IFOVs on FS1, & FS2

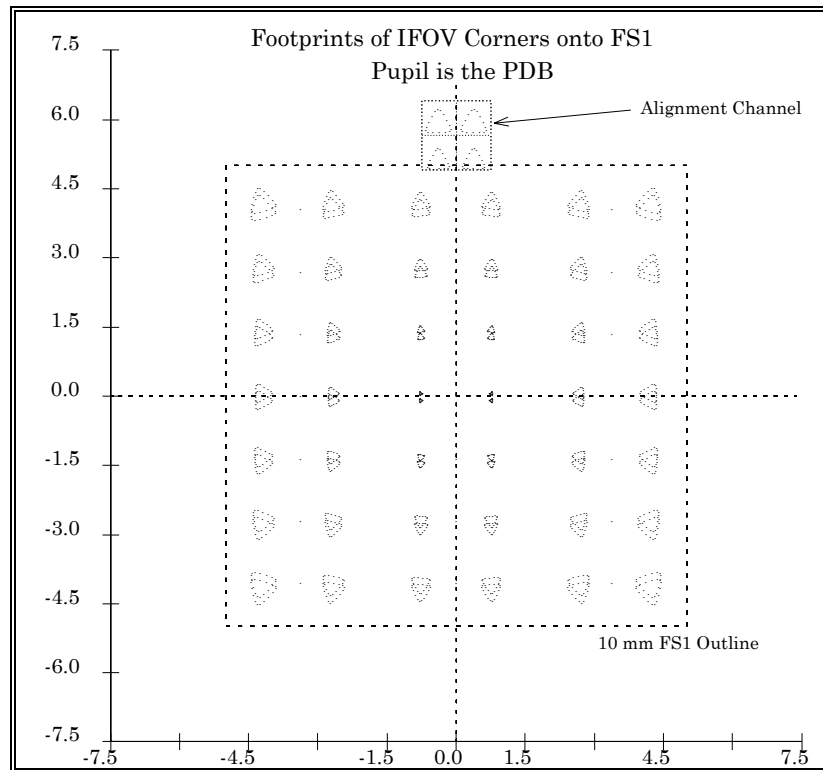


Figure x.x.x The beams from all the channels easily clear the FS1 aperture.

Rays are traced from each of the four corners of each channel IFOV, around the rim of the PDB as the defining aperture stop. The intersection of each ray with the FS1 plane is shown plotted in the figure to the left. The rounded triangular shapes represent the outline of the aberration of the image for each point.

The rays corresponding to the alignment channel are also shown, along with the FS1 notch needed.

The center ray for each channel, traced through the center of the PDB, is also shown as a single dot.

The figure indicates ~0.5 mm of clearance from the CFOV to the edge of the FS1 aperture.

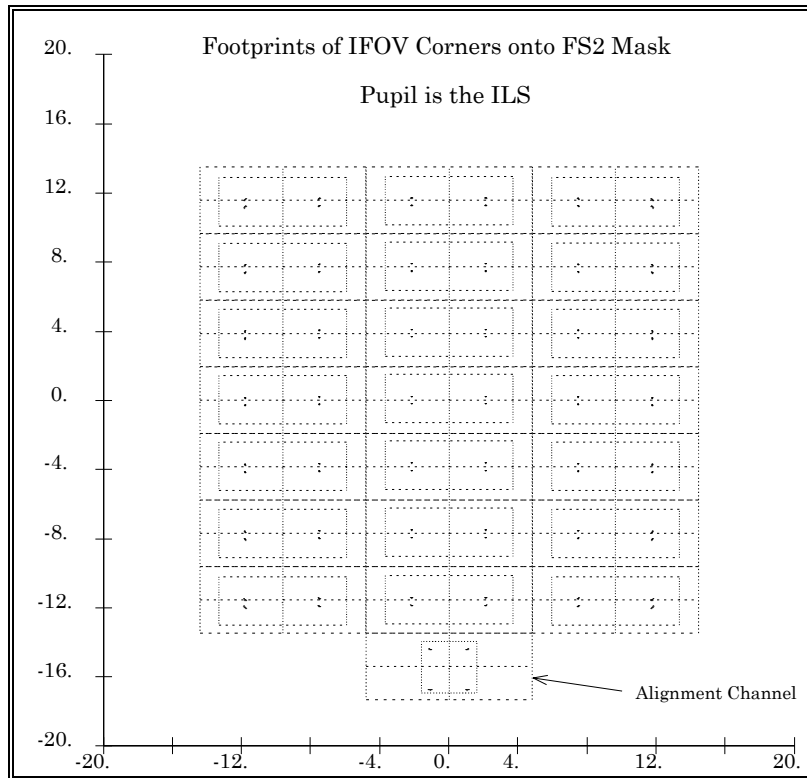


Figure x.x.x The images of the IFOV's are well centered in the FS2 masks

The figure to the left is similar to figure x.x.x above, except here, the defining aperture stop is the ILS, and the rays are plotted onto the FS2 mask plane.

Since the aberration in the images is small in this plane, the rays seem to coalesce into nearly a single point for each corner.

Except for the alignment channel, the four points within each sub-aperture of FS1 can also be interpreted as the image of the detector corners into the FS2 field mask. (This would assume ideally sized and located detectors in the final focal plane.)

5.3 Image of the SAS onto the PDB

As the SAS is the System Aperture Stop, its image in object space is, by definition, the entrance pupil. By design, the image is formed onto the PDB which is optically in object space. (The plane scan mirror does not effect this property). The area of the entrance pupil must satisfy an ITS requirement: 4.4.3.1.2, that the area exceeds 0.018m^2 ($18,000\text{mm}^2$) for every point in the IFOV of each channel.

There is a significant characteristic of the HIRDLS telescope that, due to aberration, the area of the entrance pupil varies over the CFOV. This characteristic is shown next in detail - first graphically, then in tabular format.

5.3.1 SAS footprints projected into the PDB

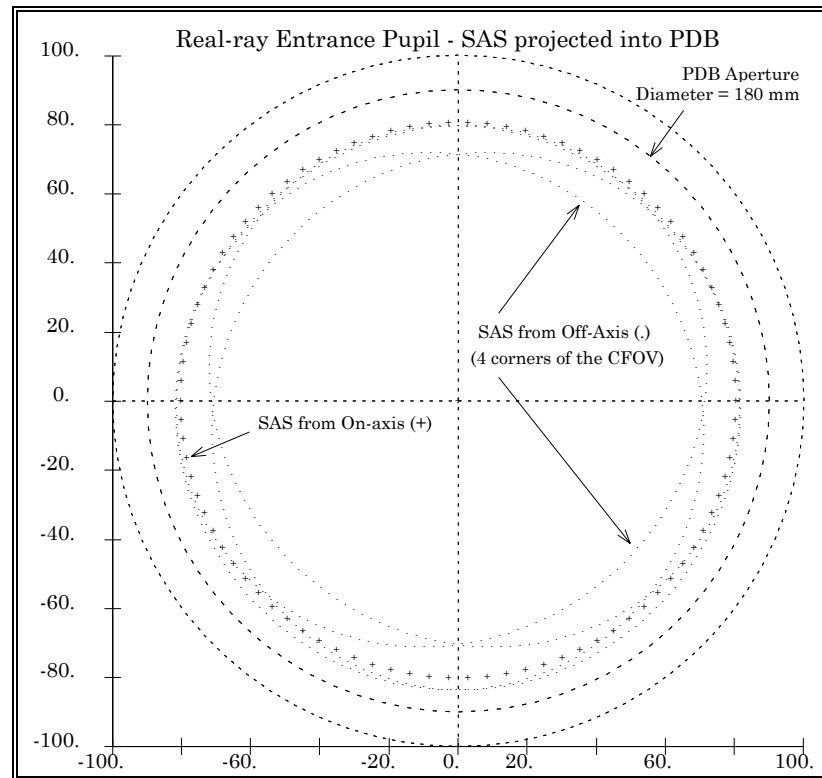


Figure x.x.x The real-ray entrance pupil shows significant variation of area with FOV

In the figure on the left, the SAS is projected onto the PDB plane from four field points within the CFOV. The “+” symbols show the the entrance pupil from the center of the CFOV.

From each of the four corners, the entrance pupils are also shown, this time plotted with a dot.

It is immediately apparent that the entrance pupil area, which is the area available for radiometric signal collection, is significantly less than the on-axis area. This effect needs to be used in the HIRDLS radiometric models.

5.3.2 Entrance pupil area, channel by channel

The entrance pupil area variation is severe enough that it is radiometrically significant even over a single channel in some cases. For example, for channel 10, there is a 4.9% variation in area between the entrance pupil areas observed from the extreme corners of the IFOV. For that reason, in the table which follows, the entrance pupil area quoted is the average value for three points in each IFOV: left, center, and right.

In addition, there is a “Normalized” column where the ratio of all the channel area averages are shown with respect to channel 2 (because it is centered in the CFOV). The

reciprocal normalization was chosen because it is easier to quickly see percentages for numbers slightly greater than 1.000.

**Table x.x.x Entrance pupil area for each channel
(>18000 sq mm req'd)**

Channel	Left	Center	Right	Average	Normalized
	mm ²	mm ²	mm ²		
1	20105	20119	20105	20109	1.0079
2	20265	20277	20265	20269	1.0000
3	20336	20351	20336	20341	0.9964
4	20279	20300	20279	20286	0.9991
5	19963	19995	19963	19974	1.0148
6	19844	19864	19844	19851	1.0211
7	18995	19349	19584	19309	1.0497
8	18191	18649	18967	18602	1.0896
9	19345	19374	19345	19354	1.0472
10	18976	18657	18197	18610	1.0891
11	19599	19364	19008	19324	1.0489
12	19952	19763	19467	19727	1.0274
13	19475	19771	19961	19736	1.0270
14	19688	19967	20144	19933	1.0169
15	19691	19996	20192	19960	1.0155
16	19426	19808	20060	19765	1.0255
17	18743	19254	19608	19201	1.0556
18	19615	19260	18748	19207	1.0553
19	20075	19822	19439	19779	1.0248
20	20221	20024	19716	19987	1.0141
21	20195	20016	19733	19981	1.0144
22	19244	19257	19244	19248	1.0530

5.4 Diffraction aspects of the pupil and field images

6.0 Footprints and Apertures (footpr.doc)

This section presents the geometric raytrace basis for the selection of all the aperture definitions of the elements in the HIRDLS imager and auxiliary paths.

6.1 Define critical, maximum, and mechanical apertures

Three aperture definitions are associated with each element. Each aperture plays a different role in the function of the system.

6.1.1 Mechanical aperture

The mechanical aperture is the physical diameter of an element, and is the largest of the three apertures. Many of the mechanical aperture values assigned should be considered preliminary because the optics supplier reserves the option to adjust for manufacturability.

6.1.2 Maximum clear aperture

The maximum clear aperture assigned to an element is defined by the rays bounded by the largest pupil and field stops in the optical space of the element. For example, the maximum clear aperture of the primary mirror is defined by rays bounded by the PDB and FS1.

6.1.3 Critical clear aperture

The critical clear aperture assigned to an element is defined by the imaging rays which are always bounded by the SAS and the corners of the CFOV, or each detector IFOV if appropriate.

6.1.4 Apertures and performance specifications

The best surface specifications in terms of optical figure and coating quality would be associated with the critical clear aperture.

In the annulus between the critical aperture and the maximum aperture, specifications can be more relaxed. For example, in this region a coating blemish, or a larger figure error may be acceptable which would not be acceptable within the critical clear aperture.

In the outer annulus between the maximum clear aperture and the mechanical aperture, there would normally be no optical specification. The coating edge may lie somewhere within this region. Edge chip and bevel specifications may apply in this region.

6.2 Maximum and Critical clear apertures, surface by surface

The specification document SP-LOC-139 *Detailed Optical Design Specifications* contains the official aperture values for the HIRDLS system. The basis for these values is exhibited in the figures which follow, but any aperture values quoted in this chapter are for reference only, and do not supersede the specifications in SP-LOC-139.

6.2.1 Scan Mirror

The footprints for the scan mirror in the figure x.x.x below assume that both scan axes lie in the plane of the mirror.

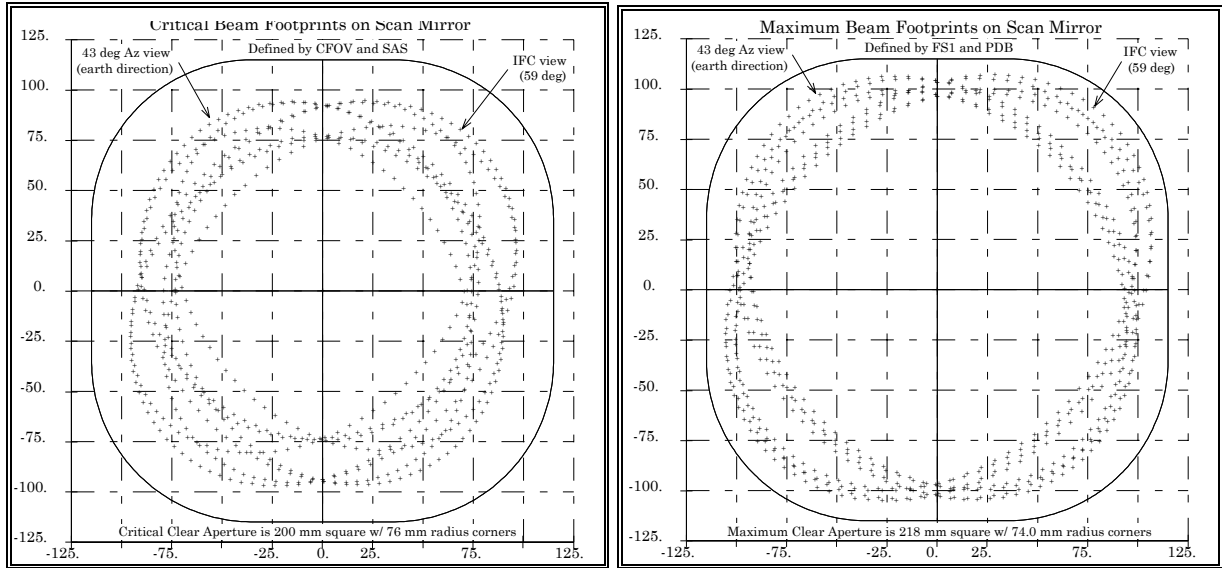


Figure x.x.x Critical (left) and maximum (right) clear apertures on the scan mirror.

6.2.2 Primary Mirror

The footprints in figure x.x.x below support the values of 190 mm and 160 mm respectively for the maximum and critical clear apertures of the primary mirror.

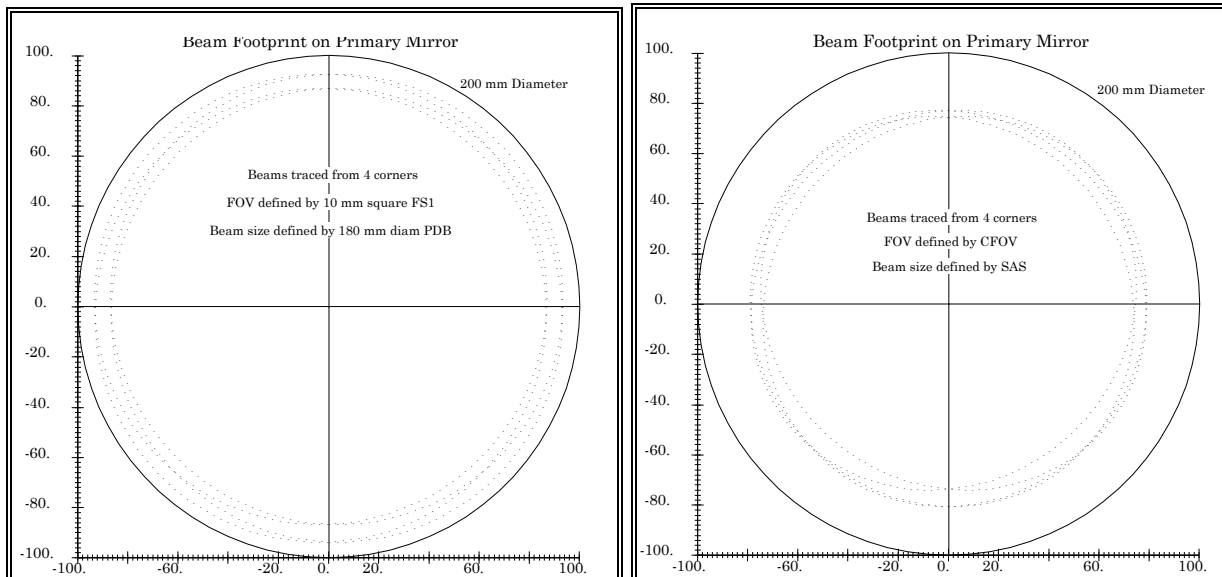


Figure x.x.x Maximum and critical clear apertures on the primary mirror.

6.2.3 Secondary Mirror

The outline of the FS1 mask is projected onto the secondary mirror along eight field rays dispersed around the boundary of the ILS to define the maximum clear aperture.

The footprints in figure x.x.x below support the values of 69 mm and 62 mm respectively for the maximum and critical clear apertures of the secondary mirror.

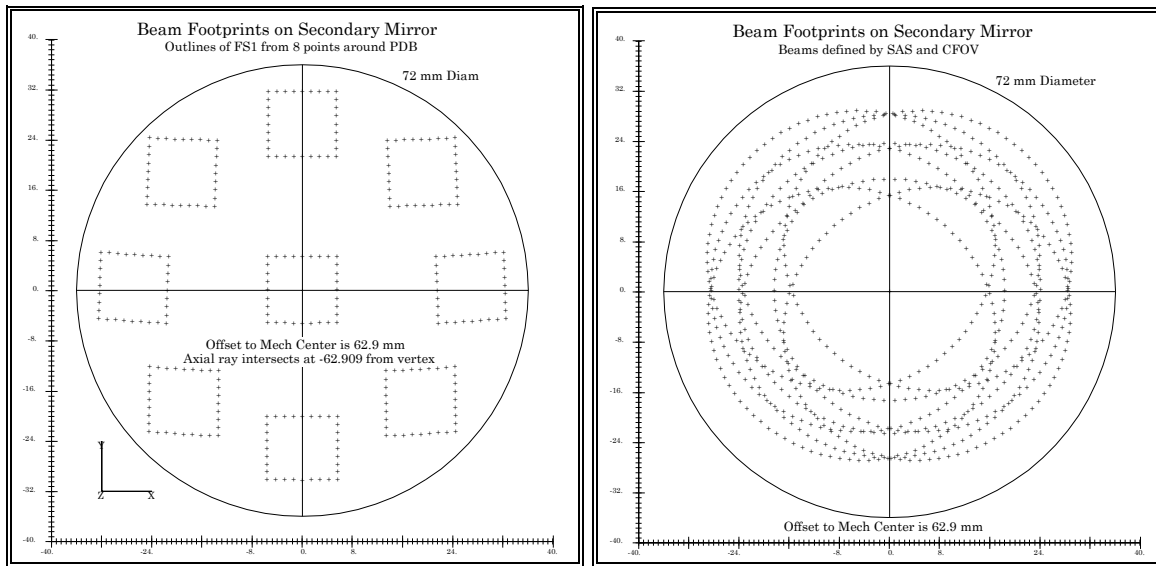


Figure x.x.x Maximum and critical clear apertures on the secondary mirror.

6.2.4 Germanium lens 1

Both surface 1 and 2 are represented in figures x.x.x and x.x.x below.

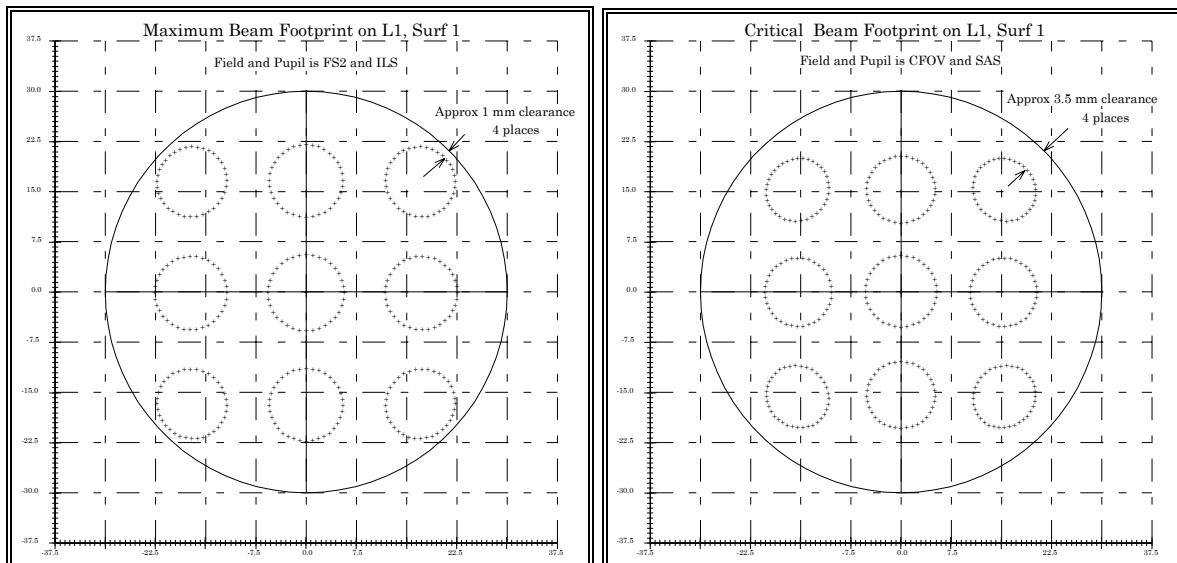


Figure x.x.x Maximum and critical clear apertures on germanium lens 1, surface 1.

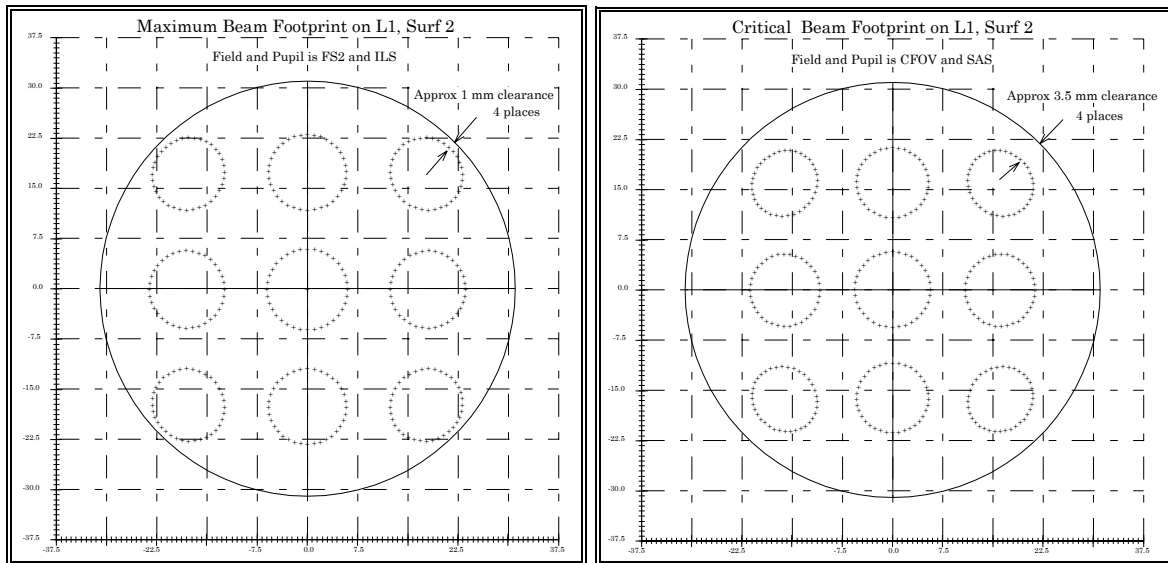


Figure x.x.x Maximum and critical clear apertures on germanium lens 1, surface 2.

The above figures support the values of 60 mm and 62 mm respectively for the maximum and clear apertures of Ge lens 1 on the front and rear surfaces. Also the critical clear apertures of 53 mm and 55 mm are supported. The optional racetrack clear apertures defined in SP-LOC-139 (5.1.11) simply enclose the footprints on the figures above.

6.2.5 Fold Mirror

Figure x.x.x below supports the values of 48 x 78 mm and 46 x 76 mm respectively for the maximum and critical elliptical clear apertures of the fold mirror.

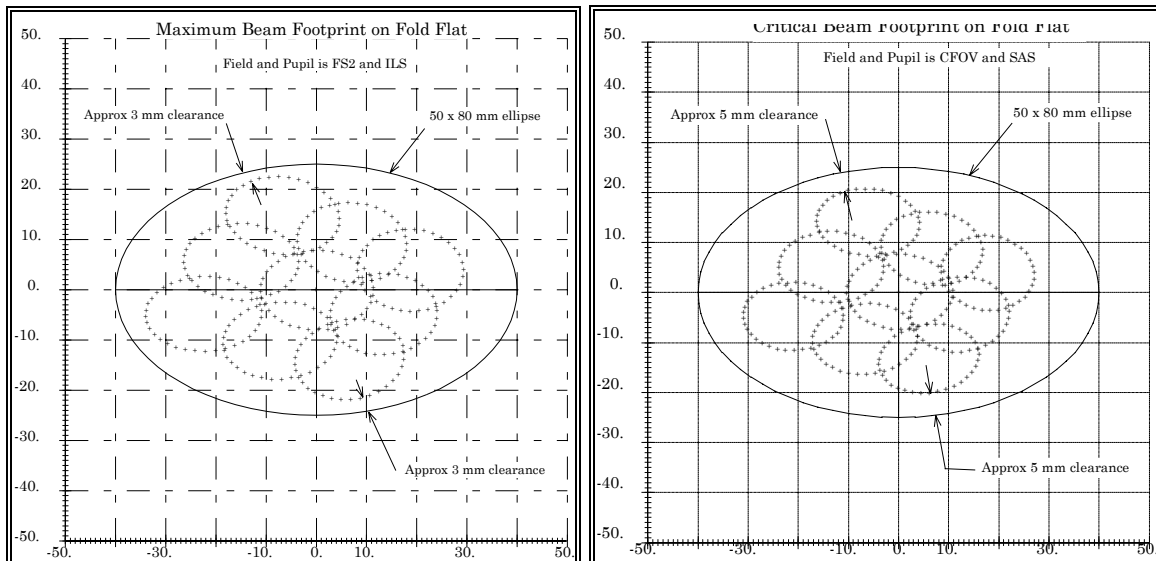


Figure x.x.x Maximum and critical clear apertures on the fold flat

6.2.6 Germanium lens 2

Both surface 1 and 2 are represented in figures x.x.x below for the critical aperture only. The maximum aperture accommodates the retro-sphere; rays are not shown for that case.

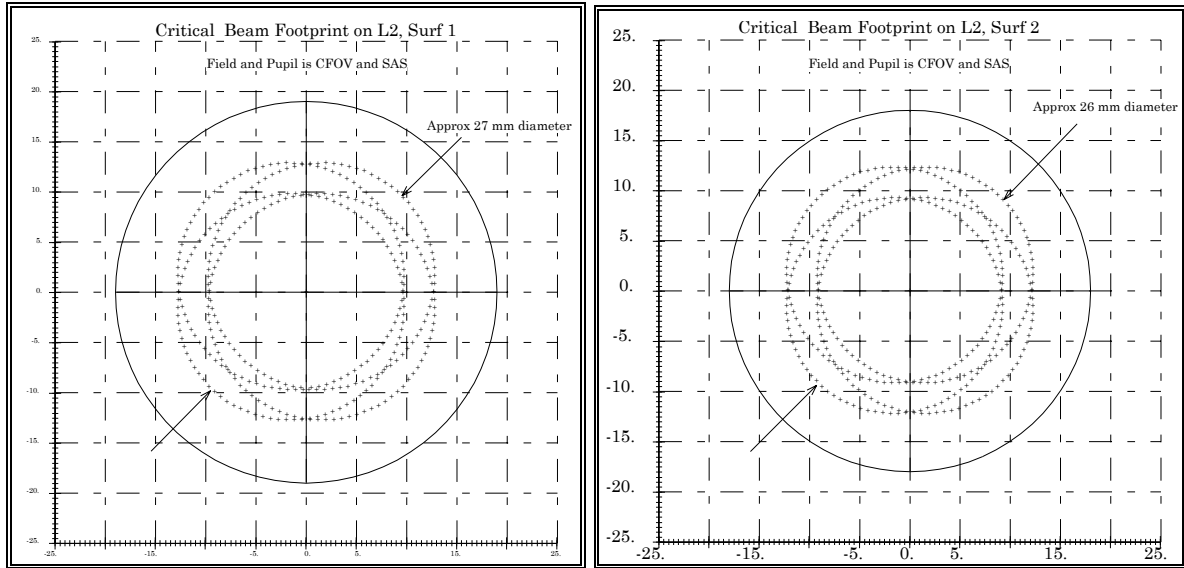


Figure x.x.x Critical clear apertures on germanium lens 2, surfaces 1 and 2.

6.2.7 Vacuum window

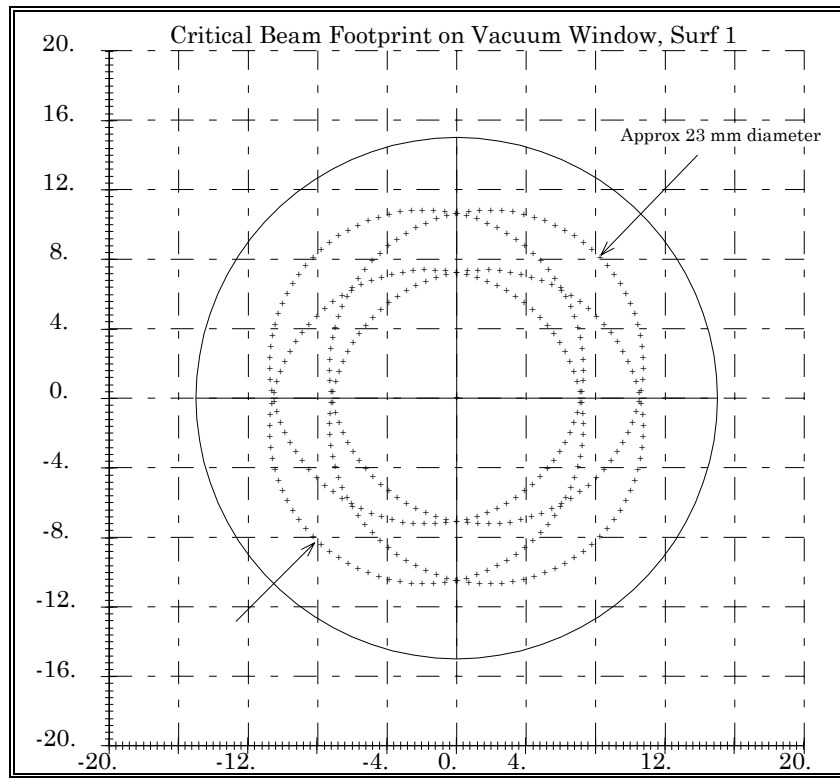


Figure x.x.x Critical clear aperture on the vacuum window, surface 1.

The footprints in figure x.x.x above supports the value of 28 mm for the critical clear apertures of the vacuum window. The maximum clear aperture of 28 mm (within 1 mm on the radius of the 30 mm mechanical diameter) is to accomodate the retor spheres function of background rejection.

6.2.8 Cold Shield

Only a critical clear aperture applies to the cold shield. There is 1.5 mm clearance from the beams to the edge of the cold shield aperture.

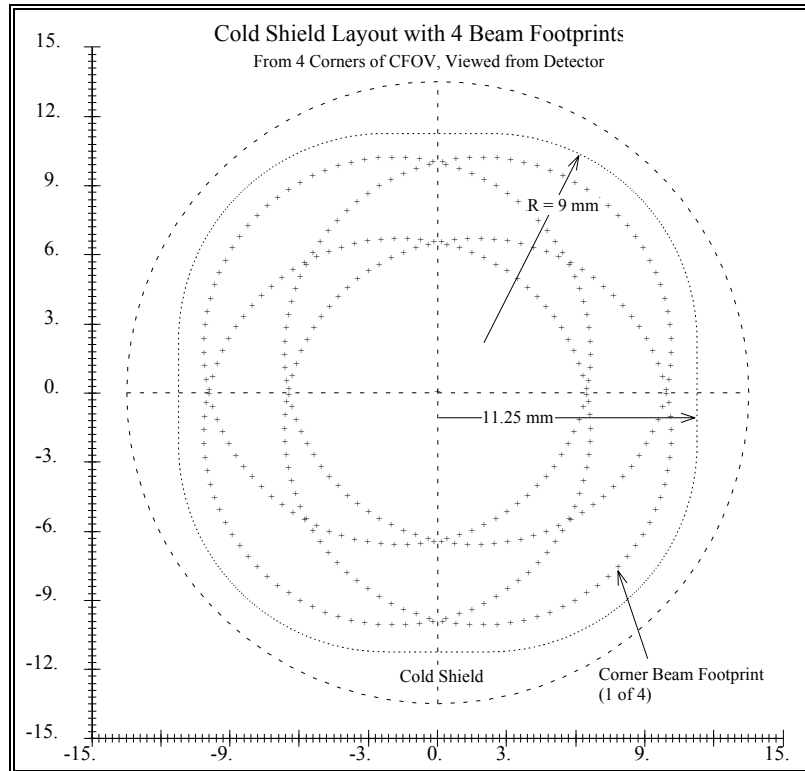


Figure x.x.x Critical aperture of Cold Shield shows about 1.5 mm clearance to edge.

6.3 Beam Geometry at FS2 and Warm Filters

Figure x.x.x below shows how key field points intersect with the current design of the FS2 field mask. Being in focus, each footprint is barely more than a point. For each channel, including the alignment channel, beams were traced from the 4 corners of the IFOV (1km x 10 km rectangle) at the earth limb.

In addition, beams were traced from 4 more corners, a 6km by 10 km rectangle centered on each IFOV. This represents the maximum vertical field which will be permitted to enter each channel unvignetted.

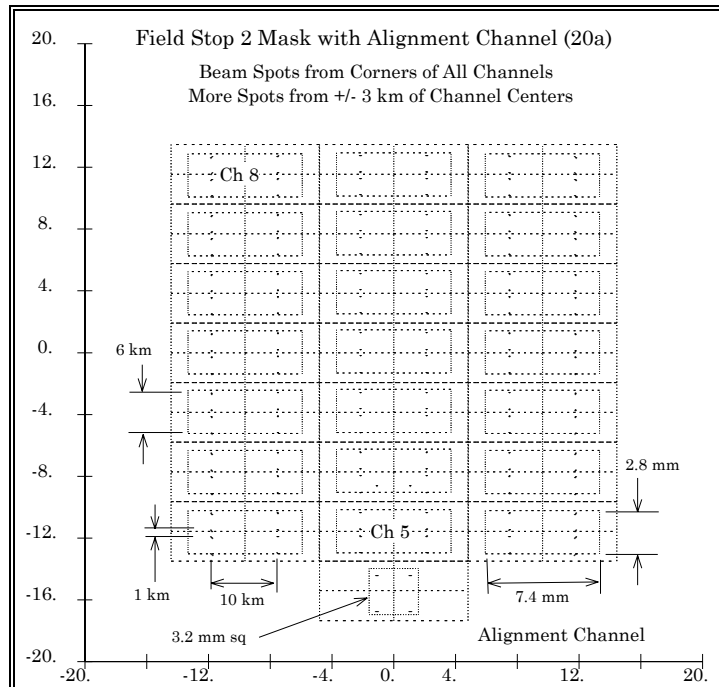


Figure x x x The mask array at FS2 accepts 6 km object heights

Figure x.x.x below shows the same beams as above on the warm filter array. The dimensions shown were taken from the ICD, and do not supercede the ICD data.

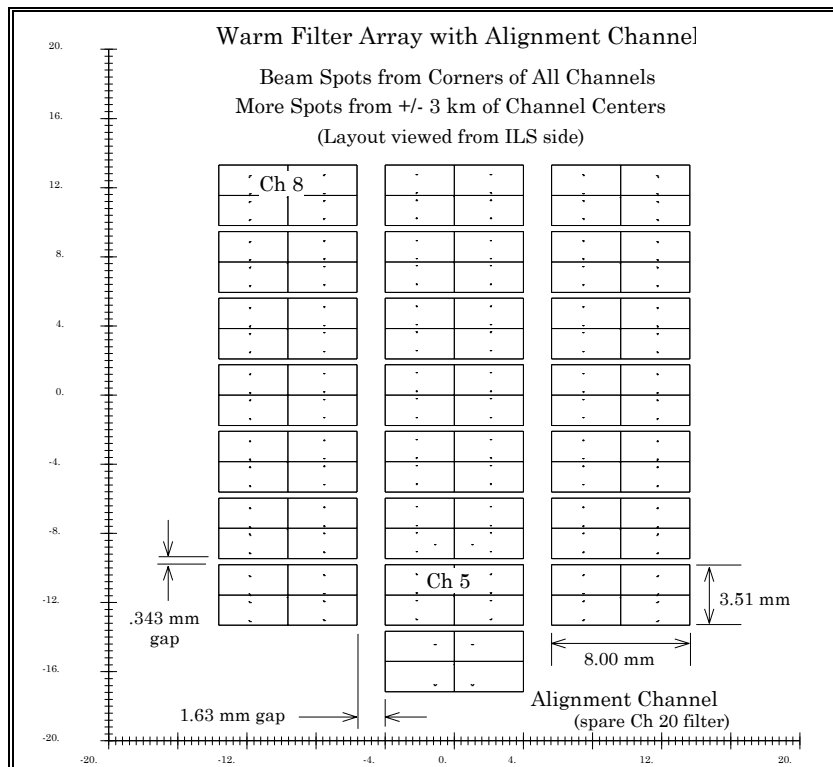


Figure x.x.x Warm Filter array with footprints

6.4 Beam Geometry at Cold Filters

The mosaic figure x.x.x below shows the beam footprints as they land on the front surface (Cold Shield side) of the Cold Filters. For the alignment channel, the beams are from the corner of the alignment acquisition FOV; these beams would miss the alignment detector.

It is clear from the figure that the filters are as large as can reasonably fit into the space available. The largest vertical (elevation) fields which can pass unvignetted to the detector plane is then ± 3 km, and not the ± 4 km which may be implied by the ITS Vertical Response specification. Fields larger than ± 3 km in any channel will begin to illuminate the adjacent channel causing a possible crosstalk problem. This is prevented by setting the FS2 masks for each channel to cut off at ± 3 km.

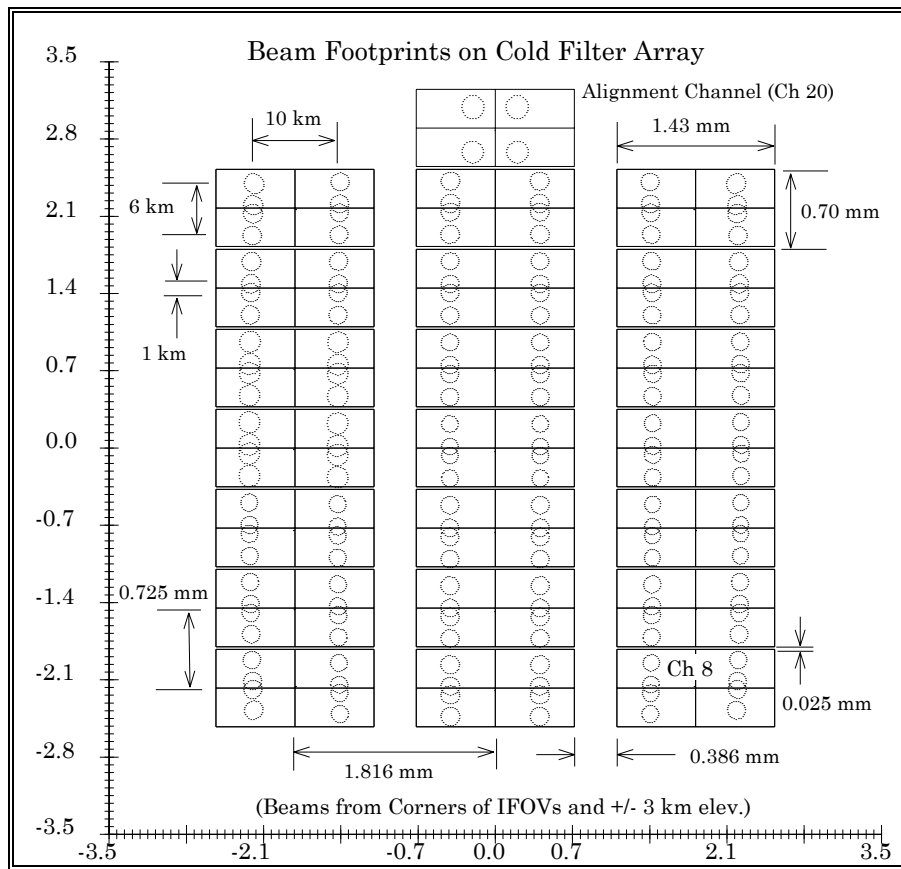


Figure x.x.x Beam footprints from ± 3 km just fit in the Cold Filter apertures

6.5 Angle-of-incidence histograms on selected surfaces

New work to be done.

6.6 Footprint on main box aperture

Exists? Repeat? Alignment Channel?

7.0 Chopper Waveform (chopwavf.doc)

7.1 Method of illumination simulation

We could define an “effective illumination patch” or beam patch for each IFOV as the bundle of all possible rays traced from all points in a channel IFOV through all points in the SAS. This patch would have a characteristic size, shape, location and energy distribution (or ray density distribution) on each optical surface in the imaging train. In particular, the beam patch on the chopper surface determines the shape and timing of the chopper waveform.

The beam patch for any channel is simulated by tracing a large number (50,000 was used) of individual rays from randomly selected points in the IFOV at 3000 km through randomly selected points in the PDB as the pupil, and storing the location of the rays where they intersect the chopper. (Only the rays transmitted through to the detector plane were counted). This patch of rays is then analyzed one channel at a time. The analysis method is explained in the section 7.2.

7.1.1 Uniformity of Illumination

To make the analysis as radiometrically relevant as possible, it is important that the PDB be the pupil to guarantee that the simulated input illumination to the instrument is realistically uniform. For off-axis points, the SAS is not uniformly illuminated due to aberration. If the SAS were selected as the pupil, then the ray-aiming feature in OPTIMA would force the entrance pupil (PDB) to be non-uniformly illuminated with the result of errors in the chopper signal profile.

Uniformity of the field is a similar concern. For this analysis, the field was assumed uniformly illuminated. While the real atmospheric fields are not uniform in the elevation direction, since chopping is done in the azimuth direction, this effect will not produce an error. However, it does assume that the detector responsivity is uniform along the long direction.

Thus, there is an unknown amount of error in the simulated chopper profiles because the non-uniform responsivity of the detector in the long direction has not been modeled here.

7.1.2 Relative amplitude of illumination

For each channel, 50,000 random rays were traced into the PDB. Depending on the entrance pupil area however, the total number of rays transmitted to the detector varied. (see section 5.3.2 *Entrance pupil area, channel by channel*). The raw data base, which is not presented in this document, contains this effect.

7.1.3 Extraction of the signal profiles

The chopper surface is selected as the geometric spot diagram collecting surface. The center of the spot diagram coordinates can always be defined as the point where the

system axial ray intersects the chopper surface. Thus, the illumination patch for each channel is located correctly relative to the axial ray.

By defining a line which can rotate through the spot diagram precisely like the edge of a chopper blade, OPTIMA will count the number of ray-points covered or uncovered as a function of the rotation angle of the line. Thus only one large spot diagram (geometrically simulated illumination patch) needs to be generated, and the rotating line (or knife edge) rapidly generates the chopper signal profile for the selected channel.

This is illustrated in the figure below which shows only a small number of rays.

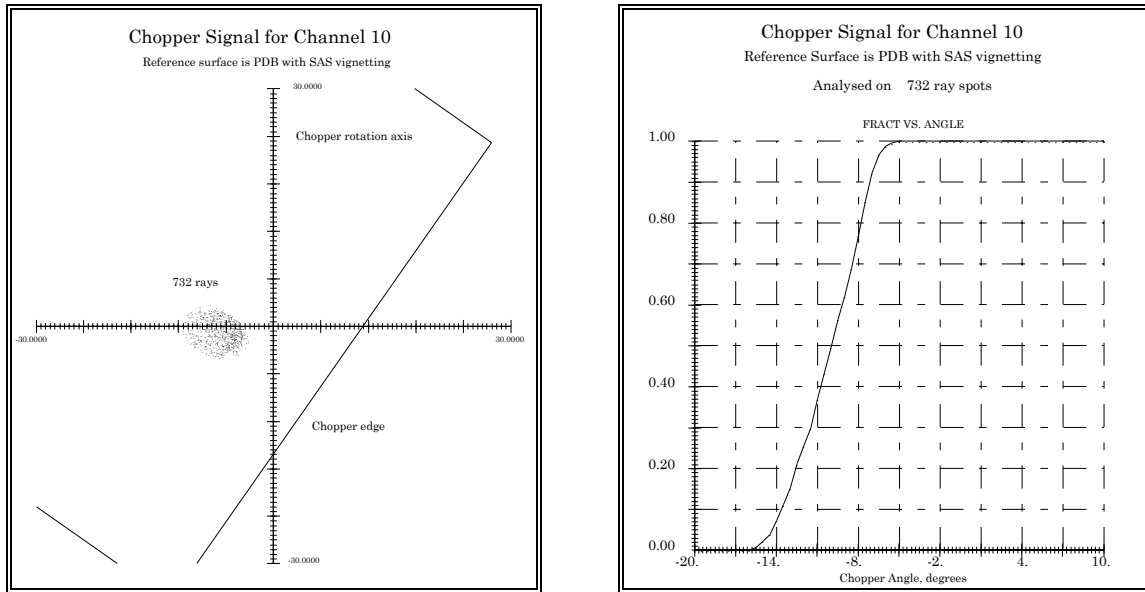


Figure 1 - Chopper signal simulation for channel 10 illustrates the method and result

In the analysis, the chopper angle is used as the independent variable. It could easily be converted to a time base given its rotation rate. The simulated chopper blade rotates in a direction which uncovers the beam patches as the chopper angle increases, so the signal changes from zero to 1.0. When the chopper edge lies precisely in the center of the beams, with the axial ray grazing the edge, the chopper angle for the analysis is -4.891 degrees.

7.1.4 Plot of the chopper signal profiles

Figure x.x.x on the following page shows the chopper signal for all 21 channels. There are several noteworthy features of this plot.

First note that the profiles are clumped in three groups. There are seven channels in each group, and they correspond exactly to the HIRDLS detector layout. Next note that all the center profiles cross at one point. This is the 50% point, and it crosses exactly at -4.89 degrees ! Finally, note how the slope varies. Slower rise times mean the patch is further from the focus at FS1.

Simulated Chopper Signal

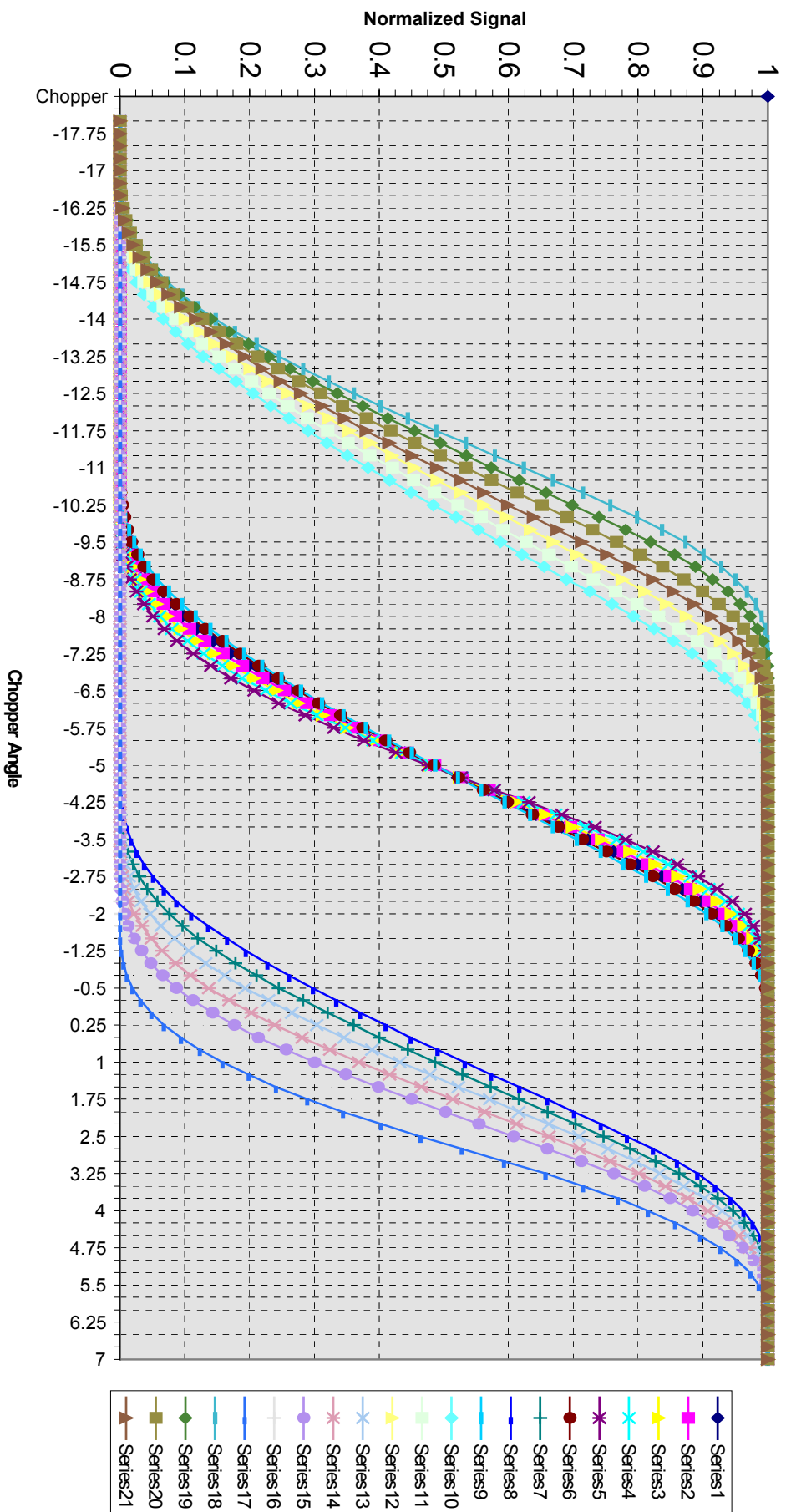


Figure x.x.x The Chopper Signal has been accurately synthesized on a common time base (chopper blade angle)

8.0 Image distortion and detector specification(distort.doc)

The object scene for the HIRDLS imager is given in the ITS as Table 4.5.1-1. Readers will notice that it is a very regular array with each channel squared in its location. The figure also states that the map is a projection of the field stop array, where it is understood that each detector is the final field stop for each channel.

Section 3.3.2 (last sentence) strongly implies that the long axis of each detector must lie parallel to the horizon because rotation will compromise the vertical response function.

Distortion in an optical system is a mapping error at the image caused by aberration of the chief rays. If there were no distortion in the HIRDLS imager, the image of the object scene layout would be regular array with the channel IFOVs squared in their locations.

There is distortion in the imager which can not be removed by ordinary design techniques. This distortion is the cause of the variation of EFL (table x.x.x) and most of the variation in entrance pupil area (table x.x.x).

8.1 Detector geometry

The distortion in the HIRDLS imager focal plane causes the ideal location of each detector to shift in a non-linear manner with respect to the center of the focal plane.

It also causes the ideal size of each detector to vary because the effective focal length of each channel varies.

Finally, the ideal orientation of the detectors in the left and right ladders are no longer “square” to the focal plane coordinates.

The only way to accurately create the projection of the channel layout as specified in ITS figure 4.5.1-1 is to tailor the detectors in size, location, and orientation according to the figure x.x.x below. Table x.x.x below gives the equivalent numerical requirements.

8.1.1 Method of determination

Figure x.x.x below shows the ideal detector layout for the HIRDLS imager. It was simply determined by tracing a series of chief rays from the edges of each channel to the detector plane, thereby outlining the ideal image of each channel. Aberration associated with the image has been ignored in this instance; it is quite small.

8.1.2 Ideal detector layout

The figure below shows the ideal detector layout as determined by raytrace.

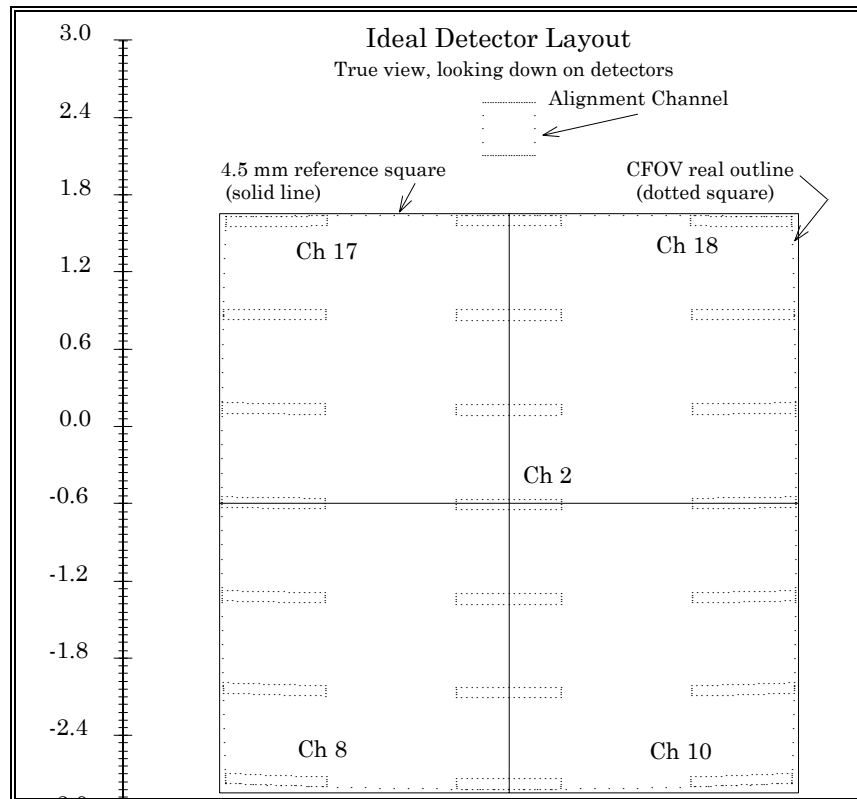


Figure x.x.x Ideal detector geometry will project to the required baseline layout as specified in the ITS

Figure x.x.x above is a “true view” looking down on the (ideal) physical detector layout.

8.1.3 Tabulated detector geometry

In the table x.x.x which follows, the ideal detector geometry is listed for each channel. Columns 2 and 3 give the locations of the centers of the detectors in a coordinate frame centered on channel 2. Columns 4 and 5 give the ideal sizes of the detectors.

Column 6 is the rotation for each detector which would produce the projection specified in the ITS figure 4.5.1-1.

Column 7 is an improved or corrected rotation value which includes the effect of the curvature of the earth limb. An additional 0.2 degrees has been applied to the outer channels. (See section 8.1.4, below *Earth limb curvature*) Even if 0.2 degrees is less than the mfg tolerance for the detectors, and even if all by itself it does not introduce a significant performance loss, it is an identifiable systematic effect which should be carried along.

Table x.x.x Ideal detector geometry dimensions, locations, and orientations

CHAN	Y-loc	X-loc	Length	Height	Angle	Ang.+Sag
Nbr.	mm	mm	mm	mm	deg	deg
1	-0.7336	0.0000	0.8172	0.0811	0.0000	0.0000
2	0.0000	0.0000	0.8178	0.0818	0.0000	0.0000
3	0.7377	0.0000	0.8172	0.0821	0.0000	0.0000
4	1.4758	0.0000	0.8150	0.0818	0.0000	0.0000
5	2.2083	0.0000	0.8106	0.0807	0.0000	0.0000
6	-1.4592	0.0000	0.8150	0.0800	0.0000	0.0000
7	-1.4370	1.8225	0.7968	0.0793	-1.5373	-1.3373
8	-2.1412	1.8102	0.7883	0.0769	-2.1669	-1.9669
9	-2.1715	0.0000	0.8108	0.0781	0.0000	0.0000
10	-2.1410	-1.8100	0.7882	0.0769	2.1695	1.9695
11	-1.4368	-1.8223	0.7967	0.0793	1.5396	1.3396
12	-0.7164	-1.8284	0.8011	0.0806	1.1292	0.9292
13	-0.7163	1.8283	0.8011	0.0806	-1.1297	-.9297
14	0.0130	1.8301	0.8024	0.0813	-0.8163	-.6163
15	0.7463	1.8280	0.8007	0.0815	-0.4958	-.2958
16	1.4784	1.8214	0.7957	0.0810	-0.0557	.1443
17	2.2010	1.8079	0.7862	0.0792	0.6496	.8496
18	2.2008	-1.8078	0.7861	0.0792	-0.6519	-.8519
19	1.4782	-1.8212	0.7956	0.0810	0.0535	-.1465
20	0.7461	-1.8277	0.8005	0.0815	0.4941	0.2941
21	0.0129	-1.8296	0.8020	0.0813	0.8163	0.6163
23	2.9207	0.0000	TBD	TBD	0.0000	0.0000

For the table above:

- “Point of view” is looking down onto the physical detector array.
- Positive X is to the LEFT, positive Y is on top of the array (as in figure x.x.x).
- (Ch 10 detector is on lower right, Ch 5 is top center.).
- Channel 23 is the alignment detector.
- A POSITIVE angle is a COUNTER-CLOCKWISE rotation.

8.1.4 Earth limb curvature

From the spacecraft, the earth limb is not rigorously a straight line, but is of course an arc. If the intent of the layout in Figure 4.5.1-1 in the ITS is followed, the outer IFOVs should be rotated .2 degrees to best conform to the earth limb curvature. The geometry for this value is shown below in the cartoon figure x.x.x.

The 0.2 result is easily calculated from the data that the radius of the earth is 6371 km, the spacecraft is flying 705 km above the surface, and that the distance between channel columns is 22.5 km

In the figure, channel 10 is at the lower left and would be rotated *counter-clockwise* 0.2 degrees. On the focal plane, channel 10 is on the lower right. To conform to the limb curvature, it should have a *clockwise* incremental rotation of 0.2 degrees.

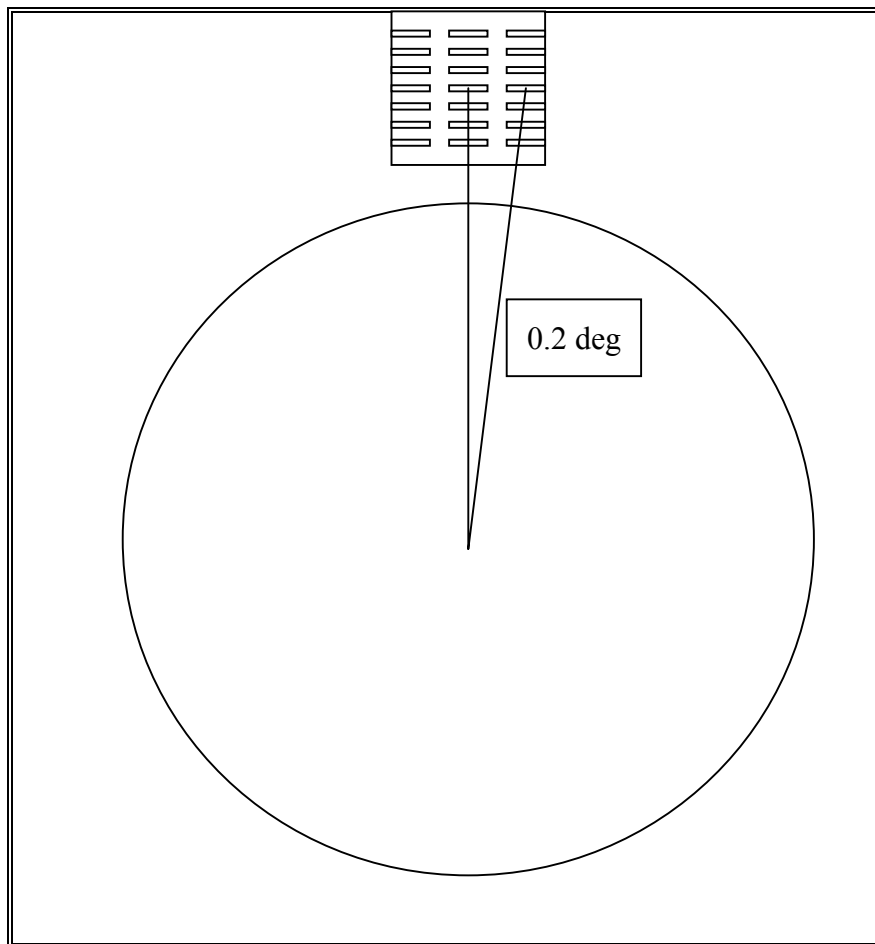


Figure x.x.x Geometry showing the 0.2 degree detector rotation due to earth limb curvature

9.0 Polarization Raytrace analysis (polariz.doc)

Although the radiation source at both the atmosphere and the IFC black body is unpolarized, this analysis explores whether radiometric calibration may have a significant component of error from variation of throughput due to polarization effects of the surfaces.

9.1 Coating specifications

Whatever variation in throughput there may be, exists due to the properties of the surface coatings, which are angle dependent. This section displays the data used for the polarization analysis.

9.1.1 n&k for gold

All the mirrors in the system are to be gold coated. The data is shown graphically in figure x.x.x below, and is for pure gold. The actual gold coating is to be an alloy whose reflectivity is very nearly the same as gold, but its n&k data are not known at this time. Thus the intent is to determine whether there is a potential problem, and if there is, to obtain measurements of n&k for the alloy, and then repeat the analysis.

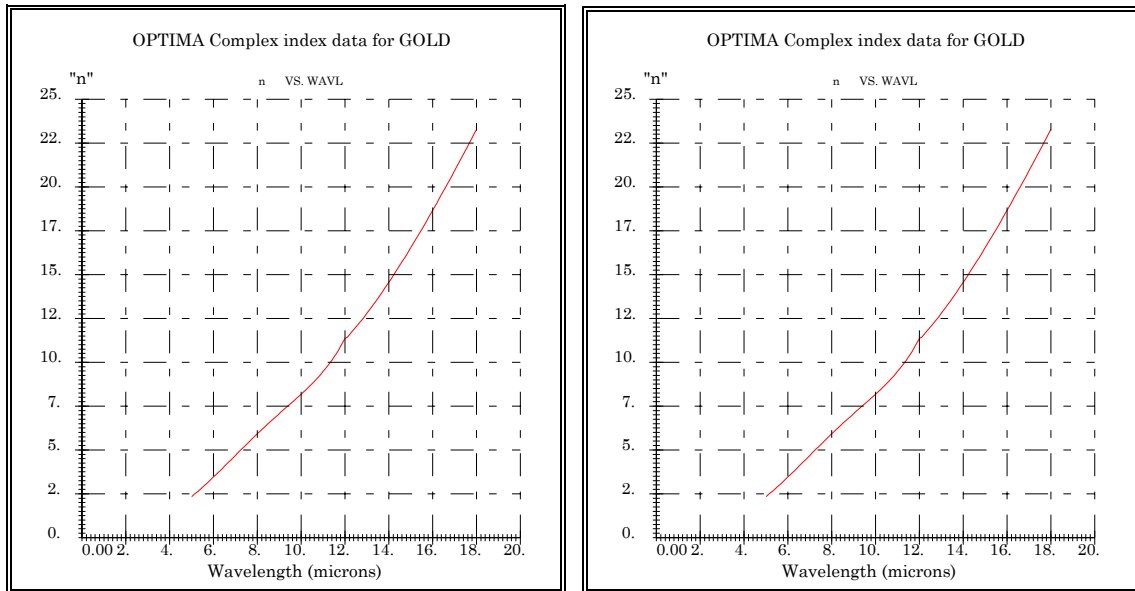


Figure x.x.x Complex index of refraction for Gold, 6 - 18 microns.

From the data above, the polarization dependent reflectivity and phase shift can be computed over a range of angles for any wavelength. While n&k for gold are very dispersive over the HIRDLS passband, the variation of polarization behavior is rather mild. This is shown in figures x.x.x through x.x.x below for 6 and 18 microns.

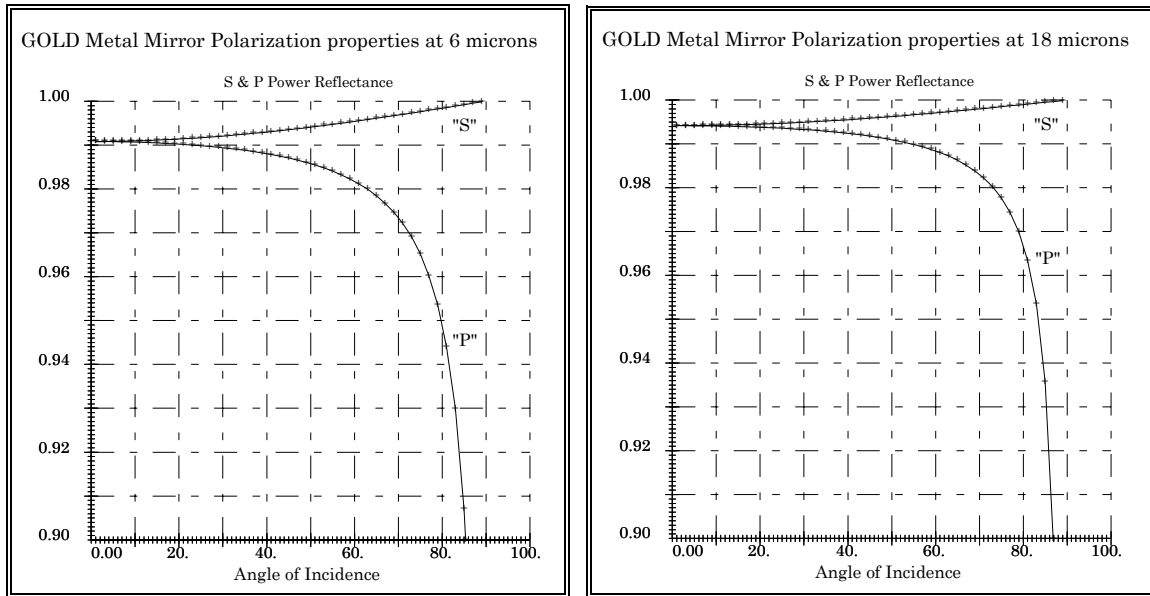


Figure x.x.x The polarization reflectivity of gold changes mildly over the 6-18 micron wavelength

When considering the possible HIRDLS effect of scan induced transmission error, note that the variation of angle of incidence on the scan mirror is from ~25 degrees ("unscanned" position) to ~36 degrees (IFC position).

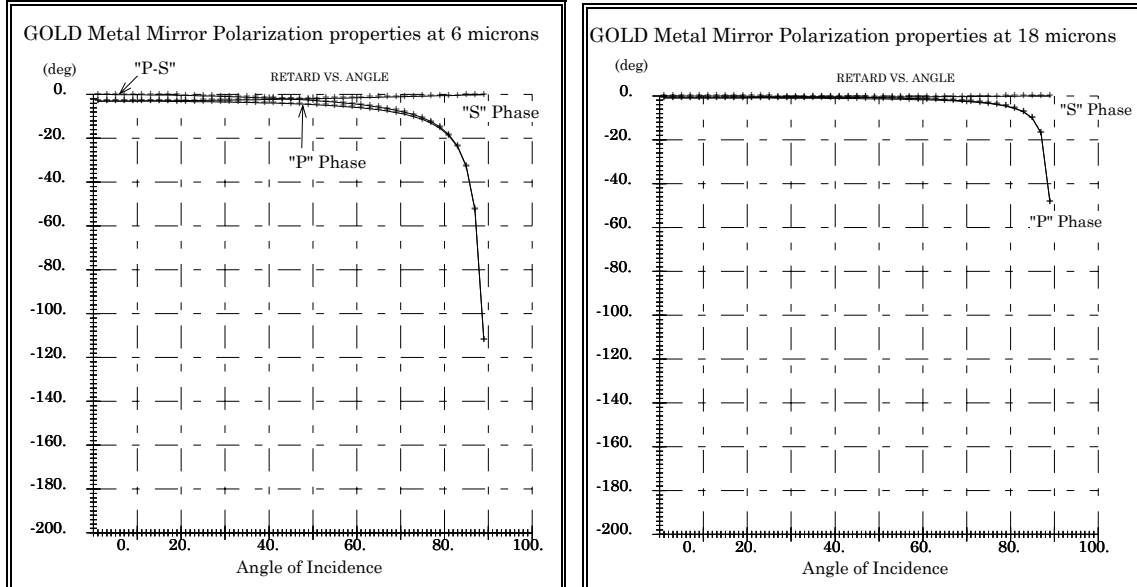


Figure x.x.x The polarization phase-shift for gold changes little over the 6-18 micron wavelength.

9.1.2 Antireflection coating

The germanium lenses and ZnSe vacuum window are to be coated with proprietary broad-band antireflection thin film stacks. Radiation for the outlying channels, especially 8, 10, 17, & 18, pass at fairly high angles of incidence on these surfaces. During a scan, there could be a variation in throughput because the polarization state off the scan mirror undergoes a scan angle dependent change. As the largest scan angle is the IFC view, there may be a calibration error from this effect.

The (tables, graphics) below indicate the properties of the antireflection coatings.

[No properties have been received to date. This chapter will be completed at a later time.]

9.2 Method

9.3 Axial ray, surface by surface example

9.4 Axial ray, each channel at detector

9.5 Pupil polarization aberration, somehow

10.0 Ghost Images (ghosts.doc)

The refractive elements in the relay section are all coated with either an antireflective thin film stack (lenses and vacuum window) or narrow-band filter/blocker stacks (warm and cold filters). Since none of the coatings will be perfectly efficient, some fraction of incoming light headed towards a particular detector will be partially reflected off each surface to begin a return towards the telescope optics. This returning light will be again partially reflected off each refractive surface encountered to propagate again towards the detector. This twice-reflected ghost light can end up on a different detector than originally targeted, with the potential of compromising radiometric accuracy.

It is the specific intent of the optical layout architecture to minimize the intensity of ghost illumination on the detectors by employing a filter array at FS2 as well as at the detector. However as some spectral channels have overlapping tails, the spectral isolation intended by the architecture may not be complete. The concept cannot work at all for channels 18 and 19 which have the same center wavelength, with channel 19 spectrally contained within channel 18. As these two channels are physically adjacent on the focal plane, they are especially vulnerable to each others ghosting effects. However, as they are also in the corner of the CFOV, some ghost illumination is vignetted away by the stop (SAS).

TC-RAL-47A has summarized an analysis of ghost illumination and has concluded that the ghost illumination levels are well below their original allocation. For that analysis, raytracing involved automatic ray splitting at the refractive surfaces, and large numbers of randomly placed rays in a reversed optical layout. A matrix method was used to develop the radiometric impact of all the ghosts. While this approach was perfectly valid, it does not provide a detailed understanding of specific ghosting paths.

This section is not intended to either replace or augment TC-RAL-47A. By using a different approach, individual ghosts images are independently developed one at a time, and the reader can gain some physical insight to the details of this phenomenon.

10.1 The ghost image geometric concentration ratio

Each ghost image is determined exactly by creating a ghosting prescription from the original prescription. The two ghosting surfaces are selected, turned into reflectors, and all the intervening elements appropriately inserted (automatically, not by hand!). Two pairs of real rays are traced close to the chief ray (as 2-ray x and y fans) and their linear separations are recorded at the entrance pupil and at the detector. The product of the ratios of these separations is called the geometric concentration ratio (GCR), and represents the *geometric* intensity of the ghost image. In other words, it is the ratio of the area of a small beam incident on the optical system to the area of the same beam on the detector.

A very large GCR represents a well focused ghost image. For example a point source which produces a ghost spot 80 microns in diameter (same size as the detector) has a $GCR \approx 4 \cdot 10^6$. If the ghost spot spans twice the vertical detector separation (~ 20 km

object space, or 1.45 mm), the GCR $\approx 12 \cdot 10^3$. Finally a spot just circumscribing the detector array (diameter = 6.36 mm) has a GCR ≈ 630 .

A ghost of *any* GCR value may be vignetted, in some cases, heavily. Thus, the extent of the illumination of each ghost must be tested by raytrace. All of the CGR values recorded for this chapter are for an on-axis point source.

10.1.1 Relative transmittance of the ghost beam

In order to turn the GCR into a radiometrically relevant quantity, the transmittance *ratio* Tr of the ghost beam to the non-ghost beam must be found. In such a ratio, all of the surface transmittances of the imager cancel leaving the relatively simple expression

$$\text{Tr} = \text{Rg1} \cdot \text{Rg2} \cdot (\text{Tg})^2$$

where Rg1 & Rg2 are the reflectances of the two ghosting surfaces, and Tg is the transmittance of the elements between the two surfaces. If both surfaces are lens or window surfaces with Rg $\sim .03$, and Tg $\sim .88$ (for 4 surfaces), then a typical relative ghost transmittance is ~ 0.0007 of the imaging beam.

If bulk absorbtion is significant, then Tg must also contain the term, for each element,

$$(e^{-(a \cdot t)})$$

where a and t are the coefficient of absorbtion and thickness. Units for a are usually cm^{-1} , so thickness must be also expressed in cm.

10.1.2 Ghost watts on the detector

Actual power computations are not included at this time.

10.2 Two surface ghosts

The elements involved in two surface ghost production are the warm filter(s) (WF), germanium lenses 1 and 2 (L1, L2), the vacuum window (VW), cold filter(s) (CF), and the detector itself. The surfaces of each element are designated S1 and S2 (S2 faces the detector). Each ghost is identified by a simple shorthand identifying the surfaces in the order encountered: L2-S2 & WF-S1 identifies a ghost produced by a first reflection off the second surface of lens 2 and a second reflection of the first surface of the warm filter.

A total of 36 ghosts involving two surfaces have been examined and GCR's recorded. Other two surface combinations were not explicitly done for the following cases:

Ghosts for WF, S1 & S2 which are extremely well focused with GCR's $> 10^7$.

Ghosts for CF S2 with all upstream surfaces (except CF S1) have the same GCR's as for CF S1 with upstream surfaces, which were recorded.

Ghosts for CF-S2 & CF-S1 are localized to the detector channel, as is the ghost from the detector with both CF surfaces.

Ghosts from the detector with all the rest of the upstream surfaces have GCR's nearly the same as for CF S1.

Figure x.x.x below shows the layout of the relay segment as prepared for this ghost analysis

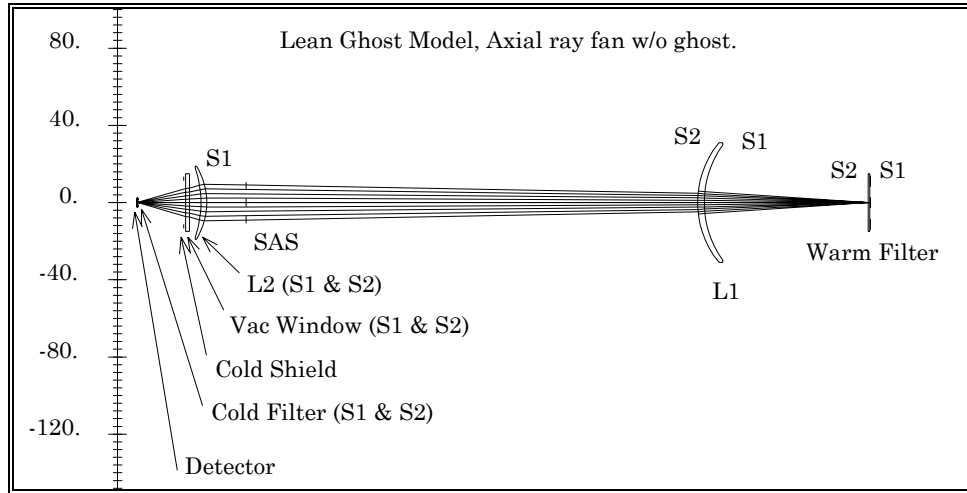


Figure x.x.x The elements for ghost image evaluation begin with the warm filter.

10.2.1 Selected examples 2 surface ghosts

The figures below are not a comprehensive collection, but are intended to show a variety of ghost images.

Figure x.x.x below shows an unvignetted, dilute (low GCR), high relative transmission ($Tr \sim .025$) ghost which would affect channels 18 & 19.

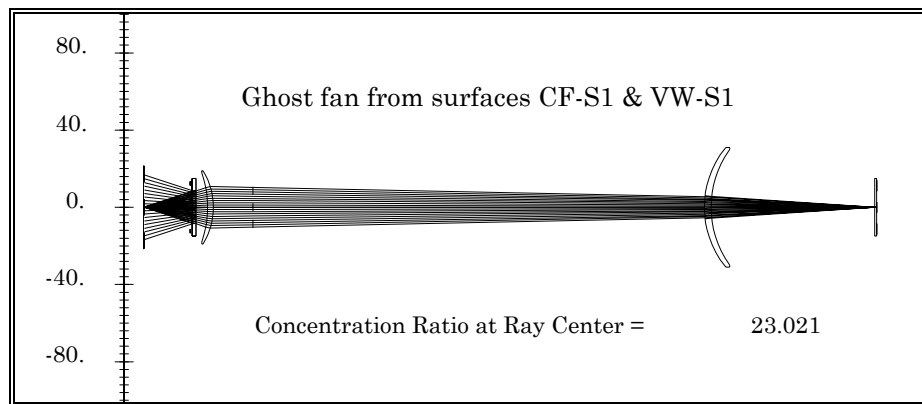


Figure x.x.x Cold Filter ghosts have a high Tr due to a high CF reflectivity

The next ghost example in figure x.x.x below also has a high $Tr \sim .02$, a moderate GCR (~ 620), but it is severely vignetted. No ghost illumination from any place in the object CFOV can flood more than the center 1/2 of the focal plane. Thus channels 18 and 19 cannot participate in this ghost.

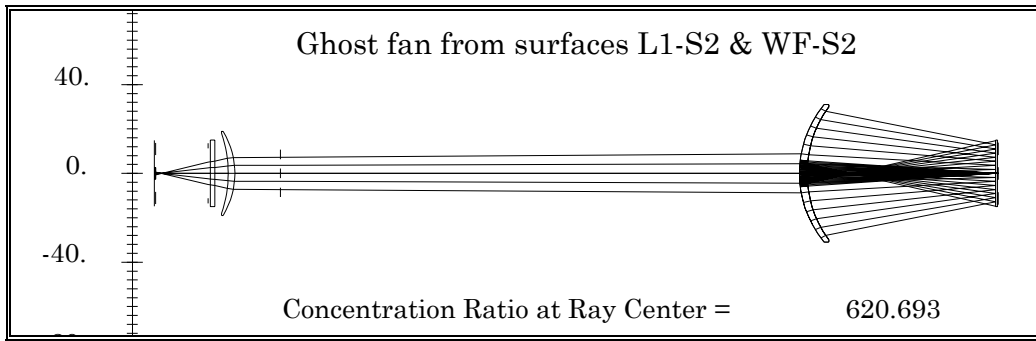


Figure x.x.x Warm Filter ghosts also have high Tr due to high WF reflectivity

The next ghost, figure x.x.x below is unvignetted and fairly concentrated with GCR = ~21000. A point source anywhere in the CFOV produces a ghost illumination 1.2 mm in diameter, so channels 18 and 19 will certainly share this ghost. However, it has a low relative transmittance of $T_g \sim .0009$.

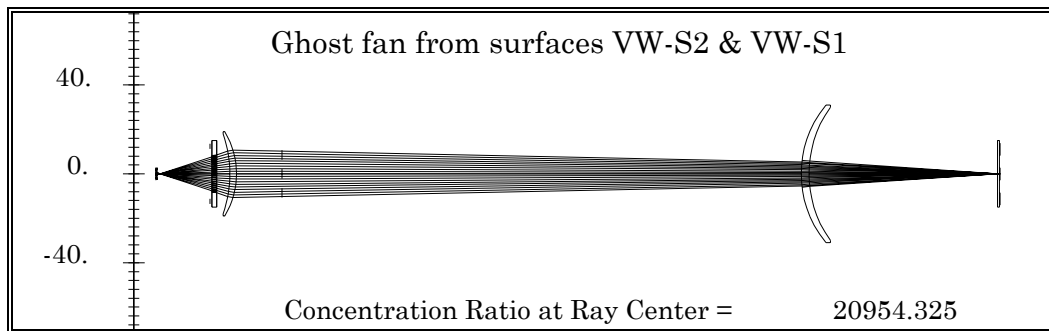


Figure x.x.x The vacuum window surface ghost is an important source for optical crosstalk

The next ghost, figure x.x.x, because it involves the CF and the WF, has a very high relative Tr exceeding 30% and a very high GCR. The effect of this ghost is detailed later in section 10.3

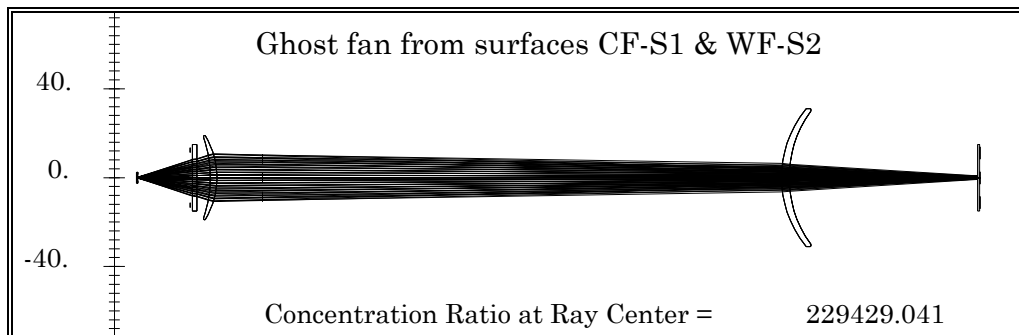


Figure x.x.x The ghost from the warm and cold filter surfaces is very concentrated

10.2.2 Tabulated summary of 2 surface ghosts

In table x.x.x below, the properties of the 36 2-bounce ghosts are listed. The column titled ‘vignettes?’ contains information about how the focal plane is illuminated by the full CFOV object. Unless the entry is NO (meaning that the illumination is uniform to the corner of the focal plane for that ghost), the first number gives the fraction of random rays which reach the focal plane, and the second gives the maximum diameter (in mm) of illumination on the focal plane. The full focal plane diagonal is ~6.4 mm, so values greater than 6 mm probably are ghosts which flood the focal plane. Frequently only a few ghost rays out of 30,000 rays incident on FS2 make it to the detector. Channels 18 and 19 can share ghost illumination for flood diameters greater than about 5 mm; at 6.4 mm, they may be exchanging as much as geometrically permissible.

For the relative transmission, lens and window surfaces have 3% reflection with no absorption, and filters have 10% reflection in-band with no absorption. Out of band, the filters have ~100% reflection. Which value to apply depends upon how the ghost illumination is spread over the warm filter array. A subscript, either *ib* or *ob* after each Tg value indicated which value was applied. For cold filters working as a first ghosting surface, the in-band reflectivity always applies. Since the intent here is only to be reasonably approximate, no special effects such as interference, or multiple internal filter reflections are considered.

Table x.x.x Characteristics of 2-bounce ghosts.

Ghost nbr	1 st refl surface	2 nd refl surface	Axial GCR	Relative Transm.	Vignettes? frac dia		Trouble for Ch 18 & 19?
1	WF-S2	WF-S1	>10 ⁷	.01 _{ib}	.87	6.3	NO: focused at same ch.
2	L1-S1	WF-S2	4070	.003 _{ib}	.017	2.43	NO: Fully vignnetted
3	L1-S1	WF-S1	3990	.0024 _{ib}	.015	2.23	NO: Fully vignnetted
4	L1-S2	L1-S1	1560	.0009	.013	2.7	NO: Fully vignnetted
5	L1-S2	WF-S2	621	.0028 _{ib}	.0062	2.5	NO: Fully vignnetted
6	L1-S2	WF-S1	612	.0023 _{ib}	.0069	2.46	NO: Fully vignnetted
7	L2-S1	L1-S2	.44	.0009	0	na	NO: Too dilute
8	L2-S1	L1-S1	1.71	.00085	.00001	na	NO: Too dilute
9	L2-S1	WF-S2	13	.0027 _{ib}	.0033	2.9	NO: Fully vignnetted
10	L2-S1	WF-S1	13	.0018 _{ib}	.0031	2.9	NO: Fully vignnetted
11	L2-S2	L2-S1	7.0	.0009	.0072	6.9	SMALL:Dilute+low tran
12	L2-S2	L1-S2	3.3	.00085	.0003	1.3	NO: Fully vignnetted
13	L2-S2	L1-S1	12	.00080	.0004	1.1	NO: Fully vignnetted

Ghost nbr	1 st refl surface	2 nd refl surface	Axial GCR	Relativ e Transm.	Vignettes? frac dia		Trouble for Ch 18 & 19?
14	L2-S2	WF-S2	81	.0025 _{ib}	.033	4.3	NO: Fully vignetted
15	L2-S2	WF-S1	82	.0020 _{ib}	.033	4.4	NO: Fully vignetted
16	VW-S1	L2-S2	50	.0009	.053	7.0	SMALL:Dilute+low tran
17	VW-S1	L2-S1	7.3	.00085	.007	6.9	SMALL:Dilute+low tran
18	VW-S1	L1-S2	.83	.00080	.00007	na	NO: Too dilute
19	VW-S1	L1-S1	3.1	.00075	.00007	na	NO: Too dilute
20	VW-S1	WF-S2	22	.0027 _{ib}	.0079	3.3	NO: Fully vignetted
21	VW-S1	WF-S1	22	.0024 _{ib}	.007	3.3	NO: Fully vignetted
22	VW-S2	VW-S1	20950	.0009	.842	7.0	YES: Significant ghost
23	VW-S2	L2-S2	51	.00085	.054	7.0	SMALL:Dilute+low tran
24	VW-S2	L2-S1	8.2	.00080	.0079	6.9	SMALL:Dilute+low tran
25	VW-S2	L1-S2	.88	.00075	.00007	na	NO: Too dilute
26	VW-S2	L1-S1	3.34	.00071	.0003	1.1	NO: Fully vignetted
27	VW-S2	WF-S2	24	.0022 _{ib}	.0085	3.53	NO: Fully vignetted
28	VW-S2	WF-S1	24	.0018 _{ib}	.0074	3.6	NO: Fully vignetted
29	CF-S1	VW-S2	25	.0030	.026	7.1	MAYBE: High transm
30	CF-S1	VW-S1	23	.0028	.024	6.8	MAYBE: High transm
31	CF-S1	L2-S2	82	.0027	.085	7.1	MAYBE: High transm
32	CF-S1	L2-S1	14	.0025	.015	6.84	MAYBE: High transm
33	CF-S1	L1-S2	390	.0024	.0022	1.5	NO: Fully vignetted
34	CF-S1	L1-S1	2240	.0022	.006	1.54	NO: Fully vignetted
35	CF-S1	WF-S2	2.3E5	.0069 _{ib}	.317	5.6	MAYBE ¹ : High transm
36	CF-S1	WF-S1	2.4E5	.0056 _{ib}	.312	5.7	MAYBE ¹ : High transm

Note 1: No crosstalk observed in simualtion of ghost 35 through FS2

10.3 Selected ghosts from channel 19

Because of the complexity of vignetting of off-axis ghosts, the data in table x.x.x above can only be taken as a filter for isolating *potential* ghosting surface pairs. Three ghosts (number 22, 31, & 35) are examined in detail in this section.

Figure x.x.x next depicts the illumination of the focal plane through FS2 stop for channel 19. The focal plane is not encumbered with any other apertures related to the CF array mounts. Of all the rays passed, ~8.9% strike the detector outline shown. This is about the right value since if the channel 19 FS2 aperture is projected 3000 km to the earth limb, it encloses an area of 111.88 sq km. The 10 sq km of the detector conjugate is just 8.938% of the area of the FS2 conjugate.

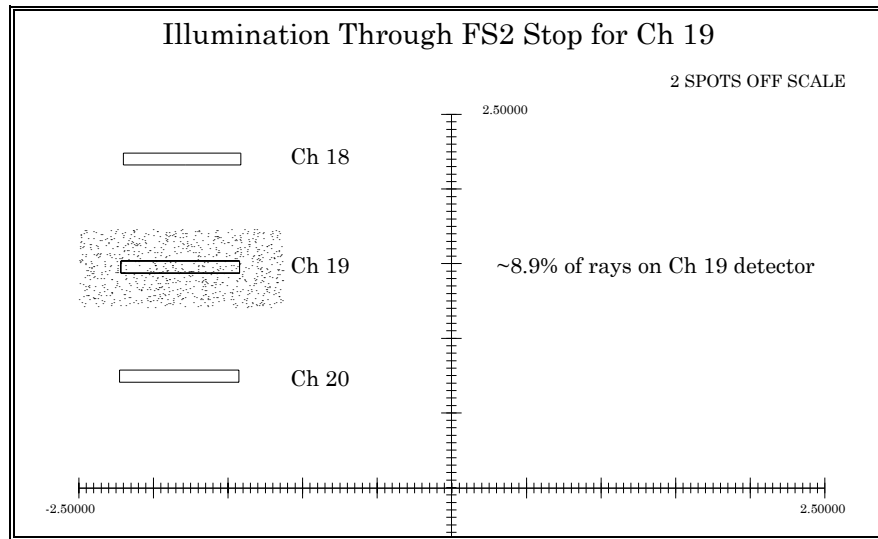


Figure x.x.x Illumination of the detector plane through Ch 19 FS2 aperture.

Ghost 22, from VW-S2 and VW-S1, is examined in the figure x.x.x, below. The result is remarkable because so little of the ghost energy ($< 1/10$) striking detector 19 ever gets to either 18 or 22. On the other hand, almost as many rays are ghosted onto channel 22 (5.3%) as originally strike the detector (8.9%). Fortunately, they are attenuated to .09% of the transmittance of the original rays. But the striking localization of this ghost cannot be inferred from any of the data listed in table x.x.x.

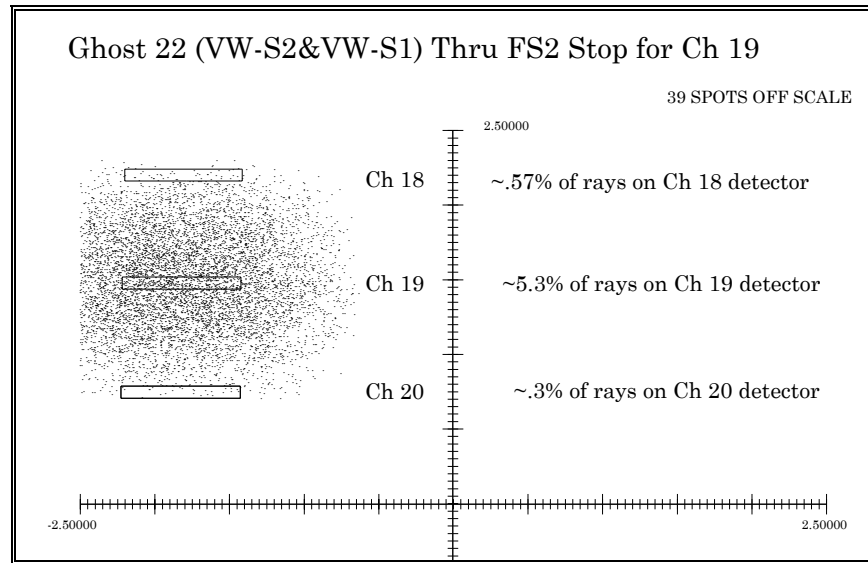


Figure x.x.x Ghost 22 is strongly localized to the producing channel

Ghost 35 and 36 is potentially worrisome because of the high reflectivity and GCR. But as figure x.x.x below proves, this ghost is harmless and produces no crosstalk at all. (There may still be some effect on the Vertical Response Profile if this energy exceeds the diffraction energy out to 3 km in the wings.)

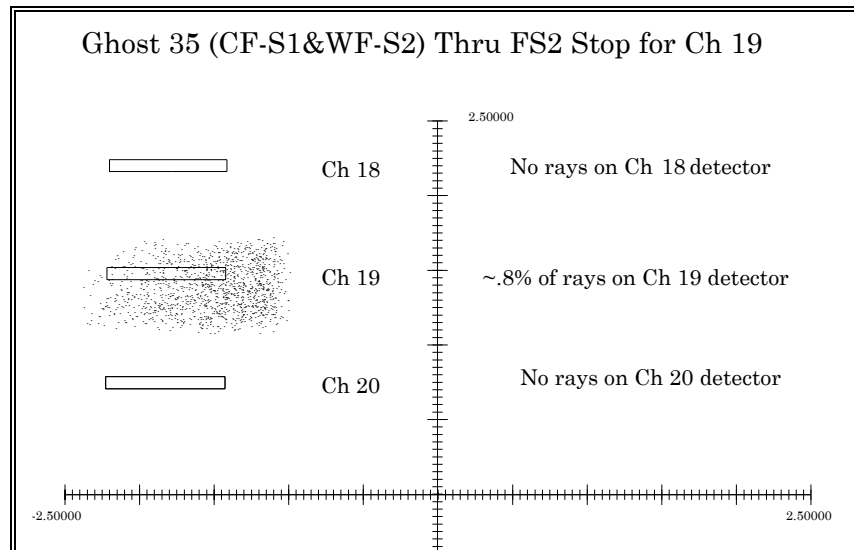


Figure x.x.x The very strong ghost 35 (&36) produces no crosstalk

Ghost 31 is the strongest of the remaining diffuse non-vignetting ghost images. With the high relative transmission of 8.5%, and a GCR of 82, it is well worth exploring. Figure x.x.x below shows that only a very small amount of the energy actually arrives at the detector. This is the type of ghost which could be correctly treated by the GCR alone.

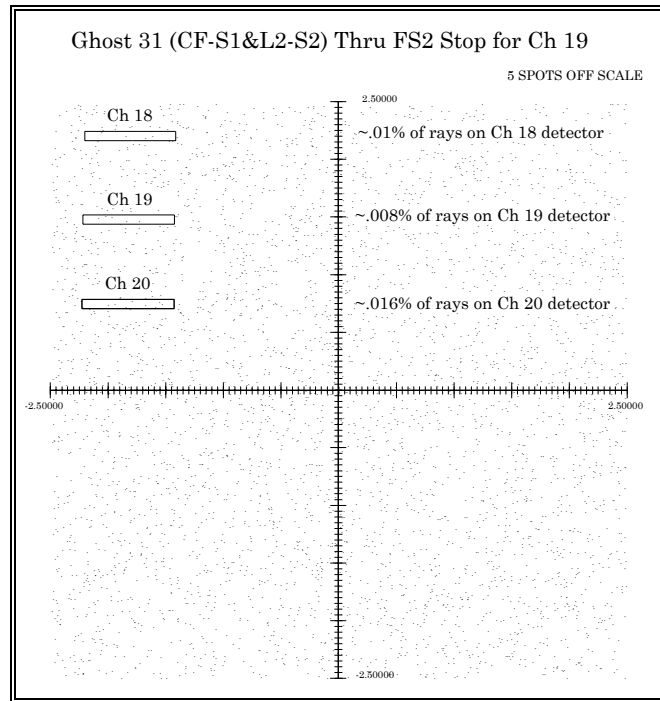


Figure x.x.x The illumination from ghost 31 is classically uniform.

11.0 LOS vector sensitivity table (los-sens.doc)

The line of sight (LOS) is the direction of the projected optical axis (POA) ray, which is the ray passing through the center of the detector and the SAS. If optical elements are shifted from their nominal position, particularly by thermal-elastic effects in orbit, the LOS may also shift. For HIRDLS, only the component of LOS shift along the elevation direction is of concern, and only that component is reported here. (The azimuth component is always computed, but is currently ignored.)

This chapter shows the vector LOS sensitivities to element perturbations. The sign and magnitude of the LOS shift is reported for a unit positive shift of each of the 6 degrees of freedom for each element. The units are [microradians (LOS) / micron (shift)], and [microradians (LOS) / microradian (tilt)].

This is done not only for the POA ray, but also for an average corner ray (a ray traced from each corner of the CFOV, and the average of the four vertical shifts is reported). Some perturbations can produce a scale change as well as an LOS shift. For example, if a lens is moved along its axis, the POA is not shifted at all, but the corner rays do have an LOS shift. Since the corner rays usually track the POA ray, only the *incremental* LOS shift is reported for the corner rays.

Finally, the POA LOS shift is also reported for the case when the scan mirror is pointing to the nominal 43 degree field of regard. The sensitivities are quite different in this direction partly because the projected coordinate system is itself rotated, and partly because of the compound incident angle on the scan mirror.

11.1 Clarification of coordinate directions

All the sensitivities described above are reported for two coordinate cases. One is the global coordinates of the IRCF. This is suitable for analysing the results of FEM perturbation studies. The other case is for the local coordinates of each element. This provides data and insight for the optical-mechanical engineering of the optical bench.

Special attention must be paid to the way OPTIMA handles rotations. The coordinates are conventionally right handed, and rotations are taken in the conventional rX, rY, rZ order (rotations about the X, Y, & Z axes in turn). However, the positive rotations are not all right handed as is the convention in many FEM programs. In OPTIMA, the three rotations are left, left, right, in the order just described. All the sensitivities reported here are consistent with this OPTIMA convention.

The element local coordinates are oriented such that for the telescope optics, the local +Y-axes are aligned more or less parallel to the IRCF +Z-axis. After the fold, the local +Y axes intercept a meridional ray at the same values as without the fold.

11.2 Element LOS sensitivities to solid body perturbations in IRCF coordinates

The data is reported in two tables below in order to keep a reasonable table size. The sensitivities to *linear* offsets along directions parallel to the IRCF axes are in table x.x.x.x, and the sensitivities to *angular* errors around axes parallel to the IRCF axes are in table

x.x.x below. Unless otherwise specified in notes, all angular errors are about vertices in the center of the elements.

Table x.x.x Vector Sensitivities for Linear Solid Body Perturbations: *IRCF*

Vertical LOS Sensitivity: (microradians / (+) μm offset) (1) Perturbations are in the GLOBAL IRCF coordinates									
Offset →	δX			δY			δZ		
Elements ↓	Center @ 0	Corner ² @ 0	Center @ 43	Center @ 0	Corner ² @ 0	Center @ 43	Center @ 0	Corner ² @ 0	Center @ 43
Scan Mirror	0	0	0	0	0	0	0	0	0
Primary	+0.030	+0.047	+0.028	0	0	-.651	-2.220	-.001	-2.123
Secondary	-.285	-.079	-.272	0	0	+.879	+2.957	-.025	+2.828
Ge Lens 1	+.168	+.057	+.161	0	0	-.151	-.487	+.028	-.465
Fold Mirror	-.097	-.017	-.148	-.108	-.019	-.165	-.093	-.017	-.142
Ge Lens 2	+3.009	-.081	+3.773	+1.775	+.094	+1.425	-2.571	+.115	-1.598
Vac Window	0	0	0	0	0	0	0	0	0
Detector	-2.827	+.074	-3.544	-1.668	-.075	-1.339	+2.415	-.100	+1.501

Notes:

- (1) A positive LOS shift means the LOS has moved away from the earth.
- (2) Corner values are incremental to center values.

Table x.x.x Vector Sensitivities for Angular Solid Body Perturbations: *IRCF*

Vertical LOS Sensitivity: (microradians / (+) $\mu\text{-rad}$ tilt) (1) Perturbations are in the GLOBAL IRCF coordinates (2)									
Tilt →	$\delta rX (\alpha)$			$\delta rY (\beta)$			$\delta rZ (\gamma)$		
Elements ↓	Center @ 0	Corner ³ @ 0	Center @ 43	Center @ 0	Corner ³ @ 0	Center @ 43	Center @ 0	Corner ³ @ 0	Center @ 43
Scan Mirror	0	0	+.686	+2.000	0	+1.870	0	0	+.530
Primary ⁴	0	0	-.129	-2.000	-.003	-1.912	0	0	-.558
Secondary ⁴	0	0	-.038	-.600	+.007	-.574	0	0	-.171
Ge Lens 1 ⁵	0	0	0	+.001	0	+.001	0	0	0
Fold Mirror	+.065	-.001	+.035	-.113	+.002	-.119	-.063	+.001	-.102
Ge Lens 2 ⁵	-.006	0	-.004	+.002	0	+.003	+.006	0	+.007
Vac Window	+.003	0	+.004	-.001	0	-.002	-.003	0	-.004
Detector	0	0	0	0	0	0	0	0	0

Notes:

- (1) A positive LOS shift means the LOS has moved away from the earth
- (2) Alpha is a tilt about the IRCF x-axis, beta about the y-axis, gamma about the z-axis.
- (3) Corner values are incremental to center values.
- (4) Tilts are about the intersection point of the gut ray with the surface
- (5) Lens tilts are about the second surface of each lens.

11.3 Element LOS sensitivities to solid body perturbations in LOCAL coordinates

Table x.x.x Vector Sensitivities for Linear Solid Body Perturbations: *LOCAL*

Vertical LOS Sensitivity: (microradians / (+) μm offset) (1) Perturbations are in the LOCAL coordinates of each element									
Offset →	δX			δY			δZ		
Elements ↓	Center @ 0	Corner ² @ 0	Center @ 43	Center @ 0	Corner ² @ 0	Center @ 43	Center @ 0	Corner ² @ 0	Center @ 43
Scan Mirror	0	0	0	0	0	0	0	0	0
Primary	0	0	+0.651	-2.020	-0.021	-1.931	+0.922	-0.043	+0.882
Secondary	0	0	+0.470	+2.735	+0.016	+2.701	-1.161	+0.082	-1.147
Ge Lens 1	0	0	+0.151	-0.515	+0.007	-0.492	0	-0.063	0
Fold Mirror	0	0	0	0	0	0	+0.173	+0.031	+0.119
Ge Lens 2	0	0	+1.271	-4.338	+0.086	-4.148	0	-0.145	0
Vac Window	0	0	0	0	0	0	0	0	0
Detector	0	0	-1.194	+4.075	-0.080	+3.896	0	+0.121	0

Notes:

- (1) A positive LOS shift means the LOS has moved away from the earth
- (2) Corner values are incremental to center values.

Table x.x.x Vector Sensitivities for Angular Solid Body Perturbations: *LOCAL*

Vertical LOS Sensitivity: (microradians / (+) $\mu\text{-rad}$ tilt) (1) Perturbations are in the LOCAL coordinates of each element (2)									
Tilt →	$\delta rX (\alpha)$			$\delta rY (\beta)$			$\delta rZ (\gamma)$		
Elements ↓	Center @ 0	Corner ³ @ 0	Center @ 43	Center @ 0	Corner ³ @ 0	Center @ 43	Center @ 0	Corner ³ @ 0	Center @ 43
Scan Mirror	-2.000	0	-1.871	0	0	-0.530	0	0	+0.686

Primary ⁴	+2.000	+0.003	+1.912	0	0	+0.560	0	0	+0.122
Secondary ⁴	+0.600	-0.007	-0.094	0	0	-0.088	0	0	-0.030
Ge Lens 1 ⁵	-0.001	0	-0.001	0	0	0	0	0	0
Fold Mirror	+0.116	-0.002	+0.125	+0.086	-0.001	-0.059	0	0	0
Ge Lens 2 ⁵	-0.009	0	-0.009	0	0	-0.003	0	0	0
Vac Window	-0.005	0	+0.004	0	0	+0.001	0	0	0
Detector	0	0	0	0	0	0	0	0	0

Notes:

- (1) A positive LOS shift means the LOS has moved away from the earth.
- (2) Alpha is a tilt about the element x-axis, beta about the y-axis, gamma about the z-axis.
- (3) Corner values are incremental to center values.
- (4) Tilts are about the intersection point of the gut ray with the surface.
- (5) Lens tilts are about the second surface of each lens.

11.3 Selected group LOS sensitivities to solid body shifts in IRCF coordinates

The LOS sensitivities for groups of elements are typically different from the effects of the elements in the groups. Groups which make sense to analyse should be tightly bound together by mechanical design. Even though the optical-mechanical concepts are not mature at this time, the groups selected in the tables below seem to be reasonable selections. Only IRCF-based perturbations have been analysed for presentation.

Table x.x.x Vector Sensitivities for Linear Group Perturbations: *IRCF*

Vertical LOS Sensitivity: (microradians / (+) μm offset) (1) Perturbations are in the GLOBAL IRCF coordinates									
Offset →	δX			δY			δZ		
Group ↓	Center @ 0	Corner ² @ 0	Center @ 43	Center @ 0	Corner ² @ 0	Center @ 43	Center @ 0	Corner ² @ 0	Center @ 43
Scan Mirror to ILS	-0.255	-0.032	-0.244	0	0	+0.229	+0.737	-0.026	+0.705
FS2 to Detector	+0.255	+0.032	+0.244	0	0	-0.229	-0.737	+0.026	-0.705
FS2 to L2	+3.082	-0.041	+3.788	+1.668	+0.075	+1.110	-3.153	+0.126	-2.206
L2 to detector	+0.182	-0.008	+0.228	+0.107	+0.019	+0.086	-0.156	+0.014	-0.097
SAS to detector	+0.184	-0.008	+0.231	+0.108	+0.019	+0.087	-0.157	+0.014	-0.098

Notes

- (1) A positive LOS shift means the LOS has moved away from the earth.
- (2) Corner values are incremental to center values.

Table x.x.x Vector Sensitivities for Angular Group Perturbations: *IRCF*

Vertical LOS Sensitivity: (microradians / (+) μ -rad tilt) (1) Perturbations are in the GLOBAL IRCF coordinates (2)									
Tilt \rightarrow	δrX (α)			δrY (β)			δrZ (γ)		
Group \downarrow	Center @ 0	Corner ³ @ 0	Center @ 43	Center @ 0	Corner ³ @ 0	Center @ 43	Center @ 0	Corner ³ @ 0	Center @ 43
Scan Mirror to ILS ⁴	0	0	+.540	+.787	+.004	+.581	0	0	+.206
FS2 to Detector ⁵	-.135	+.005	-.122	-.135	+.006	-.129	+.047	+.006	0
FS2 to L2 ⁶	-.022	+.002	-.043	-.163	+.006	-.171	-.049	+.007	-.112
L2 to detector ⁵	-.104	+.002	-.069	+.032	-.001	+.048	+.100	-.002	+.121
SAS to detector ⁵	-.104	+.002	-.069	+.032	-.001	+.048	+.100	-.002	+.121

Notes:

- (1) A positive LOS shift means the LOS has moved away from the earth.
- (2) Alpha is a tilt about the element x-axis, beta about the y-axis, gamma about the z-axis.
- (3) Corner values are incremental to center values.
- (4) Tilt vertex is at center of the ILS.
- (5) Tilt vertex is at center of detector.
- (6) Tilt vertex is at center of L2.

One clear conclusion of the group sensitivities is that tight coupling of the relay group should include the detector. This will avoid the high offset sensitivity >3 mr/mm seen in table x.x.x, row 3 (FS2 to L2).

12.0 Diffraction image performance (difperf.doc)

12.1 Introduction

The requirements for the image quality at the detector in the imager are defined in the ITS section 3.3.2, *Vertical Response*. Analysis of the Vertical Response Profile (VRP) leads to the several specifications in that section. Detailed interpretation of the requirement is deferred to section 12.4 where the method of computation is also outlined.

The VRP specification is not a traditional measure of image quality. Computation of the elements of the VRP is somewhat involved, especially compared to more common diffraction image quality measures such as RMS wavefront error (WFE), Strehl ratio, MTF, knife edge response, or encircled energy. This chapter will show how the imager performs using selected traditional measures, as well as the VRP. It is the intent of this comparison to show why it may be valid, or invalid, to substitute a simpler measure of image quality for tolerance analysis and image error tree construction.

With that in mind, image quality is shown through focus wherever possible. Focus shift is the lowest order and simplest wavefront error which reduces diffraction image performance. Focus error is introduced to the wavefront, not to the prescription, for these analyses. Since many constructional or alignment errors (as well as environmentally induced perturbations in operation) produce a focus error, such a presentation constitutes a first look at sensitivity to this class of tolerances.

12.1.1 Deviation from isoplanatism

Each detector is long and thin and covers a significant fraction of the field of view in the azimuth direction. It is desirable that any image quality computation be valid over the whole detector, so that the wavefront only needs to be computed for one point (typically the center). If the wavefront or point spread function (PSF) changes “insignificantly” over each detector, then the part of the FOV associated with the detector is sufficiently isoplanatic to proceed, and only one wavefront must be computed and applied.

Three channels have been selected for a test of isoplanatism based on wavelength and location in the focal plane. Shorter wavelengths, and corner locations are more demanding.

The three figures on the next page demonstrate isoplanatism (or lack thereof) using geometric spot diagrams for channels 18, 21 and 10. This is a sensitive test because it is not smoothed by diffraction. Indeed, compared to the Airy disk first dark ring, the performance is extremely good! The spot diagrams shown are for the inner, center, and outer points of the long dimension of each channel.

For channel 18, which appears the least isoplanatic, the wavefront error was examined for the same three field points. The results summarized in table x.x.x below encourage the author to go ahead and assume that channel 18 is sufficiently isoplanatic for all diffraction computations, and therefore all channels. The centers of the channels will be used for wavefront generation.

Table x.x.x The worst case, channel 18, is sufficiently isoplanatic for diffraction computation.

Location	RMS WFE	Strehl	dz to best focus	RMS WFE	Strehl
	(waves)		(mm)	(waves)	
Inner	.02517	.9753	-.00497	.02247	.9803
Center	.01549	.9906	0.0000	.01549	.9906
Outer	.02358	.9783	+.00986	.006471	.9983

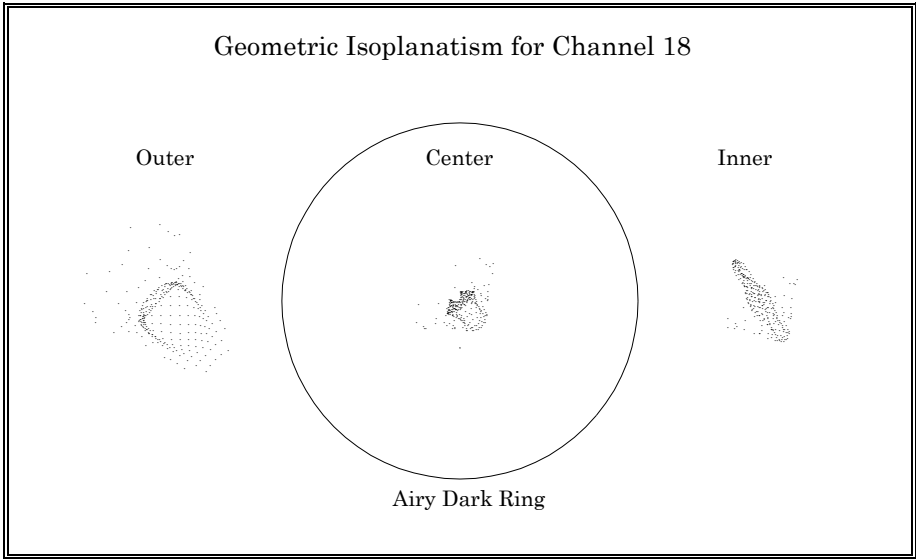


Figure x.x.x The spot diagrams along channel 18 are small compared to the Airy size

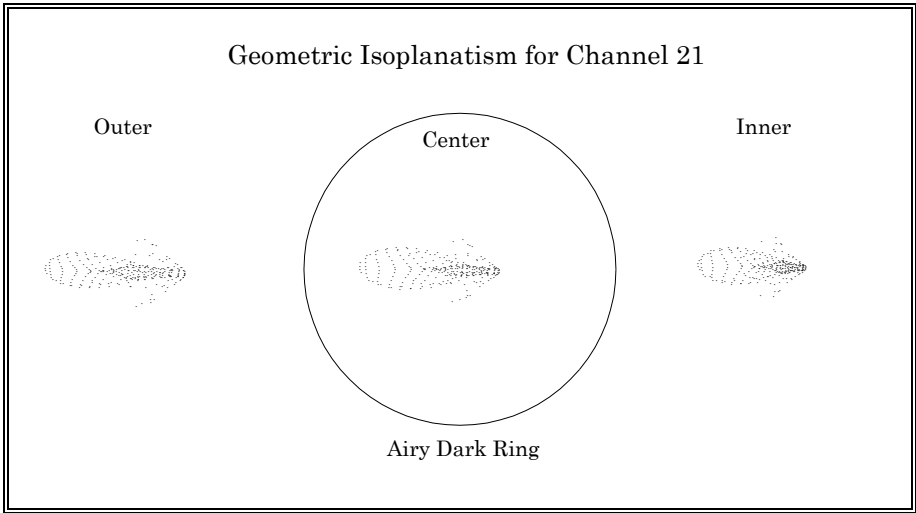


Figure x.x.x The geometric spot diagrams for channel 21 are remarkably isoplanatic

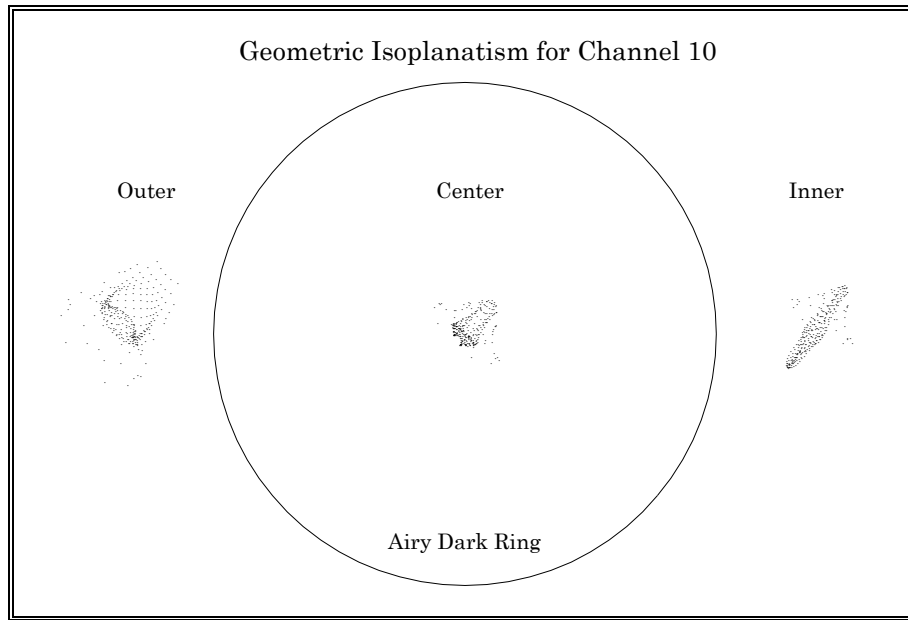


Figure x.x.x Isoplanatism for channel 10 is restored by a dominant diffraction spread

12.2 Wavefront error and Strehl ratio

Table x.x.x below shows that the imager has very low wavefront error in all channels. In the table, channel 23 is the alignment channel. The average adjustment for best focus is +1.4 microns, which is just a hint that the system is properly focused (but see section 12.3 for a definitive exhibit of best focus).

Since both RMS OPD (wavefront error) and Strehl ratio computations are specifically independent of spatial direction, these values before and after refocus may be somewhat misleading. The HIRDLS imager needs best image performance in the elevation direction, even at the expense of performance in the azimuth direction. Thus in the presence of astigmatism, for example, focus is best when the beam or spot is smallest in the elevation direction (local y-axis on the focal plane).

The best HIRDLS performance can be found only by adjusting focus until the maximum MTF in the local y-direction is achieved. This is explored through focus in section 12.3. For comparison purposes, through-focus data is presented first for wavefront error and Strehl ratio for several selected channels in the table following the next table.

Table x.x.x The imager is characterized by very high Strehl ratio performance

Config (Channel)	RMS OPD (waves)	Strehl Ratio	Refocus (mm)	Best RMS (waves)	Best Strehl Ratio
1	0.0025	0.9998	0.0006	0.0024	0.9998
2	0.0011	1.0000	-0.0009	0.0007	1.0000
3	0.0034	0.9996	0.0012	0.0031	0.9996
4	0.0101	0.9960	0.0044	0.0090	0.9968
5	0.0150	0.9911	0.0066	0.0133	0.9931
6	0.0122	0.9941	0.0051	0.0102	0.9959
7	0.0165	0.9893	-0.0032	0.0160	0.9900
8	0.0115	0.9948	-0.0019	0.0111	0.9951
9	0.0196	0.9849	0.0072	0.0165	0.9893
10	0.0125	0.9938	-0.0013	0.0124	0.9940
11	0.0198	0.9847	-0.0028	0.0192	0.9855
12	0.0248	0.9760	-0.0077	0.0205	0.9835
13	0.0247	0.9763	-0.0058	0.0219	0.9812
14	0.0277	0.9701	-0.0087	0.0217	0.9816
15	0.0268	0.9721	-0.0060	0.0238	0.9779
16	0.0256	0.9745	-0.0030	0.0248	0.9760
17	0.0151	0.9910	-0.0002	0.0151	0.9910
18	0.0155	0.9905	0.0004	0.0155	0.9906
19	0.0276	0.9703	-0.0029	0.0268	0.9720
20	0.0319	0.9607	-0.0068	0.0275	0.9707
21	0.0352	0.9523	-0.0085	0.0275	0.9705
23	0.0154	0.9907	0.0035	0.0122	0.9941

12.2.1 Through-focus WFE & Strehl ratio behavior of selected channels

Channels 2, 5, 10, 17, & 21 were selected because of their wavelength spread and dispersment over the focal plane for a brief through-focus study. The WFE as measured by RMS OPD tends to change linearly with defocus. For a fixed value of focus shift, the RMS OPD changes reciprocally with wavelength. Both of these features are clearly evident in figure x.x.x below.

The Strehl ratio S was computed here by exponentiation of the RMS OPD: $S = e^{-(2\pi\text{rms})^2}$. The plot of Strehl ratio vs. defocus is therefore a gaussian function to the extent that RMS OPD is linear with defocus.

The focus range selected is from -.100 to +.100 mm. This should imply nothing at all regarding any tolerance to be assigned later. It is simply a round and ample value.

Table x.x.x Through-focus WFE and Strehl ratio for selected channels

Channel	2	5	10	17	21		2	5	10	17	21
FOCUS	RMSOPD	RMSOPD	RMSOPD	RMSOPD	RMSOPD		STREHL	STREHL	STREHL	STREHL	STREHL
SHIFT	(WAVES)	(WAVES)	(WAVES)	(WAVES)	(WAVES)		RATIO	RATIO	RATIO	RATIO	RATIO
-0.1	0.09558	0.11494	0.16023	0.21859	0.23848		0.6972	0.5936	0.3629	0.1516	0.1059
-0.09	0.08594	0.10431	0.1441	0.19679	0.21279		0.7471	0.6508	0.4405	0.2168	0.1674
-0.08	0.0763	0.09369	0.12798	0.17501	0.18716		0.7947	0.7071	0.5238	0.2984	0.2509
-0.07	0.06666	0.0831	0.11189	0.15325	0.1616		0.8391	0.7614	0.61	0.3957	0.3567
-0.06	0.05702	0.07255	0.09582	0.13152	0.13617		0.8795	0.8124	0.6959	0.5052	0.4809
-0.05	0.04738	0.06205	0.0798	0.10984	0.11094		0.9152	0.859	0.7777	0.6211	0.6151
-0.04	0.03774	0.05164	0.06387	0.08824	0.08611		0.9453	0.9001	0.8513	0.7354	0.7462
-0.03	0.0281	0.04138	0.04809	0.06681	0.06214		0.9693	0.9346	0.9127	0.8384	0.8586
-0.02	0.01847	0.03142	0.03272	0.04579	0.04059		0.9866	0.9618	0.9586	0.9206	0.937
-0.01	0.00884	0.02218	0.01876	0.02617	0.0278		0.9969	0.9808	0.9862	0.9733	0.9699
0	0.00109	0.01503	0.01252	0.01511	0.03519		1.0000	0.9911	0.9938	0.991	0.9523
0.01	0.01049	0.01377	0.02203	0.02696	0.05517		0.9957	0.9925	0.981	0.9717	0.8868
0.02	0.02012	0.01956	0.03658	0.0467	0.07867		0.9841	0.985	0.9486	0.9175	0.7832
0.03	0.02976	0.02837	0.0521	0.06775	0.10332		0.9656	0.9687	0.8984	0.8343	0.6561
0.04	0.0394	0.03817	0.06792	0.08919	0.12845		0.9406	0.9441	0.8335	0.7305	0.5213
0.05	0.04904	0.04836	0.08389	0.11079	0.15383		0.9094	0.9118	0.7574	0.616	0.3929
0.06	0.05868	0.05873	0.09992	0.13247	0.17936		0.8729	0.8727	0.6742	0.5002	0.2808
0.07	0.06832	0.06921	0.116	0.15421	0.20497		0.8317	0.8277	0.5879	0.3911	0.1904
0.08	0.07796	0.07975	0.1321	0.17597	0.23064		0.7867	0.778	0.5021	0.2945	0.1224
0.09	0.0876	0.09032	0.14821	0.19775	0.25636		0.7386	0.7246	0.4201	0.2136	0.0747
0.1	0.09724	0.10093	0.16435	0.21955	0.28211		0.6884	0.6689	0.3443	0.1491	0.0432

The data in the table above is plotted in the two figures below. One feature especially evident is the fact that these 5 channels, in terms of RMS OPD and Strehl ratio, are not parafocal. Since the channels were optimized for best behavior in the elevation direction, they are in best “focus” only in that direction. This will be evident in the through-focus MTF plot in section 12.3

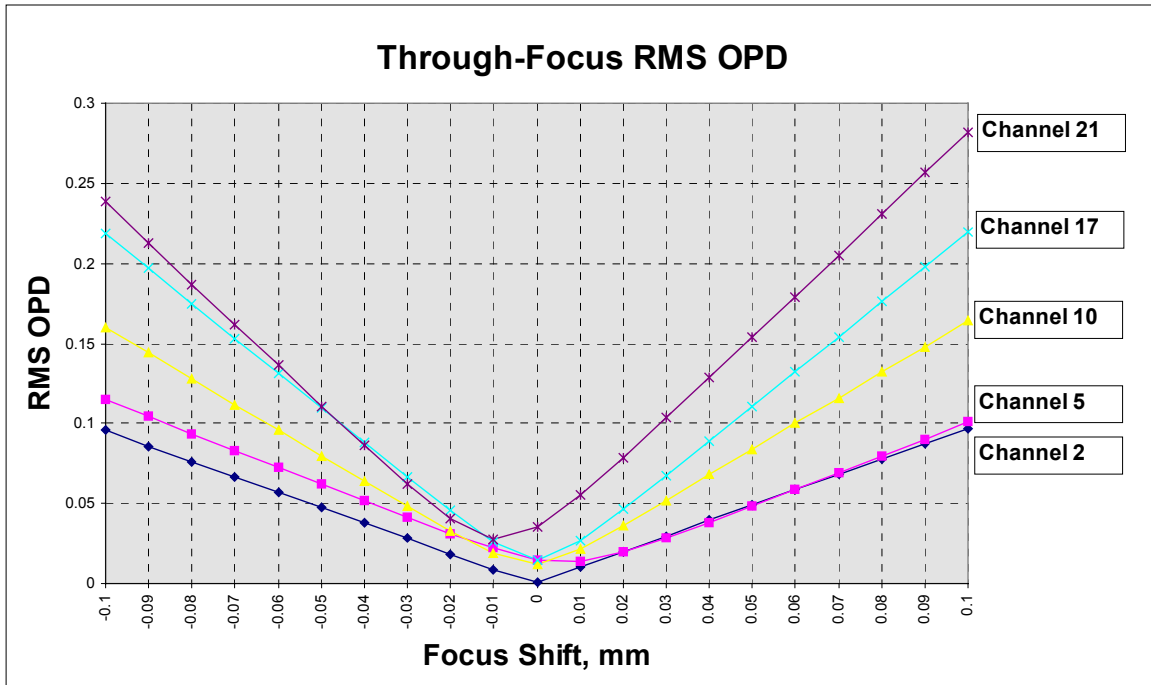


Figure x.x.x Through-focus behavior for wavefront RMS OPD for 5 selected channels.

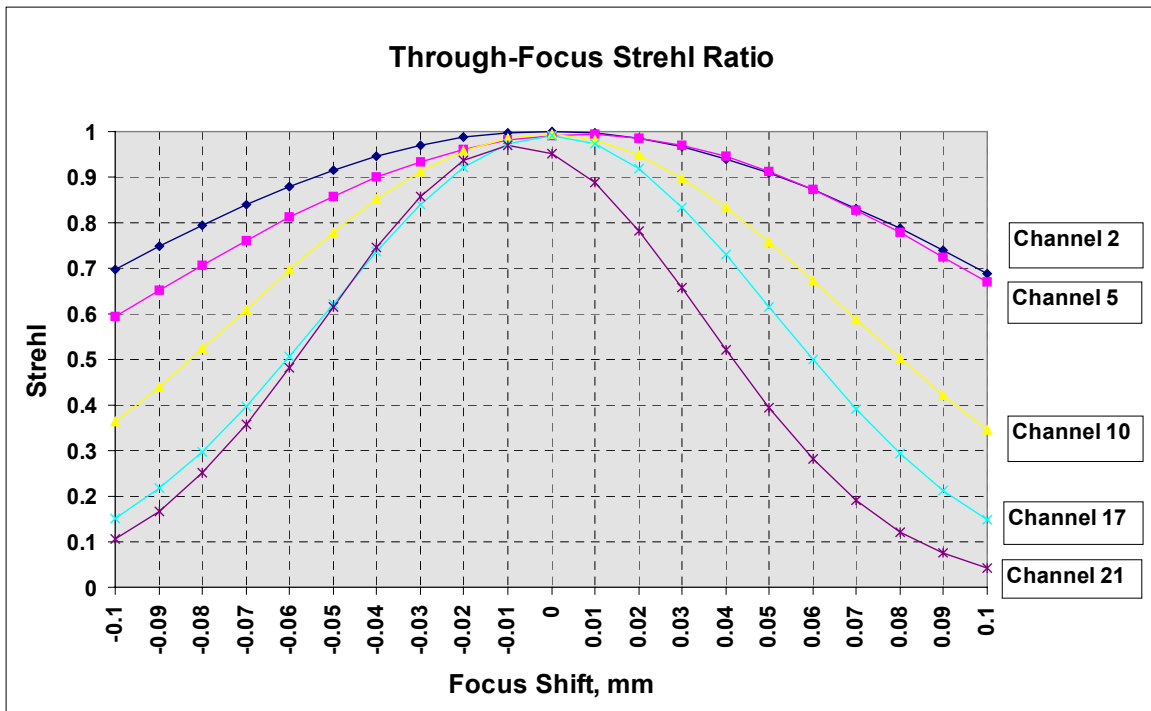


Figure x.x.x Through-focus behavior of Strehl ratio for 5 selected channels shows that the channels are not parafocal for a conventional round spot requirement.

12.3 MTF at detector Nyquist frequency, with through-focus data

While RMS OPD and Strehl ratio have the advantage of indicating diffraction performance with a single number, that is also the disadvantage. The HIRDLS performance requirement is directional - along the elevation axis. There is no convenient method to separate either RMS OPD or Strehl ratio into directional components. (If that were possible, a great deal of computing time could be saved, with possible very great benefit for tolerance analysis for HIRDLS).

12.3.1 Relevance of MTF to HIRDLS

MTF is a far more detailed measure of diffraction performance, but with the disadvantages that it is a 2-dimensional function, and requires much more computation. Fortunately for HIRDLS, a single relevant number can be extracted from the MTF sheet.

The relevant point on the MTF function lies along the local y-axis of the MTF (parallel to the elevation axis), at the detector Nyquist spatial frequency. (Since the MTF always exhibits point symmetry, either value with respect to zero can be selected). The Nyquist frequency is the spatial sine wave with period exactly twice the detector height. For a detector with a height of .080 mm, the Nyquist frequency is 6.25 line-pairs/mm. (A sine-wave is equivalent to a bright-dark pair of lines).

12.3.2 Computation and display of through-focus MTF data

The wavefront was developed for each channel using 6000 rays. A focus error was introduced into the wavefront numerically as an independent variable, from -0.100 to +.0100 mm. The diffraction point spread function (PSF) was computed by Fourier transform, then the MTF was computed by another Fourier transform. The point on the data array at 6.25 lp/mm was extracted and placed in a file. The 21 data files for all 21 channels are shown in table x.x.x on the next page.

The MTF in focus is the center row in bold print. This should be compared to the aberration-free MTF printed along the bottom row, computed by setting the phase term to zero over the wavefront. In terms of MTF along the Y-axis at Nyquist frequency, the HIRDLS imager is an extremely well corrected design. The worst case is channel 19 where the focused MTF is only 0.15% less than the perfect MTF !

On the page following the table, the through-focus MTF data is plotted in a single overlay for all 21 channels in figure x.x.x. Note the remarkable consistency of focus in contrast to the through focus of Strehl ratio. In the elevation direction, the HIRDLS channels are exquisitely par focal.

TABLE X.X.X Through-Focus MTF @ 6.25 lp/mm (Detector Nyquist frequency)

RAL-33E optical design. 6000 rays traced from the center of each channel with the SAS as pupil and reference surface. Focus shift introduced into the wavefront as a post-process; rays were not retraced in the presence of a prescription perturbation. Aberration-free MTF found by setting the phase part of the pupil function to zero.

Channel:	1	2	3	4	5	6	7	8	9	10	11	12	13	14	15	16	17	18	19	20	21
FOCUS	MTF	MTF	MTF	MTF	MTF	MTF	MTF	MTF	MTF	MTF	MTF	MTF	MTF	MTF	MTF	MTF	MTF	MTF	MTF	MTF	MTF
(mm)																					
-0.10	0.6929	0.7002	0.7031	0.7076	0.7114	0.7285	0.7313	0.7383	0.7373	0.7464	0.7459	0.7568	0.7551	0.7614	0.7590	0.7606	0.7603	0.7602	0.7641	0.7679	0.7718
-0.09	0.7131	0.7211	0.7244	0.7293	0.7337	0.7533	0.7563	0.7637	0.7635	0.7731	0.7729	0.7841	0.7834	0.7895	0.7875	0.7892	0.7897	0.7901	0.7934	0.7973	0.8017
-0.08	0.7315	0.7401	0.7438	0.7490	0.7540	0.7761	0.7791	0.7869	0.7874	0.7975	0.7975	0.8090	0.8093	0.8152	0.8136	0.8154	0.8166	0.8175	0.8202	0.8242	0.8290
-0.07	0.7479	0.7571	0.7612	0.7666	0.7722	0.7965	0.7995	0.8076	0.8089	0.8194	0.8197	0.8314	0.8326	0.8383	0.8371	0.8389	0.8408	0.8421	0.8443	0.8484	0.8537
-0.06	0.7624	0.7720	0.7765	0.7820	0.7881	0.8145	0.8175	0.8258	0.8279	0.8387	0.8392	0.8510	0.8532	0.8586	0.8577	0.8596	0.8621	0.8639	0.8655	0.8697	0.8753
-0.05	0.7747	0.7848	0.7895	0.7952	0.8017	0.8299	0.8329	0.8412	0.8442	0.8551	0.8560	0.8678	0.8709	0.8759	0.8755	0.8773	0.8804	0.8826	0.8836	0.8879	0.8939
-0.04	0.7848	0.7952	0.8002	0.8060	0.8128	0.8427	0.8456	0.8539	0.8576	0.8686	0.8698	0.8816	0.8855	0.8902	0.8901	0.8918	0.8955	0.8981	0.8986	0.9029	0.9091
-0.03	0.7927	0.8034	0.8086	0.8144	0.8214	0.8527	0.8555	0.8637	0.8682	0.8791	0.8807	0.8923	0.8970	0.9013	0.9016	0.9032	0.9073	0.9102	0.9102	0.9146	0.9210
-0.02	0.7983	0.8092	0.8145	0.8203	0.8274	0.8599	0.8625	0.8705	0.8757	0.8865	0.8884	0.8998	0.9053	0.9092	0.9098	0.9112	0.9156	0.9189	0.9185	0.9229	0.9294
-0.01	0.8015	0.8125	0.8180	0.8237	0.8308	0.8642	0.8667	0.8743	0.8802	0.8907	0.8930	0.9041	0.9103	0.9138	0.9147	0.9159	0.9206	0.9241	0.9233	0.9277	0.9343
0.00	0.8024	0.8135	0.8190	0.8245	0.8316	0.8656	0.8679	0.8751	0.8816	0.8917	0.8945	0.9052	0.9120	0.9150	0.9162	0.9171	0.9220	0.9258	0.9246	0.9290	0.9357
0.01	0.8010	0.8120	0.8176	0.8228	0.8297	0.8642	0.8661	0.8728	0.8800	0.8896	0.8927	0.9030	0.9104	0.9129	0.9143	0.9150	0.9199	0.9239	0.9224	0.9268	0.9334
0.02	0.7972	0.8081	0.8136	0.8185	0.8252	0.8598	0.8615	0.8675	0.8752	0.8843	0.8878	0.8976	0.9055	0.9074	0.9091	0.9094	0.9143	0.9184	0.9168	0.9210	0.9276
0.03	0.7911	0.8018	0.8072	0.8118	0.8181	0.8525	0.8539	0.8592	0.8674	0.8758	0.8798	0.8889	0.8972	0.8987	0.9006	0.9005	0.9052	0.9095	0.9076	0.9118	0.9183
0.04	0.7827	0.7932	0.7984	0.8025	0.8085	0.8425	0.8435	0.8480	0.8567	0.8643	0.8687	0.8772	0.8858	0.8867	0.8888	0.8882	0.8928	0.8971	0.8951	0.8993	0.9055
0.05	0.7721	0.7822	0.7873	0.7909	0.7963	0.8297	0.8303	0.8340	0.8430	0.8497	0.8546	0.8623	0.8712	0.8716	0.8738	0.8728	0.8771	0.8814	0.8794	0.8834	0.8894
0.06	0.7593	0.7690	0.7738	0.7769	0.7817	0.8142	0.8145	0.8172	0.8264	0.8323	0.8376	0.8446	0.8536	0.8535	0.8558	0.8543	0.8582	0.8625	0.8604	0.8644	0.8701
0.07	0.7444	0.7536	0.7582	0.7607	0.7648	0.7961	0.7961	0.7978	0.8072	0.8121	0.8178	0.8240	0.8331	0.8325	0.8348	0.8328	0.8362	0.8405	0.8385	0.8423	0.8476
0.08	0.7275	0.7362	0.7404	0.7423	0.7457	0.7756	0.7752	0.7759	0.7854	0.7894	0.7954	0.8008	0.8099	0.8087	0.8111	0.8086	0.8115	0.8156	0.8137	0.8174	0.8223
0.09	0.7087	0.7168	0.7207	0.7219	0.7245	0.7528	0.7520	0.7516	0.7612	0.7641	0.7706	0.7750	0.7841	0.7824	0.7848	0.7817	0.7840	0.7880	0.7862	0.7898	0.7943
0.10	0.6881	0.6955	0.6990	0.6995	0.7013	0.7279	0.7267	0.7252	0.7348	0.7366	0.7434	0.7470	0.7559	0.7537	0.7561	0.7525	0.7541	0.7579	0.7563	0.7598	0.7639
Aberration																					

Free	0.8025	0.8135	0.8191	0.8247	0.8318	0.8659	0.8690	0.8757	0.8818	0.8923	0.8956	0.9059	0.9126	0.9152	0.9170	0.9185	0.9225	0.9262	0.9260	0.9299	0.9360
------	--------	--------	--------	--------	--------	--------	--------	--------	--------	--------	--------	--------	--------	--------	--------	--------	--------	--------	--------	--------	--------

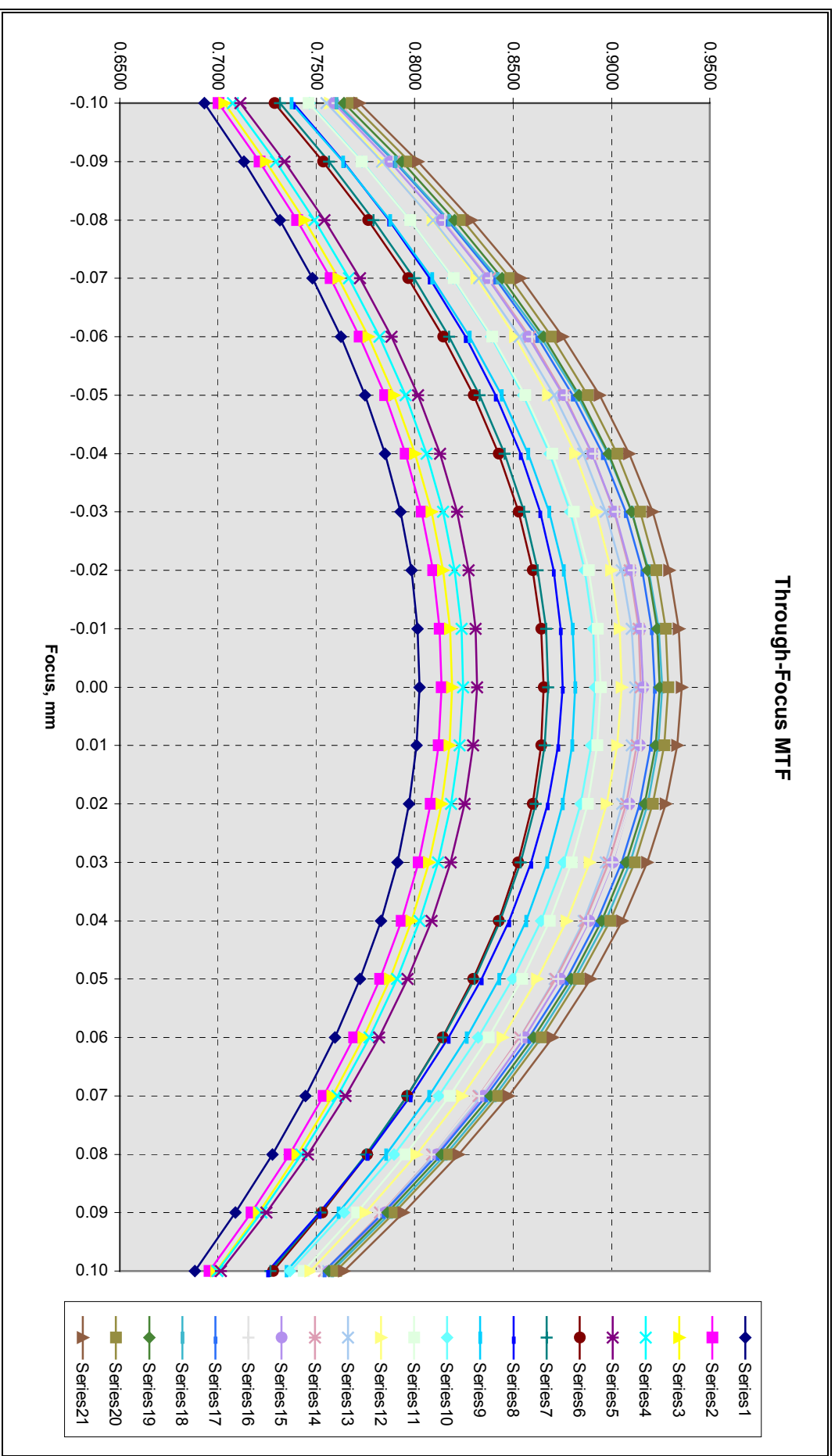


FIGURE X.X.X Plot of MTF (Elevation Direction) through focus shows that each channel is extremely well focused.

12.4 Vertical Response Profile (VRP) & derived performance data

In the broadest terms, the computation of VRP for each channel follows the path outlined below:

1. Generation of wavefront by raytrace. (Raycount must be sufficient)
2. Compute the diffraction PSF by Fourier methods. (Sufficient Airy rings)
3. Define the detector and convolve with the PSF. (Must extend beyond 5-6 km)
4. Integrate the convolution data in rows parallel to the horizon. (This is the VRP)
5. Analyze the VRP data to get the ITS requirements.
 - a. Interpolate to find 50% points, and FWHM
 - b. Integrate full VRP to get “total response”. (Largest systematic error here)
 - c. Integrate partial VRP ranges to get 50%, .75 km, 1-4 km integ. responses.

12.4.1 Interpretation of the ITS Vertical response requirement sections 3.3.1 and 3.3.3.1

In table x.x.x below, The ITS requirement is carefully dissected and examined. Comments regarding computational methods are made in the right column.

Table x.x.x Interpretation and computation of the ITS Vertical response

#	ITS Statement	Computational method
a	3.3.2 Vertical response The end-to-end response of each spectral channel to a line source perpendicular to the ILOS, parallel to the IRCF X-Y plane, and moving parallel to the IRCF Z axis shall be a function ...	The Vertical Response Function or Profile (VRP) is computed as follows: The diffraction PSF is convolved with the ideal detector (section 8.1.3). The integrated data of each row (parallel to the azimuth) vs location of the row on the focal plane is the image VRP. The peak is normalized to 1.0.
b	...with a full width at half maximum (FWHM) of 1.00 km +0.05/-0.1 km.	Interpolation is made to .50, each side of the peak, and multiplied by the plate scale. FWHM is the separation between locations in km.
c	The integrated vertical response between the half-maximum points must be at least 80% of the total integrated response.	The total integrated response is the area under the full VRP data array. An interpolating data integrator finds the area under the FWHM. The area ratio (x 100%) is reported.
d	Define the center of the vertical IFOV as the midpoint between the half-maximum points and let Dz be the distance (in km at the limb) from this center.	No analytical problem. Object coordinates in km converted to image coordinates by a local plate scale determined for each channel by raytrace.
e	Then for Dz = 0.75 km, the integrated response over the spatial interval -Dz to +Dz must be at least (100 - 0.4λ)% of the total integrated response, where λ is the central wavelength (in μm) of the channel.	The total is already determined as above. Interpolate with plate scale to find .75 km from midpoint in image. Straight forward to integrate data between image coordinates, with interpolation.

f	...for $1 \leq Dz \leq 4$, the integrated response over the spatial interval $-Dz$ to $+Dz$ must be at least $(100 - 0.25\lambda / Dz^{1.15})\%$ of the total integrated response.	Actually defines a function, not a number ! Data points at $\pm 1, 2, 3, 4$, km are found, and the area under the VRP data computed as above. The ratios to the total area are reported, and compared to the function required of that point.
g	...and for $Dz > 4$, the vertical response function shall be governed by the Out-of-Field Response requirement in Section 3.3.5.	Not covered in TC-LOC-12.
h	3.3.3 Vertical Response Stability 3.3.3.1 Within a Single Channel The long-term stability of the vertical IFOV profile of each channel between the initially determined 0.2% relative response points...	(Assume that the vertical IFOV profile is the same as the VRP.) The baseline VRP data is saved for each channel. Thresholding above the .002 level will occur later. A new perturbed VRP is produced and compared to the baseline VRP.
i	...shall be such that the relative response averaged over any interval equal to one tenth of the IFOV in the vertical spatial dimension...	One tenth of the IFOV is taken to mean 0.1 km, or ~ 8 microns on the focal plane.
j	...shall not change by more than 0.5% of the maximum response, over the lifetime of the Instrument in orbit.	For a perturbed normalized VRP, if the ratio R_i of the data points, over any 0.1 km range, to the baseline VRP data points lies outside the range $0.995 < R_i < 1.005$, this specification is exceeded.

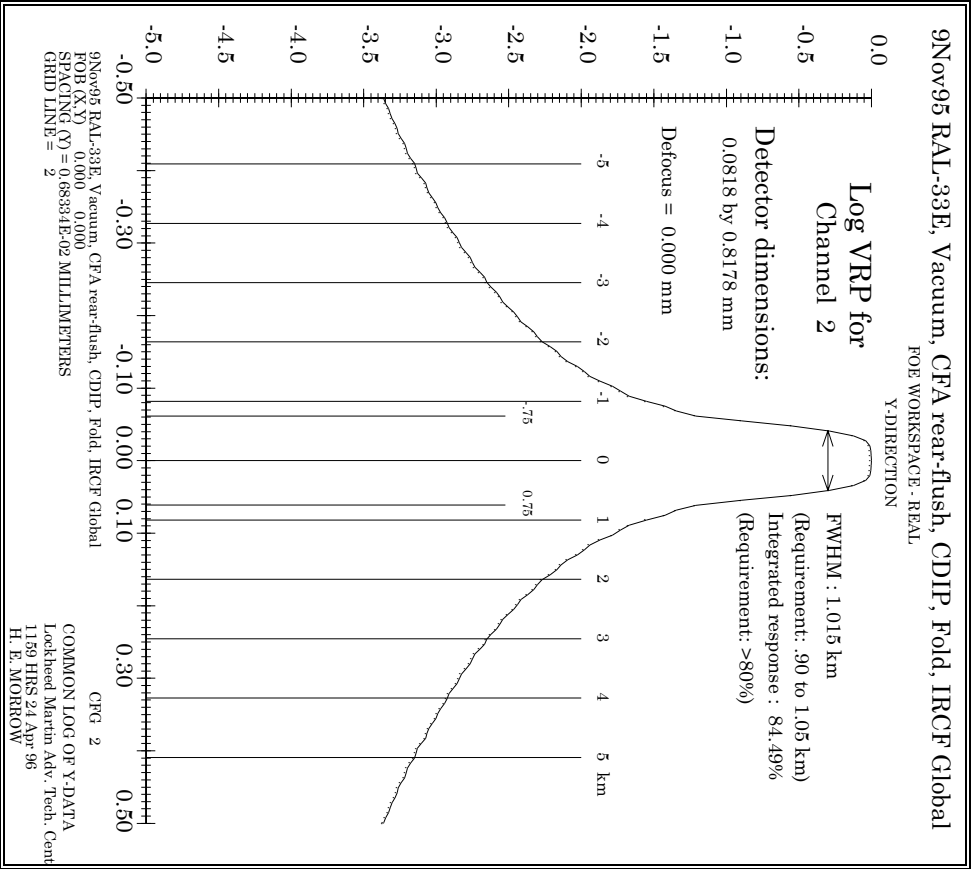
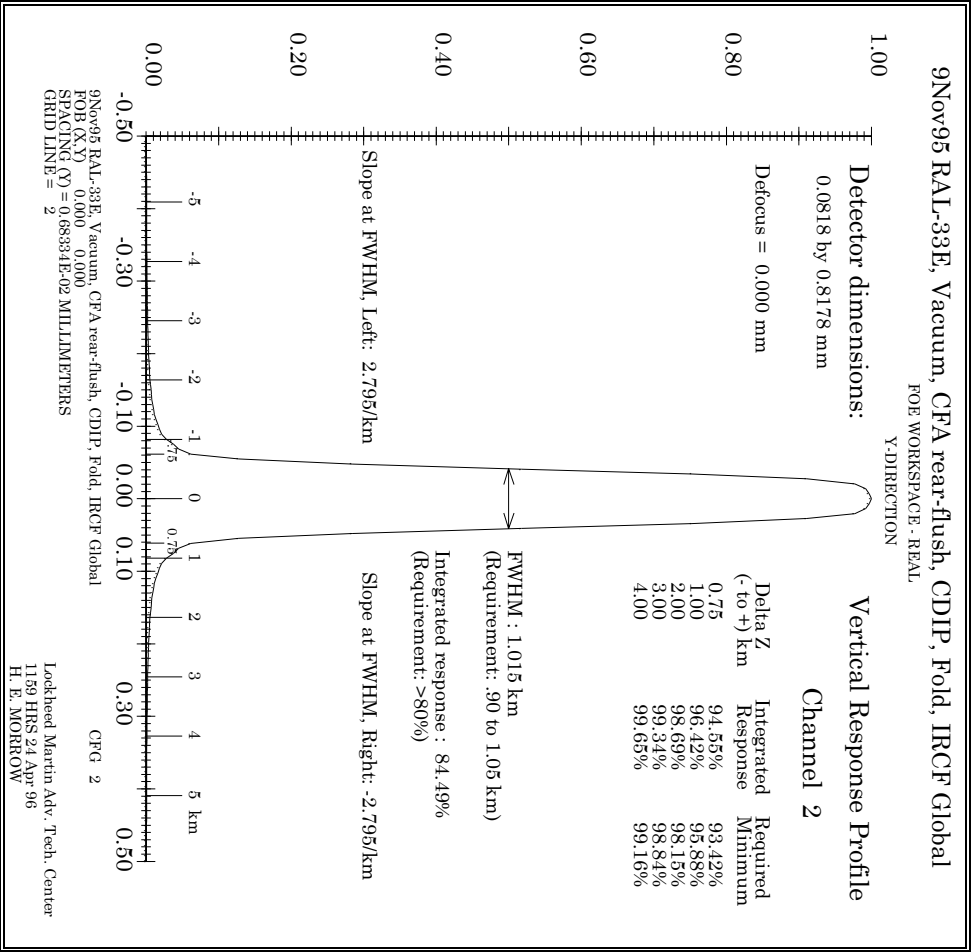
12.4.2 Baseline Computed VRP data.

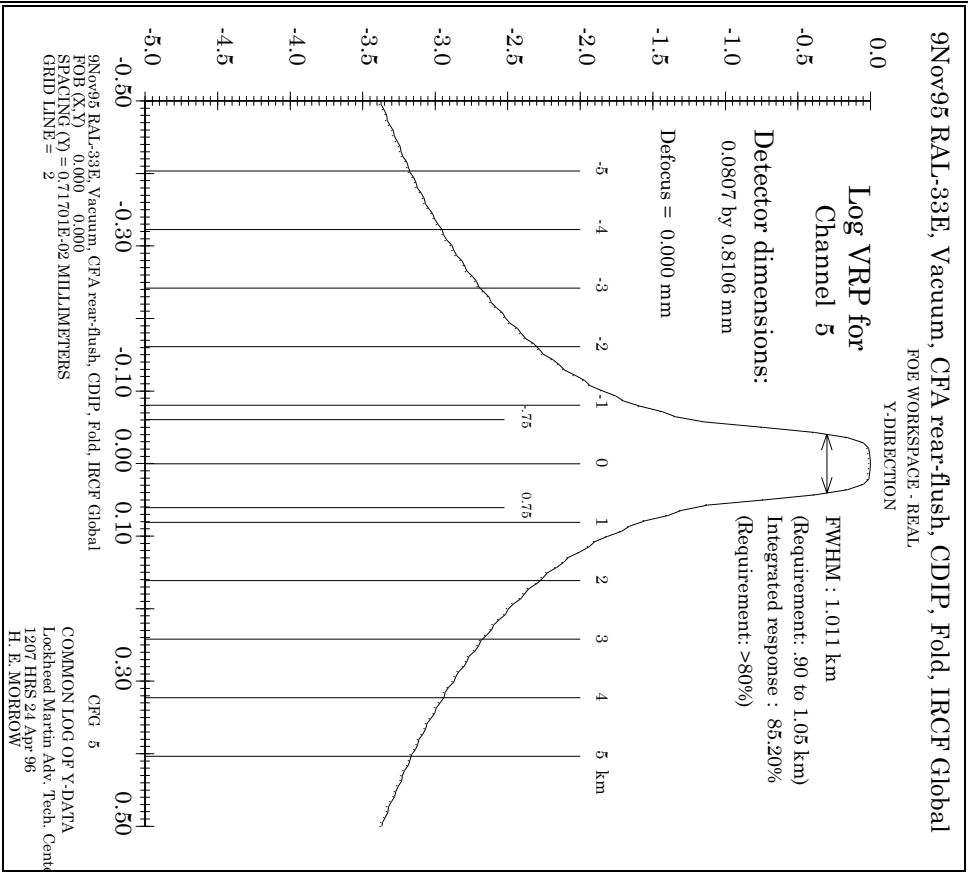
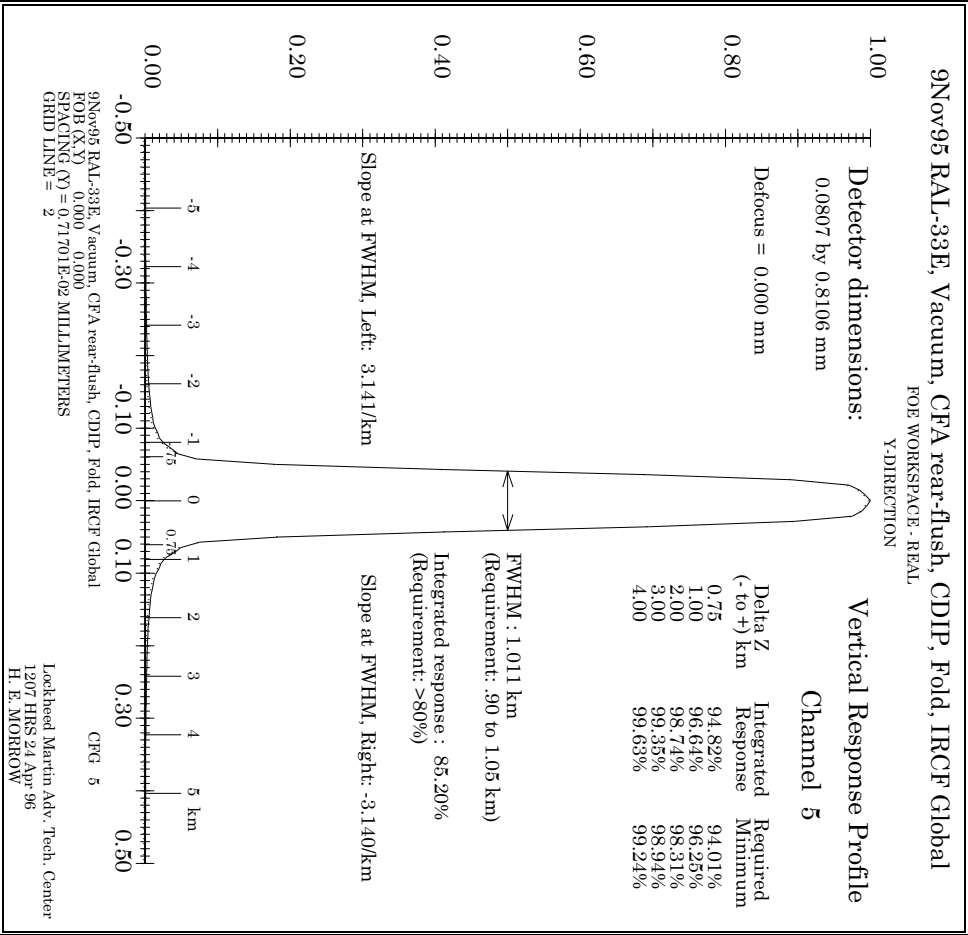
Annotated graphs in both linear and log displays for the selected HIRDLS channels 2, 5, 10, 17, and 21 follow. Following the plots, tables x.x.x and x.x.x summarize the VRP data for all channels.

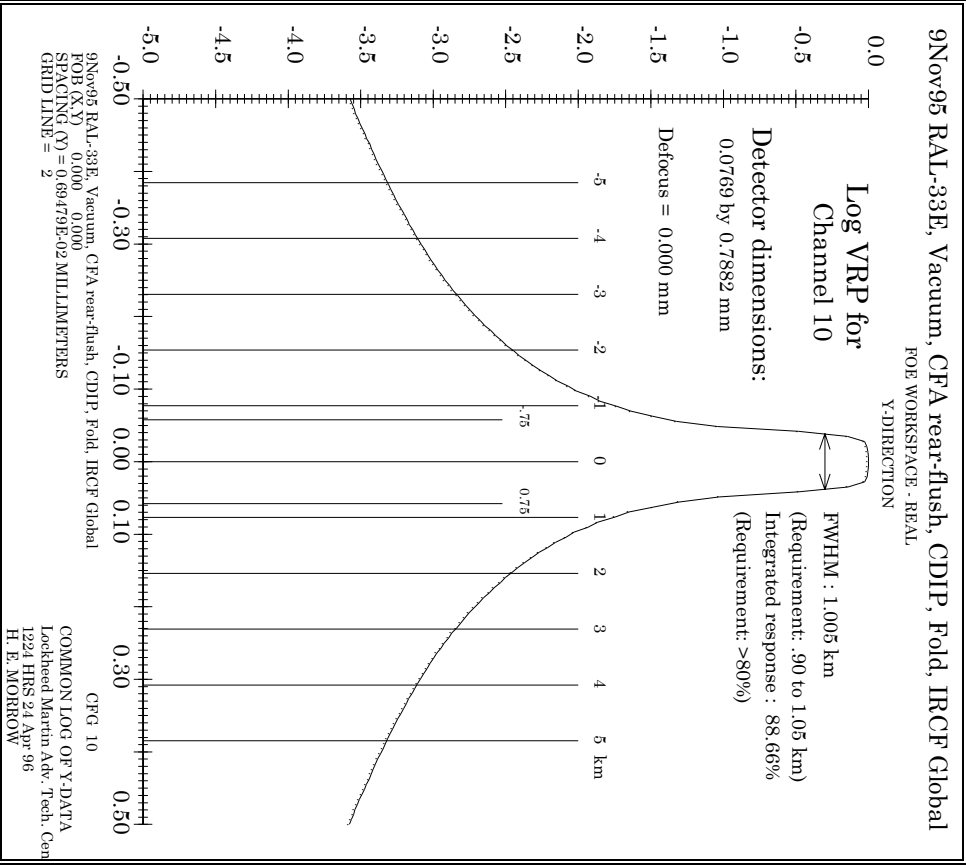
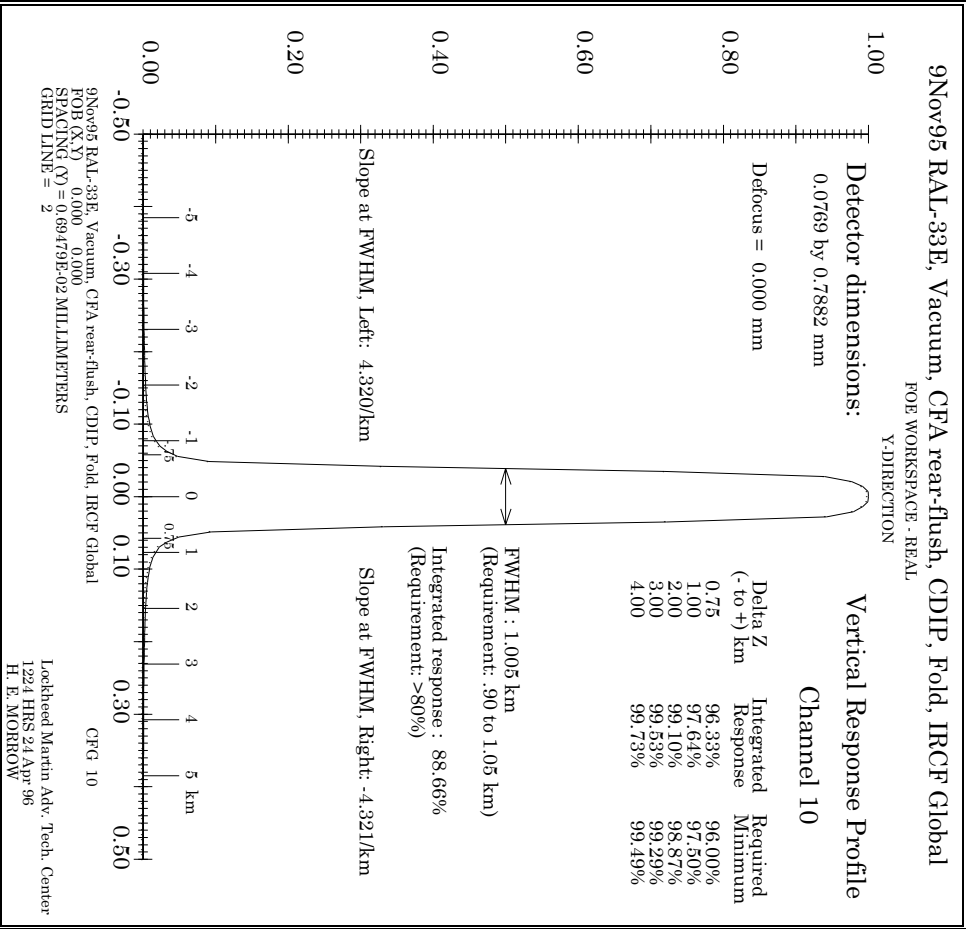
The data was created in OPTIMA with the ideal detector sizes customized for each channel. From 6000 to 18000 rays were traced to develop the wavefront, depending on wavelength. From 16 to 40 airy rings were developed also depending on wavelength. The large ray count is required to produce the large number of diffraction rings (sampling theory). The large number of rings are required to produce diffraction energy out to 5 or 6 or more km from the center.

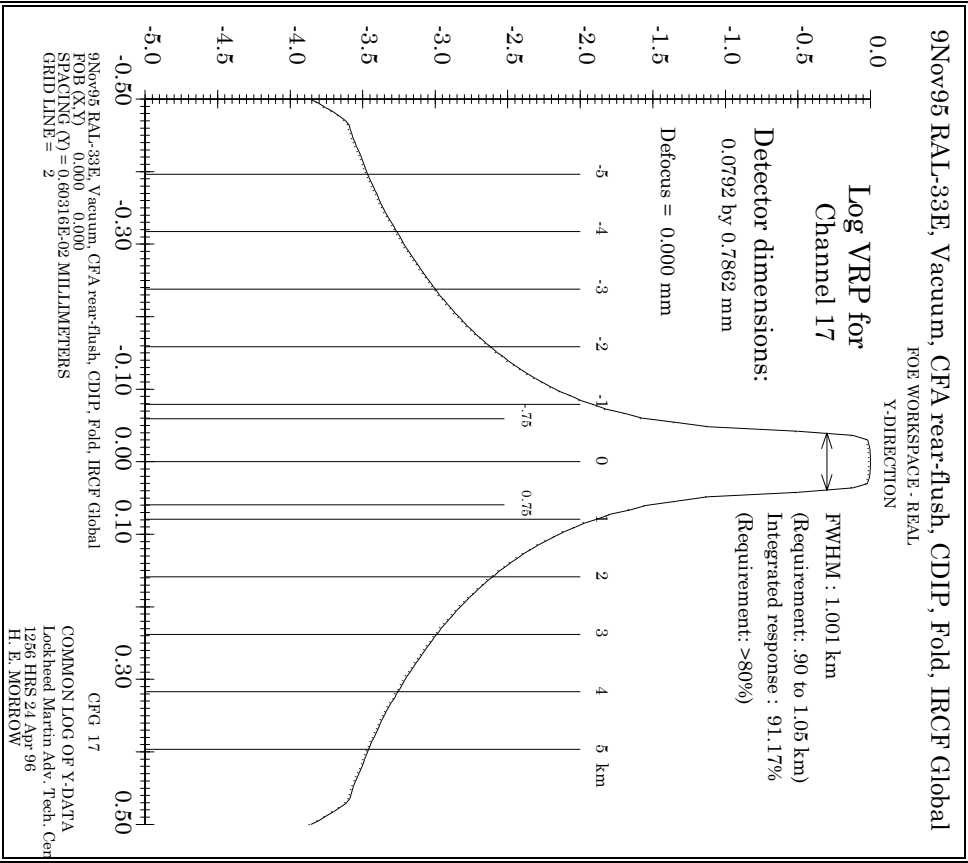
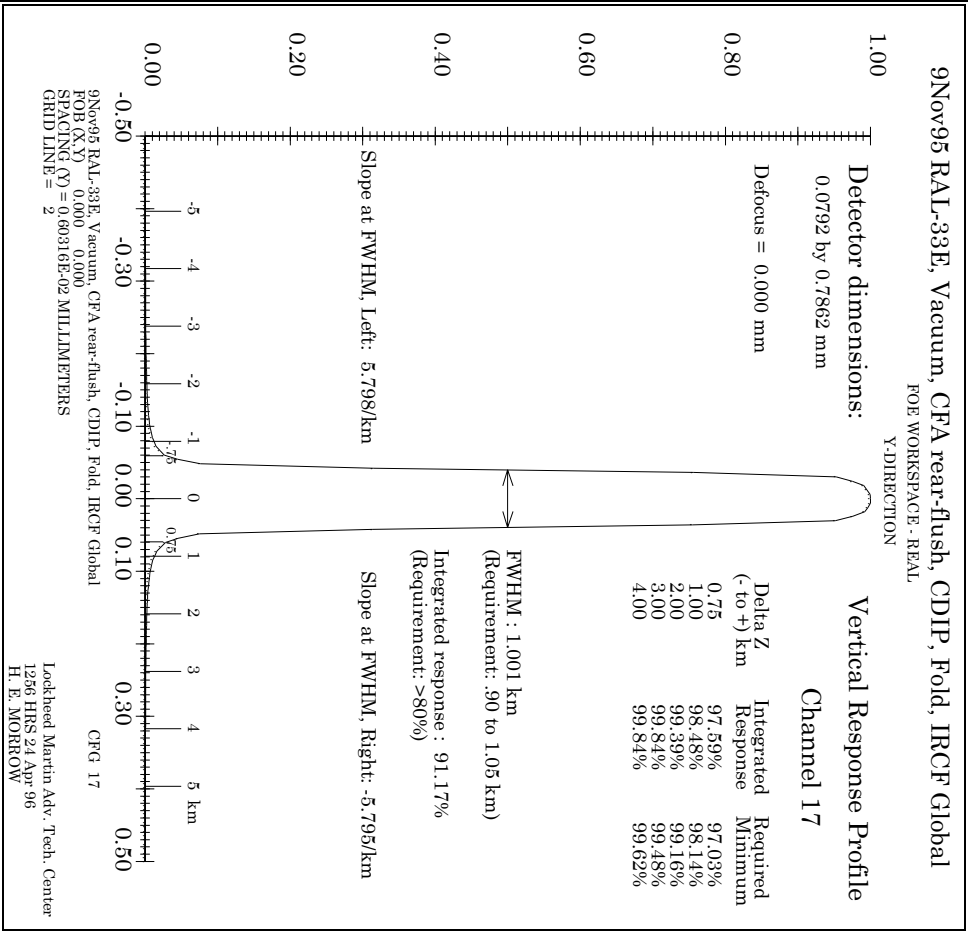
There is one remaining systematic error in the analysis process. The ITS calls for comparison of integrated responses under various limited ranges to the *total integrated response*. The VRP data is “good” over ranges exceeding ± 6 km for long wavelengths, and $\sim \pm 5$ km for the shortest wavelengths. Since the data at these ranges is still asymptotically approaching zero (probably with an inverse cube law), the computed value for the total integrated response is necessarily truncated. The magnitude of the resulting error is unknown at this time. This problem is clearly evident in the log VRP plots below.

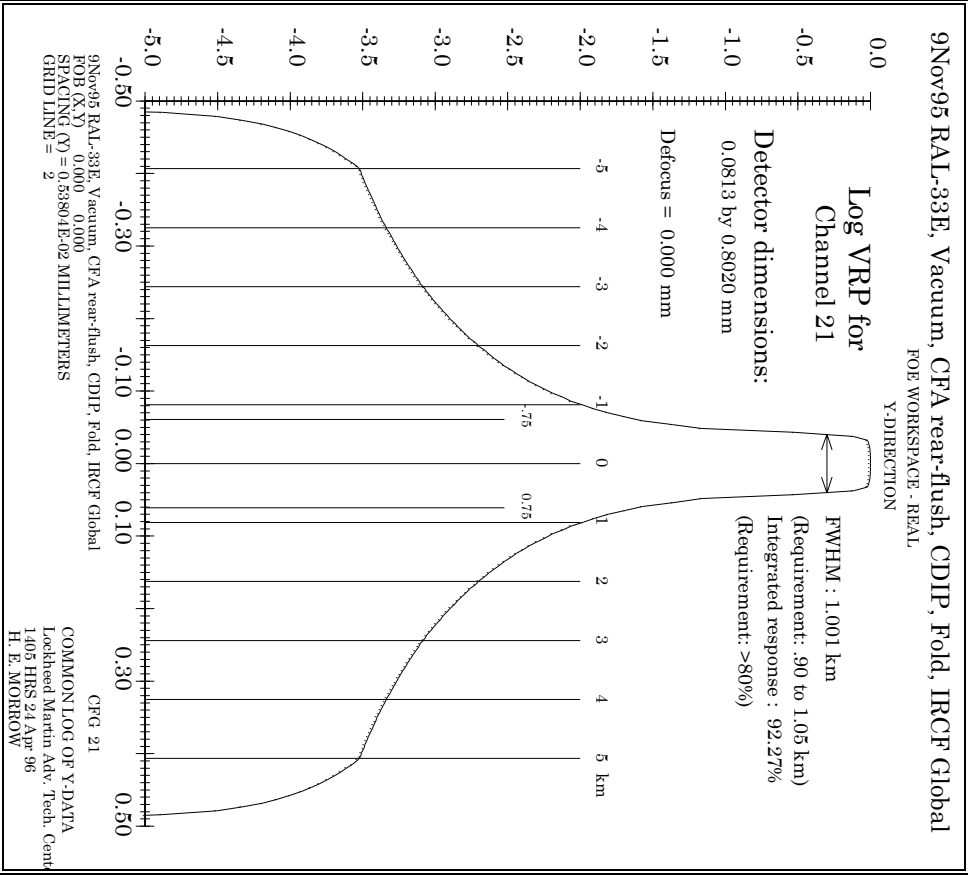
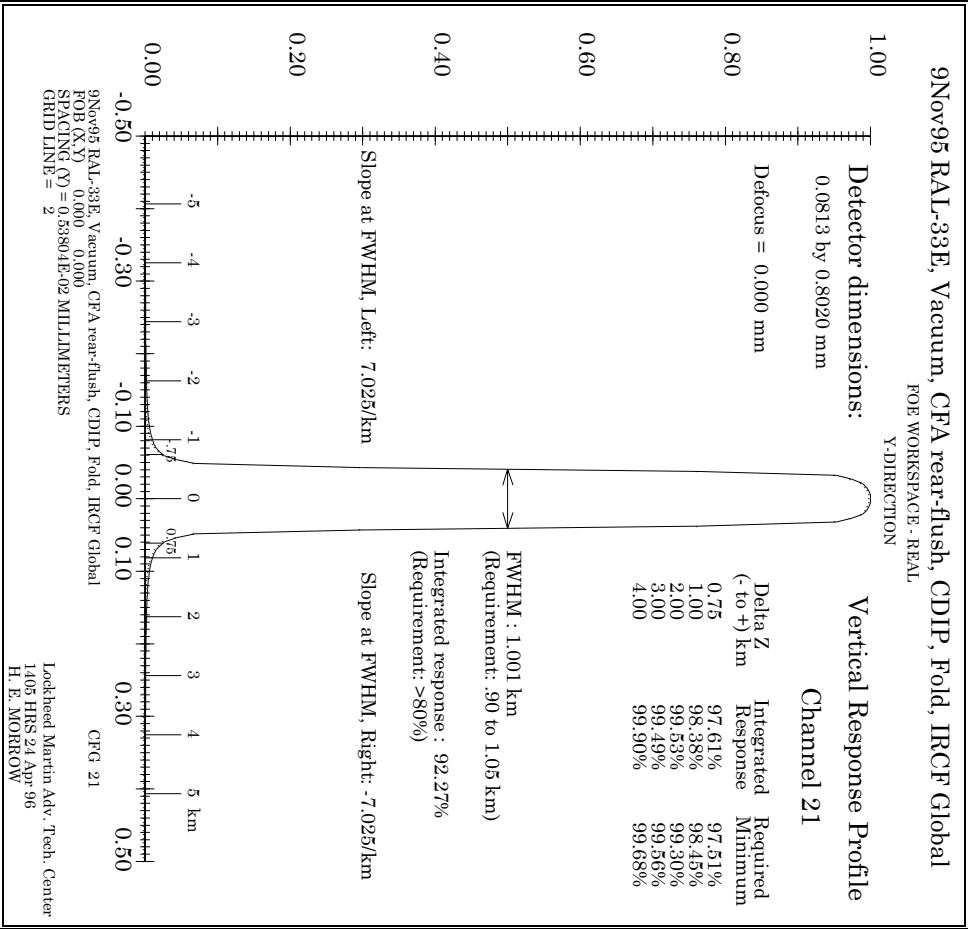
It may be possible to extrapolate the data in the VRP wings with a function like $AY^{-1} + BY^{-3} + CY^{-5}$ and form the integral to infinity. For moderate aberration situations (under defocus or tolerance perturbation), the character of the wings does not significantly change.











The Vertical Response Profile data tables for each channel follow. FWHM is always very near the ideal value because the ideal *geometric* detector size was used. The integrated response under the FWHM exceeds the 80% requirement for the pristine baseline design.

Slope at half max is not an ITS performance requirement. Slope is a useful indicator of performance, is wavelength and aberration sensitive, and may have significant engineering value. It is also easy to measure and to compute.

Table x.x.x FWHM Related Values

Channel Number	FWHM (km)	Integrated Response (%)	Slope (km/mm)
1	1.017	83.86	2.771
2	1.015	84.49	2.795
3	1.013	84.66	2.935
4	1.012	85.08	2.943
5	1.011	85.20	3.141
6	1.006	87.25	3.774
7	1.008	87.34	3.806
8	1.009	87.64	3.849
9	1.006	88.10	4.087
10	1.005	88.66	4.320
11	1.003	88.80	4.247
12	1.007	90.28	4.641
13	1.006	90.76	5.283
14	1.002	90.76	5.550
15	1.002	90.94	5.618
16	1.002	90.88	5.586
17	1.001	91.17	5.798
18	0.999	91.10	5.574
19	1.003	91.70	5.103
20	1.006	92.20	6.032
21	1.001	92.27	7.025

The integrated response in the wings was computed as described above. In the table below, the difference between the computation and the requirement, in percent, is reported.

Note that for channel 21, the margin is slightly negative.

Table x.x.x Integrated Response in Wings - % Margin over requirement.

Channel Number	0.75 km	1.00 km	2.00 km	3.00 km	4.00 km
1	1.11	.55	.58	.55	.53
2	1.14	.54	.54	.51	.49
3	1.05	.50	.50	.48	.46
4	0.96	.51	.52	.49	.47
5	0.81	.39	.42	.41	.40
6	0.56	.27	.34	.33	.32
7	0.45	.20	.28	.28	.28
8	0.33	.13	.25	.26	.26
9	0.39	.18	.26	.27	.27
10	0.33	.14	.23	.24	.24
11	0.42	.21	.26	.26	.25
12	0.49	.23	.27	.26	.25
13	0.50	.23	.27	.25	.24
14	0.50	.26	.26	.26	.24
15	0.57	.32	.27	.31	.24
16	0.56	.31	.27	.31	.24
17	0.56	.33	.23	.36	.22
18	0.36	.26	.29	.29	.22
19	0.42	.23	.25	.24	.23
20	0.42	.22	.24	.10	.10
21	0.10	-.07	.23	-.07	.22

Note that the integrated response within each specified VRP range is found by dividing the area under the range by the total area, so if the total area were increased (by data extrapolation for instance), the integrated response will decrease, *reducing* the margins reported above.

12.5 Through-focus VRP data

Focus shift can be thought of as the lowest order aberration. By developing the VRP data through focus, it is possible to gain considerable insight to the relative sensitivity of the various VRP entities to wavefront error.

This is especially true of Vertical Response Stability (ITS 3.3.3.1). For this case, one may assume that the defocus would occur anytime between the last critical ground calibration of VRP and orbital insertion, and thereafter as thermally induced focus changes in orbit.

12.5.1 Method of computation (in OPTIMA)

For each channel, the VRP data was generated and placed in the center grid of a two-dimensional array. The focus error was introduced into the wavefront without retracing the rays, and the new VRP generated from the defocused diffraction PSF. The defocused VRP data was placed on the array at grid locations corresponding to the amount of focus error. In all, 21 focus positions df were generated over the range $-.100 \leq df \leq +.100$ mm, at 10 micron intervals. The 21 VRP data arrays, 1 for each channel, are saved as permanent files.

A second set of arrays was generated from the VRP data arrays for the purpose of analyzing VRP stability. If the in-focus VRP is defined as the reference (VRPr), and any defocused VRP is an error (VRPe), then the VRP stability function (VRPs) is defined as

$$VRPs = 1 + (VRPr - VRPe)$$

point-by-point along each VRP, where the data intervals are identical by design for all focus values. Taking the difference is valid because all VRP data is normalized to 1.0 at the center. The additive 1 in the expression above is arbitrary, and means that the acceptance range for the VRPs is any value between .995 and 1.005, averaged over any 1/10th km (~8 microns on the focal plane). As a practical matter, the 1/10th averaging range has little impact on the results since the data increment is ~6 microns on the focal plane.

12.5.2 Sample through-focus VRP data plots (Channel 10)

Figure x.x.x below shows the linear plot of VRP vs. focus error for channel 10, while the next figure x.x.x shows the same data plotted in log mode. The plotted data for all channels is superficially identical when viewed visually in either linear or log presentation. A sharp eye will note that the peaks of the VRP data sharpen as defocus is introduced. Otherwise, any deterioration is too subtle to notice visually.

Perhaps this is good news: VRP data entities may therefore be fairly robust against wavefront errors.

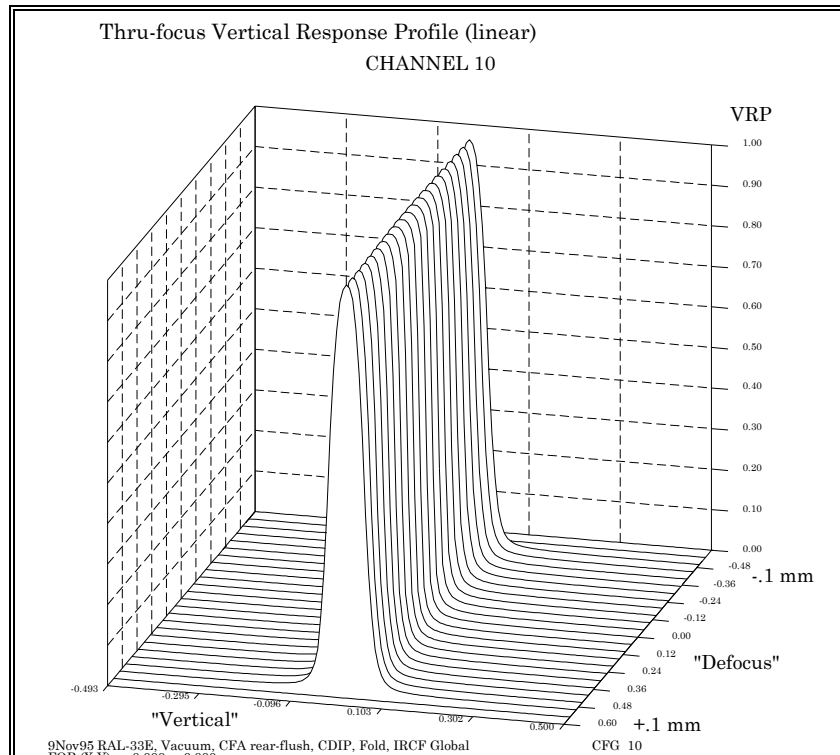


Figure x.x.x The VRP shows little change through focus in a linear display

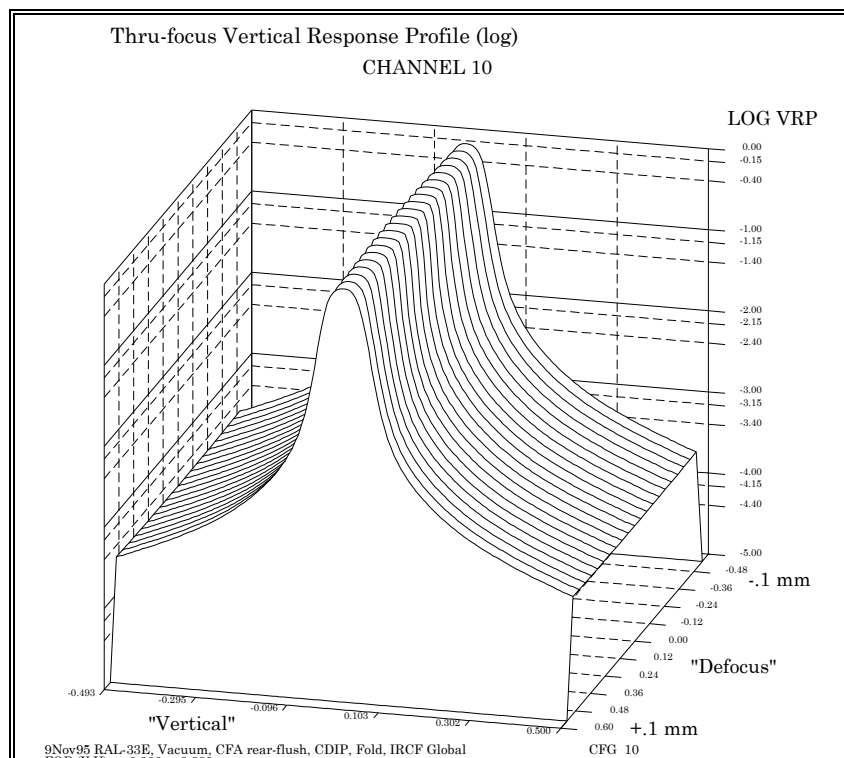


Figure x.x.x The VRP shows nearly no change in the wings, through focus, in a log display

12.5.3 FWHM through focus plots for channels 2, 10 and 21

Full Width Half Max is plotted against focus error for the channels 2, 10, and 21 in figures x.x.x, x.x.x, and x.x.x below. It is interesting to note that FWHM remains in spec over all the focus range, keeping in mind that the detector size used is the ideal geometric dimension for each channel.

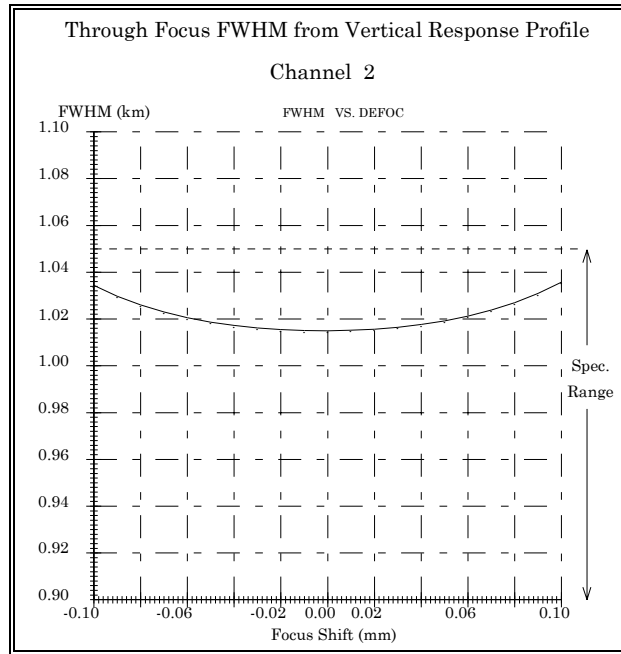


Figure x.x.x FWHM for Channel 2 stays in spec over ± 100 micron defocus range

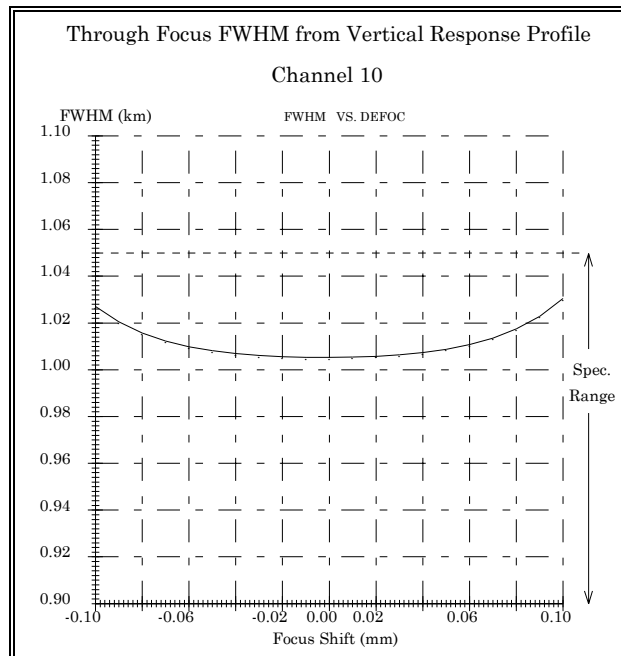


Figure x.x.x FWHM for Channel 10 stays in spec over ± 100 micron defocus range

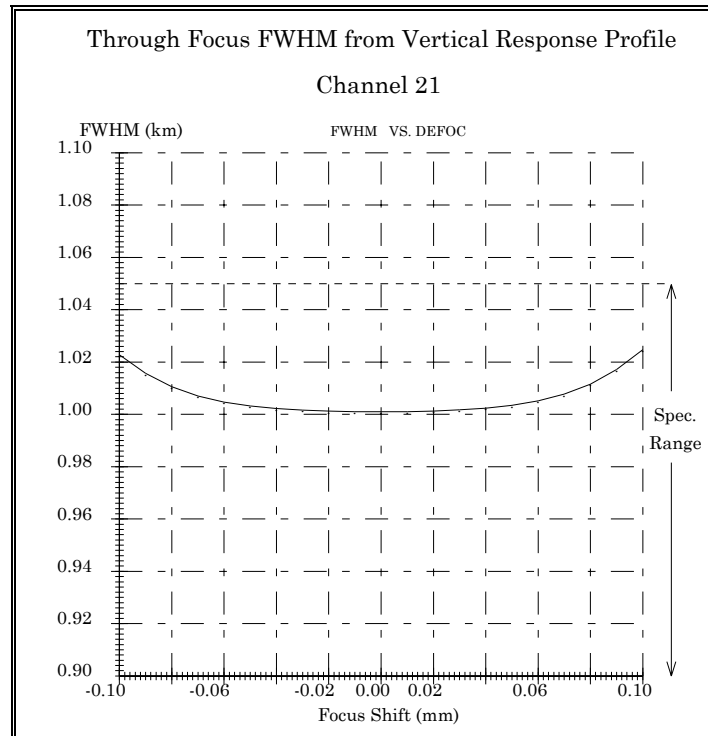


Figure x.x.x FWHM for Channel 21 stays in spec over ± 100 micron defocus range

12.5.4 Slope at FWHM through focus for channels 2, 10 and 21

This slope is not an ITS specification. However it is shown anyway because it is a useful engineering measurement and is easily obtained from either computational data or measured data, and may serve as a diagnostic tool.

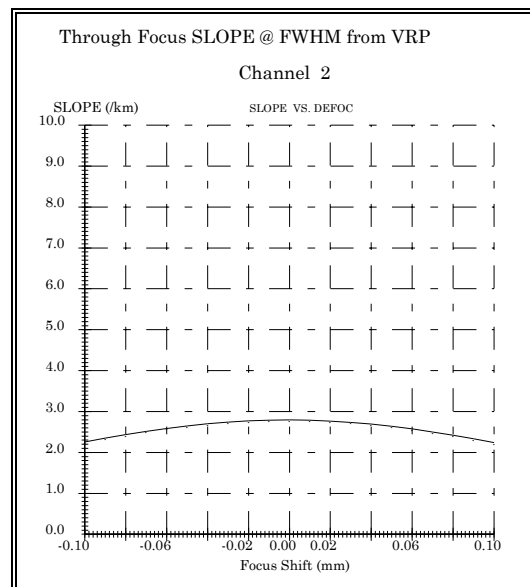
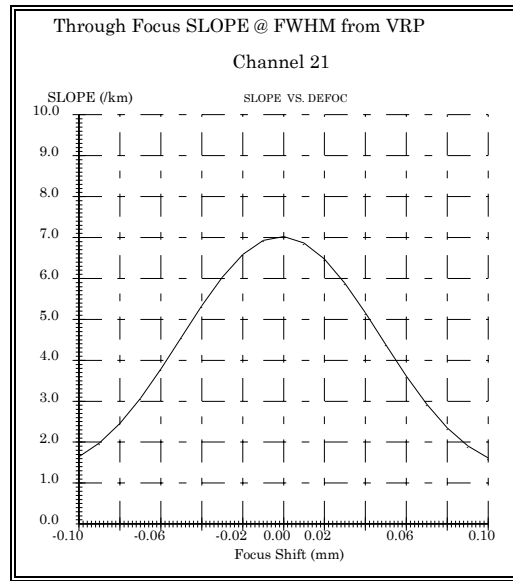
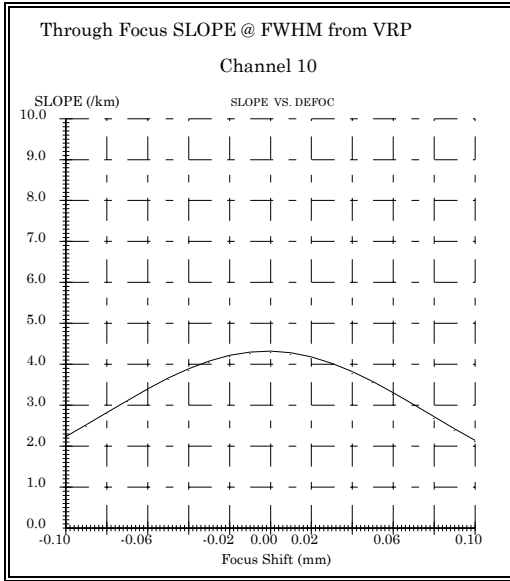


Figure x.x.x Slope at FWHM for channel 2 decreases modestly over the focus range



Figures x.x.x & x.x.x Slope at FWHM through focus changes significantly and dramatically for channels 10 and 21 respectively

12.5.5 Relative integrated response under FWHM through focus for Ch. 2, 10 and 21

The ITS requires that at least 80% of the total integrated response under the VRP lie within the FWHM. The three figures x.x.x through x.x.x below show that this requirement is met even through the ± 100 micron focal shift examined.

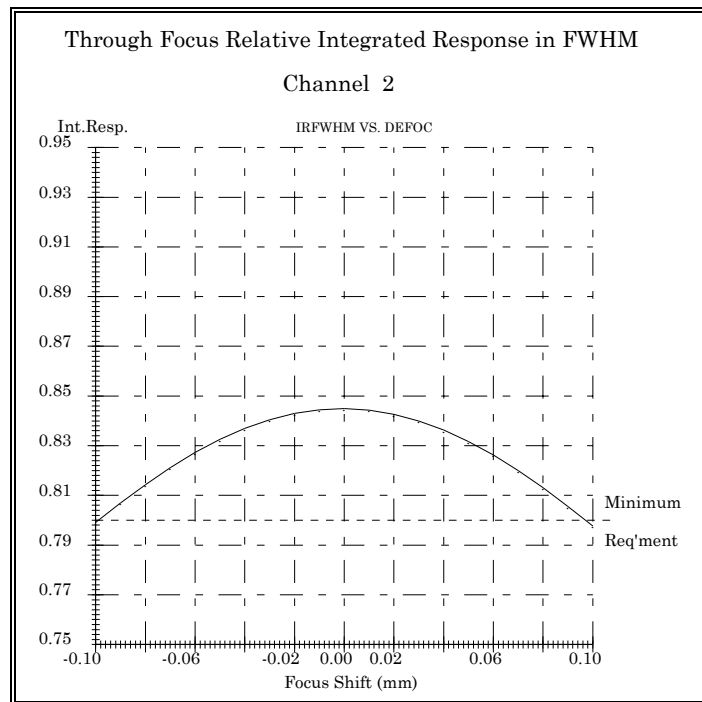


Figure x.x.x Relative integrated response under FWHM is in spec for ± 100 micron focal range for Channel 2.

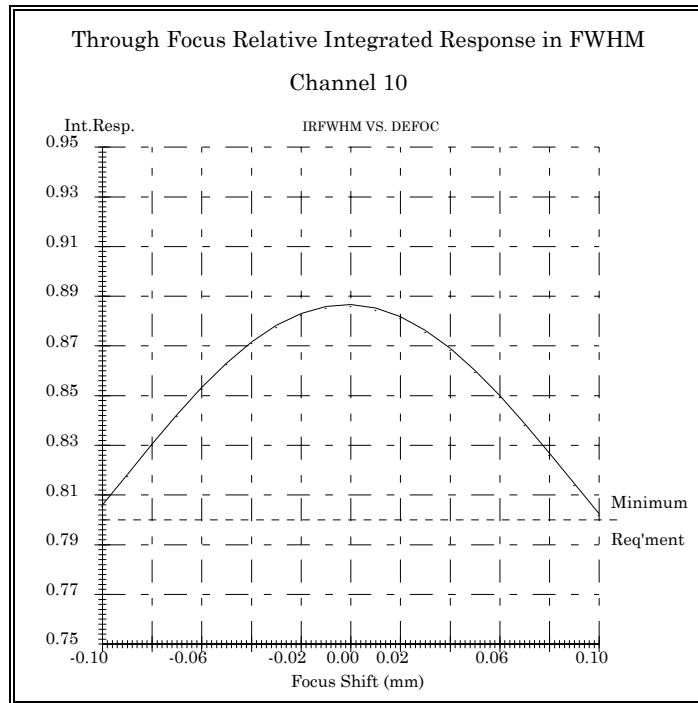


Figure x.x.x Relative integrated response under FWHM is in spec for ± 100 micron focal range for Channel 10.

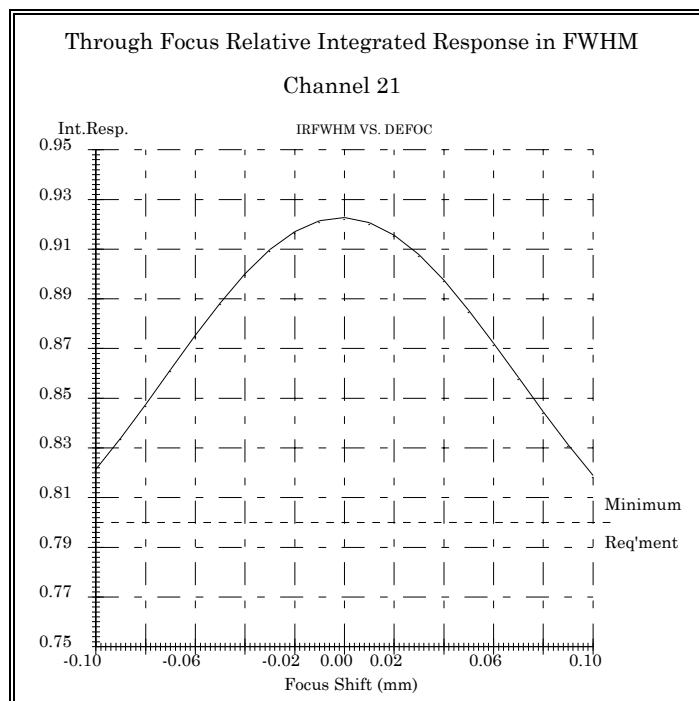


Figure x.x.x Relative integrated response under FWHM is in spec for ± 100 micron focal range for Channel 21.

12.5.6 Relative integrated response through focus within $\pm .75$ km for Ch 2, 10, & 21

The in-focus margin is less for shorter wavelengths for the relative integrated response within $\pm .75$ km. The focus error tolerated decreases as the wavelength gets shorter.

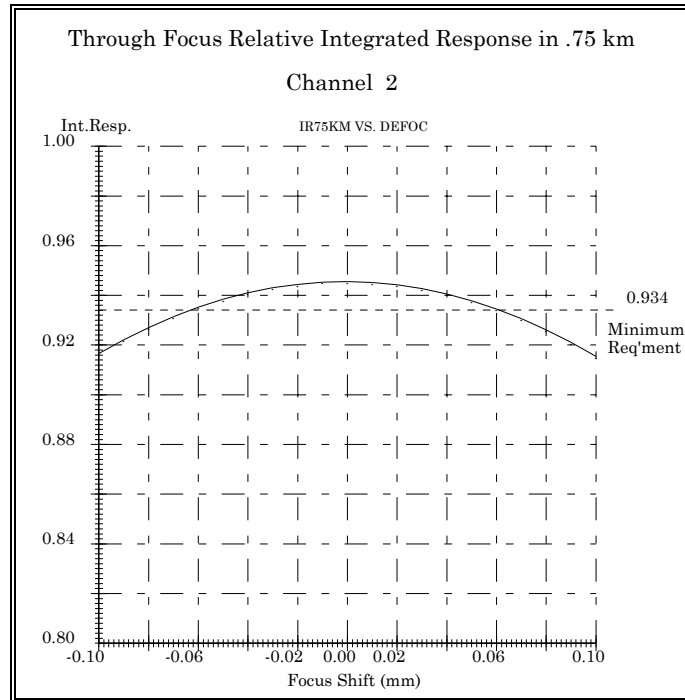
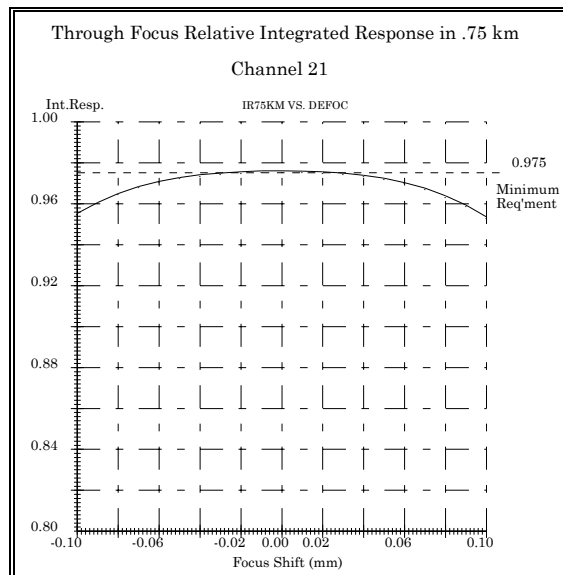
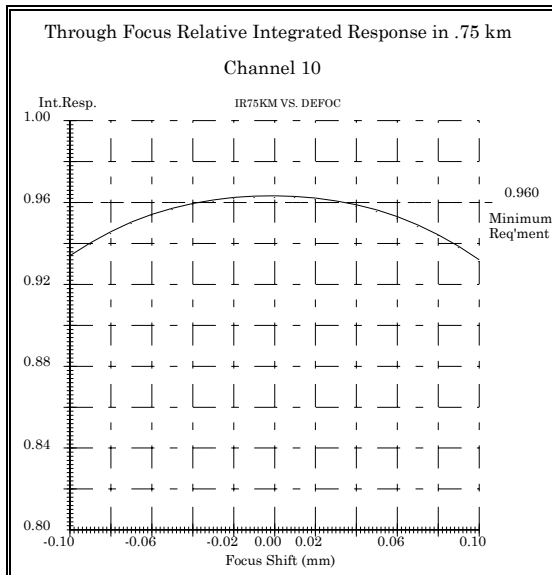


Figure x.x.x Integrated response for Channel 2 over the $\pm .75$ km height remains in spec over ± 60 microns of focus shift.



Figures x.x.x & x.x.x Integrated response for both Channels 10 & 21 over the $\pm .75$ km height remains in spec over ± 30 microns of focus shift.

12.5.7 Relative integrated response through focus within ± 1.0 km for Ch 2, 10, & 21

For the relative integrated response within ± 1.0 km, the focus error curve is flatter than at 0.75 km. This flattening trend becomes more pronounced as the integration is carried to greater heights, and is the reason that no through focus data is presented for 2-4 km.

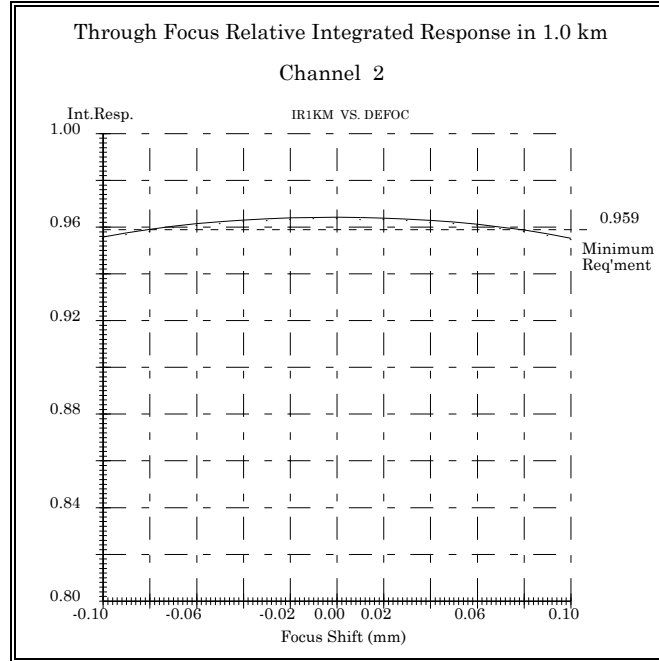
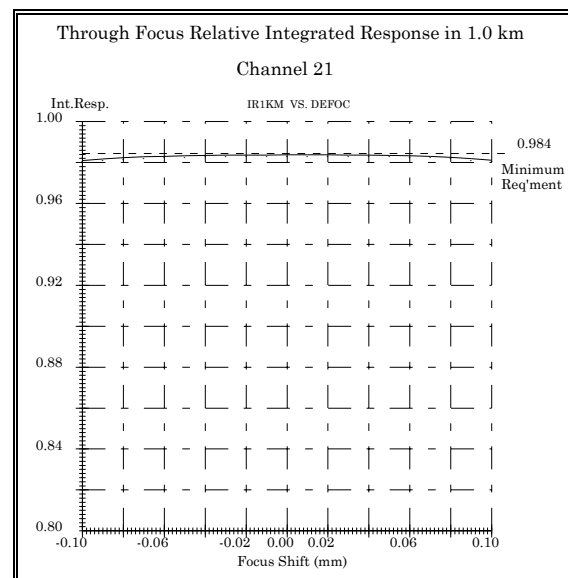
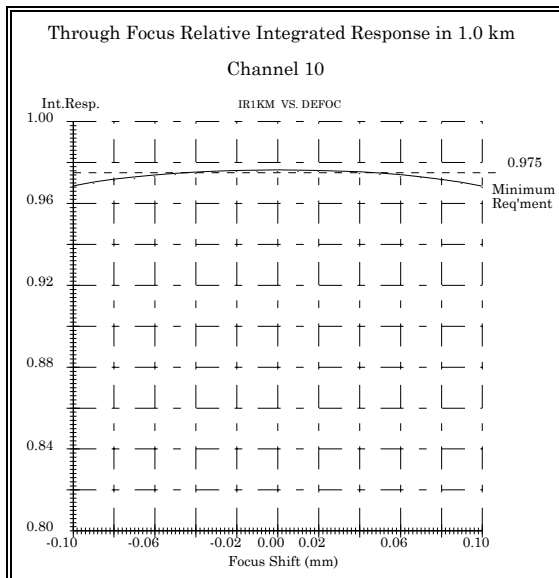


Figure x.x.x Integrated response for Channel 2 over the ± 1.0 km height remains in spec over ± 80 microns of focus shift.



Figures x.x.x & x.x.x Over the ± 1.0 km height, integrated response for Ch. 10 remains in spec over ± 50 microns of focus shift. Ch 21 is just out of spec.

12.5.8 Relative integrated response through focus for heights ≥ 2.0 km.

The through-focus relative integrated responses for heights 2.0 km and larger are so flat (independent of focus shift) that no graphics examples will be shown. The margins in paragraph 12.4.2 (table x.x.x) are essentially the same over focus from -100 to +100 microns.

12.5.9 Tabulated through-focus VRP data for all channels.

Table x.x.x Through focus VRP data for all channels

Channel number	Average FWHM at 100 microns defocus (km)	Average integrated response at 100 microns defocus	.75 km integrated response focus spec limit (~microns)	1.0 km integrated response focus spec limit (~microns)
1	1.039	.7945	± 60	± 80
2	1.035	.7984	± 60	± 80
3	1.033	.7986	± 60	± 80
4	1.032	.8003	+ 55 - 60	± 80
5	1.031	.7977	+ 50 - 54	± 70
6	1.027	.8059	± 55	+ 65 - 62
7	1.030	.8050	± 40	± 55
8	1.033	.8025	+ 30 - 35	± 40
9	1.030	.8054	± 40	+ 55 - 50
10	1.029	.8043	+ 35 - 40	± 45
11	1.026	.8086	± 53	± 60
12	1.026	.8154	+ 45 - 50	+ 65 - 70
13	1.025	.8165	± 50	± 70
14	1.023	.8173	+ 50 - 55	± 75
15	1.024	.8178	± 55	+ 85 - 80
16	1.024	.8166	+ 53 - 58	± 80
17	1.026	.8136	± 52	± 80
18	1.026	.8140	± 52	+ 75 - 70
19	1.024	.8177	± 58	± 74
20	1.023	.8191	± 50	± 75
21	1.024	.8201	± 30	0

In the table above, column 2 reports the average of the two FWHM values at +100 and -100 microns focus shift. This value is “in spec” even at the full 100 micron focus error, and it appears that FWHM growth due to aberration will not be an optical tolerance

driver. The largest portion of FWHM tolerance budget can go to uncertainty in the “vertical” sizes of the detectors during fabrication.

Column 3 in the table above reports the average of the two values of integrated response under the FWHM fraction of the ± 100 microns defocused VRPs. This value also stays “in spec” over the trial defocus range, although the value for channel 1 is just over the limit. Note that these values will be reduced slightly if a correction factor to the total response were applied, resulting possibly in several more channels being out of spec.

Columns 4 and 5 in the table above report the focus range over which the relative integrated response within $\pm .75$ km and ± 1.0 km respectively stays within the permitted minimums. The permitted focus ranges vary from ± 80 microns to about ± 35 microns *assuming a waiver for channel 21*. Note that these focus ranges will be reduced somewhat if a correction factor to the total response were applied.

Data has been collected and saved (but is not reported here) for the through-focus relative integrated response within ± 2 , ± 3 , & ± 4 kms. Curiously, the effect of this amount of defocus on this parameter is (nearly) negligible, and probably indicates that this parameter will not be a driver for the tolerance budget.

12.6 VRP stability (ITS 3.3.3.1)

The method of computation is described in section 12.5.1.

This section will display plots of several typical difference-data files, and also plots of minimum and maximum peak values for selected channels. Finally a focus-tolerance table for all channels will be given.

12.6.1 Selected VRP stability “difference data” plots.

Figures x.x.x and x.x.x below each show *half* of the data in each array generated by the method outlined in 12.5.1. Since the full plots are very symmetric with respect to defocus (and quite symmetric with respect to elevation also), only the 0 to 100 micron defocus portion is shown. A better view is thus afforded, since the more turbulent results are all in the rear of the plot at 100 microns defocus.

The gross morphology of these plots can be quite easily understood given the familiarity we now have from section 12.5. As focus error is introduced, the FWHM stays fairly stable, but the slope of the VRP does change, more strongly as wavelength decreases. The far wings have good stability through focus. Therefore, if the data of the defocused profile (VRPe) is subtracted from the in-focus profile (VRPr), the result is zero in the center due to normalization, but just inside the FWHM points the result is positive. At some point near the FWHM, the result is zero again, and then outside the FWHM, the difference is negative. Finally in the far wings, the difference is nearly zero, partly because the values are small, and partly because the data is stable anyway.

In the two plots which follow, the nearest line is flat, representing perfect stability of the VRPr with itself. Recall that 1.00 is added to the differences resulting in a unit bias in the data.

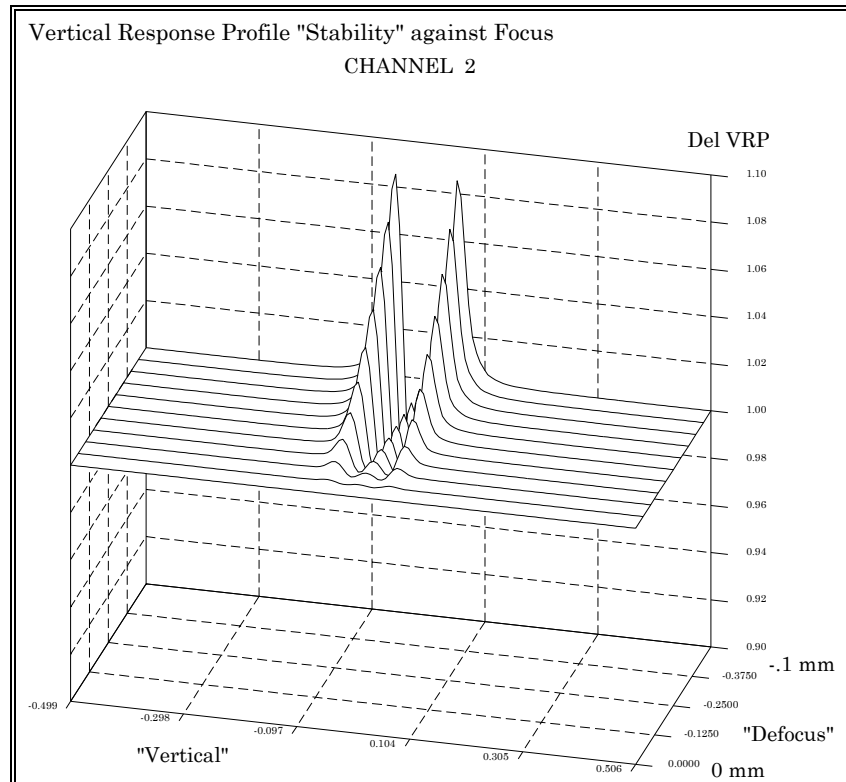


Figure x.x.x Half of the difference-data VRP array for channel 2

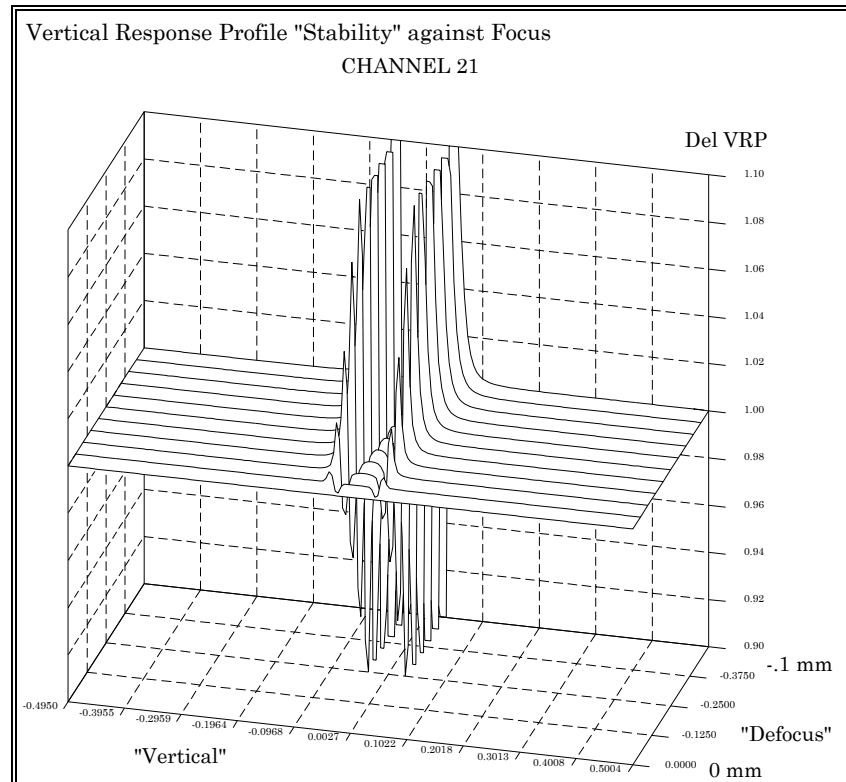


Figure x.x.x Half of the difference-data VRP array for channel 21

In the presentation of the above plots, the vertical (1+difference) dimension was clipped above 1.10 and below .90. While all the data for channel 2 fits in this range, the data for channel 21 does not resulting in clipped data. The ITS specification requires that VRP be stable, in this formulation, such that the data lie between .995 and 1.005 - a quite small portion of the vertical dimension displayed.

12.6.2 VRP stability: peak and valley projections.

A routine was invoked on the difference data arrays which could select the local peak and valley values through focus in the difference data. If these values are then plotted through focus, the acceptable focus range for VRP stability can be read off the graph.

Figures x.x.x through x.x.x below present such plots for channels 2, 10, and 21. Since there are two peaks and two valleys for each VPRE, there are 4 curves on each plot in nearly coincident pairs.

Note the evident quadratic dependence with defocus. This implies that exceeding the focus range limit will result in runaway excessive VRP instability.

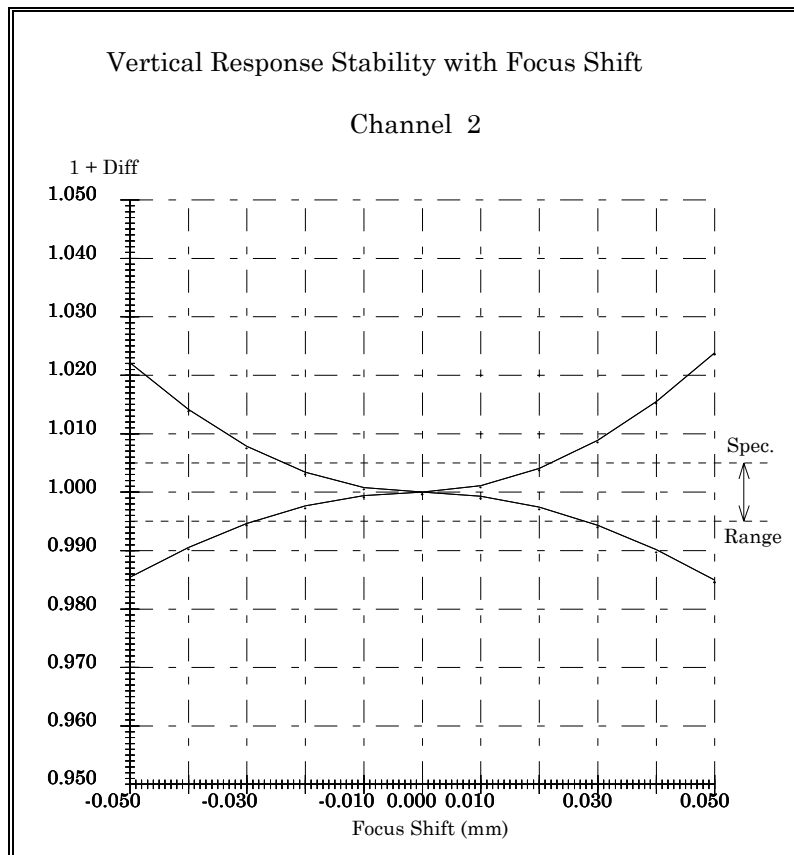


Figure x.x.x VRP stability for channel 2 is acceptable within ± 23 microns defocus.

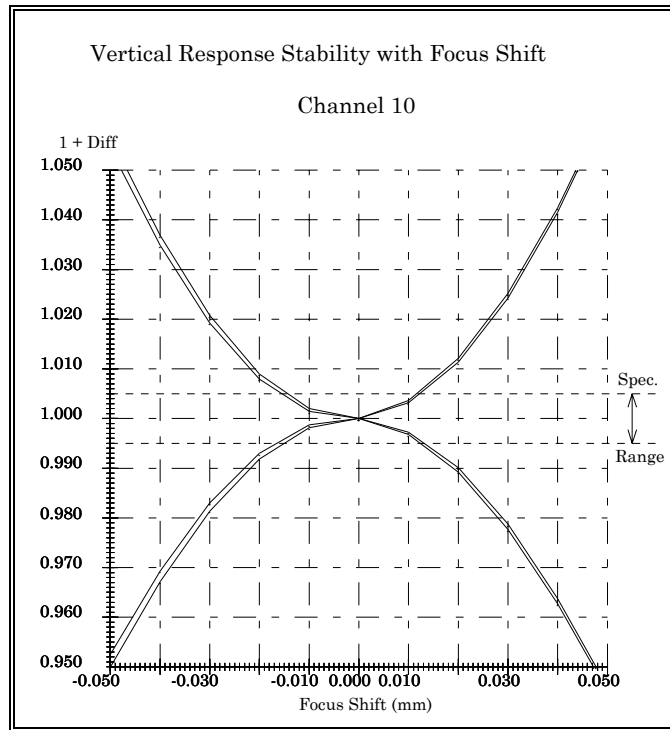


Figure x.x.x VRP stability for channel 10 is acceptable within ± 13 microns defocus.

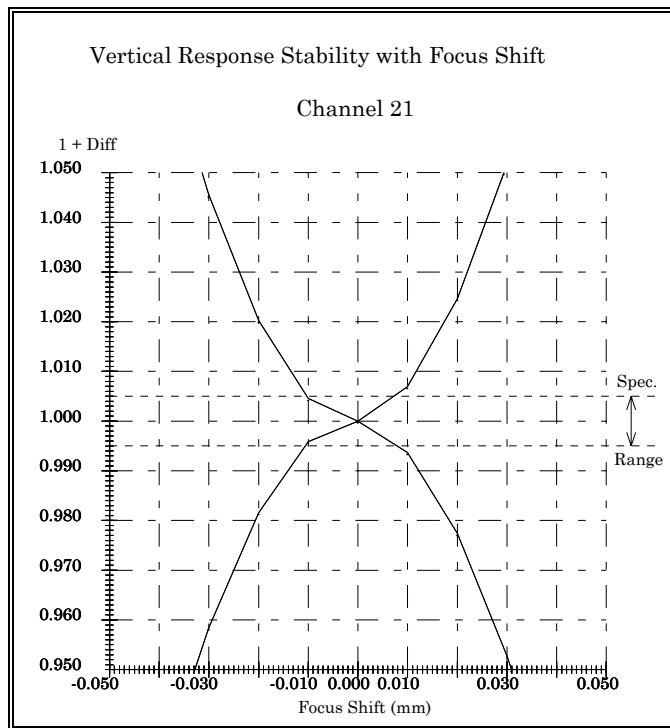


Figure x.x.x VRP stability for channel 21 is acceptable within ± 9 microns defocus.

12.6.3 VRP stability focus range for all channels

In the table x.x.x which follows, the focus range within which VRP stability is acceptable is presented for all 21 channels. The data was picked off plots like those in the preceding section.

Table x.x.x Focus range for acceptable VRP stability for all channels

Channel number	Focus range (microns)
1	+ 22 - 25
2	+ 22 - 24
3	+ 21 - 23
4	+ 20 - 23
5	+ 18 - 22
6	+ 16 - 17
7	+ 15 - 17
8	+ 13 - 17
9	+ 13 - 15
10	+ 12 - 14
11	+ 13 - 13
12	+ 12 - 14
13	+ 12 - 12
14	+ 11 - 12
15	+ 11 - 11
16	+ 10 - 12
17	+ 8 - 11
18	+ 8 - 10
19	+ 7 - 11
20	+ 7 - 11
21	+ 7 - 11

It should be clear that this type of focus error (after ground calibration, launch, to EOL) is global to all channels. Only one focus error or drift value can be allocated: a reasonable value would be ± 10 microns.

13.0 Thermally induced focus error

The HIRDLS imager optics can be considered in two sections. The first section, which is the Gregorian off-axis telescope up to FS2, will be athermal if constructed entirely of aluminum. That is, under an isothermal temperature change of the first section *only*, the spaces as well as the element powers change the same amount because the thermal coefficient of expansion (CTE) is the same everywhere. Therefore the beam at FS2 (and the detector) remains in focus. If the elements and spaces are at *different* temperatures however, the beam may not remain in focus at FS2, and therefore may not be in focus at the detector. This case is considered in section 13.1

The second section is the relay section from FS2 to the detector, and is not athermal if the metering is aluminum, because the germanium lenses are very sensitive to temperature. This section is considered in section 13.2 where the requirement for temperature stabilization of the lenses is clarified.

13.1 Telescope elements

There are only 4 prescription parameters in the telescope which can contribute to thermally induced focus error. These are the primary and secondary mirrors, and the two metering spaces, primary to secondary, and secondary to FS2.

For the analyses which follow, the CTE for aluminum is assumed to be $23 \times 10^{-6}/^{\circ}\text{C}$. All focus shifts reported are at the detector. Furthermore, the defocus effects will be taken for channel 10 as representative of all channels.

13.1.1 Primary and secondary mirrors

The radii of curvatures are changed by $\delta R = \text{CTE} \cdot \delta T$, and the focus shift determined by raytrace. The results obtained are summarized in table x.x.x below. The radii were simply changed at the vertex; no special consideration was made for the fact that both mirrors will be mounted at their mechanical centers, off-axis from their vertices.

In all the tables in this section, the center column is the focus shift at the detector for 1 degree C temperature rise of the entity in the left column. The right column is an inverse sensitivity, and gives the temperature change required to produce a 10 micron focal shift. This is the focus stability tolerance suggested in 12.6.3 of this document.

Table x.x.x Focus error due to temperature changes in telescope mirrors

Element	$\delta\text{-focus}/^{\circ}\text{C}$ (microns)	$\delta\text{-}^{\circ}\text{C}$ for 10 microns $\delta\text{-focus}$
Primary	2.26	4.43 $^{\circ}$
Secondary	0.947	10.55 $^{\circ}$

13.1.2 Two spaces

If the spacing between the primary and secondary, or secondary and FS2 are changed by $\delta l = \text{CTE} \cdot \delta T$, and the focus shift determined by raytrace, the results obtained are summarized in table x.x.x below.

Table x.x.x Focus error due to temperature changes in telescope spacing

Space	$\delta\text{-focus/C}$ (microns)	$\delta\text{-C}$ for 10 microns $\delta\text{-focus}$
Pri - Sec	-2.94	3.40°
Sec - FS2	-.271	36.9°

13.2 Relay section

Only the 2 lenses and the 3 spaces in the relay section can independently change the focus if they are thermally perturbed. The vacuum window can have a small effect, but both the CTE and dn/dT for ZnSe are mild, and not analyzed at this time. For the analyses which follow, the CTE for the spaces is assumed to be $23 \times 10^{-6}/\text{C}$, including the space between L2 and the detector (but see 13.3.3). The CTE for the Germanium lenses is small, only $5.53 \times 10^{-6}/\text{C}$, but it is applied nevertheless. The problem with germanium is dn/dT which has a very large value of $400 \times 10^{-6}/\text{C}$.

13.2.1 Germanium elements

The germanium lenses have dramatically different thermal sensitivities of more than 20:1, much greater than their focal length ratio of 4.7:1. This is seen in table x.x.x below which shows that L2 must be thermally controlled (better than 1 degree) while thermal control of L1 may not be required.

Table x.x.x Focus error due to temperature changes in the germanium lenses

Element	$\delta\text{-focus/C}$ (microns)	$\delta\text{-C}$ for 10 microns $\delta\text{-focus}$
L1	-.205	48.78°
L2	-4.57	2.18°

13.2.2 Three spaces

The three metering spaces in the relay were independently expanded by the aluminum CTE of $23 \times 10^{-6}/\text{C}$ with the results summarized in table x.x.x below.

Table x.x.x Focus error due to temperature changes in relay spacings

Space	δ -focus/C (microns)	δ -C for 10 microns δ -focus
FS2 - L1	-.061	163°
L1 - L2	-.014	714°
L2 - Det.	-.71	14°

13.3.3 Special problem of the dewar assembly (L2 to detector)

The space between the last lens L2 and the detector is not simply metered by aluminum at room temperature. An equivalent CTE for this space must be constructed from the design, materials, and CTE's of these materials (at their operational temperatures). As the dewar design does not yet exist in sufficient detail, the required equivalent CTE is not yet known.

13.3 Full system with thermally stabilized lenses

If the germanium lenses were thermally controlled without error, the rest of the system could change temperature and cause a focus error. Assuming all aluminum, table x.x.x below gives this result.

Table x.x.x Focus error due to temperature changes in the aluminum parts

Segment	δ -focus/C (microns)	δ -C for 10 microns δ -focus
All aluminum parts	-.807	12.4°

14.0 Element Null test Configurations (nulltest.doc)

There are four aspheric surfaces in the imager. In addition there is one in the IFC and one (toric) in the space view. Each of these surfaces will require special consideration when testing for optical surface figure. The sections which follow review the acceptance test configuration and ideal performance for each surface.

Some surfaces are treated only briefly, and no mention is made of tolerances.

14.1 Null testing

In an optical null test, the configuration of the test setup, in its ideal implementation, will produce an optical wavefront sensibly free of any aberration. The interferogram resulting from such a configuration should produce no fringes, or, if tilt is introduced correctly, fringes should be straight, parallel, and equally spaced (all three conditions simultaneously).

14.2 Off-axis parabolas: the imager primary, and the IFC mirror

This case is so well known that no graphic will be presented. A plane wave incident on the mirror and parallel to the vertex axis will produce a stigmatic (aberration-free) image at the focus.

Alternatively, a point source at the focus will be collimated into a stigmatic plane wave. There are numerous test configurations which exploit this property.

14.3 The secondary mirror

The secondary mirror is an off-axis ellipsoid characterized by a conjugate pair of real foci as in any closed ellipse. A null test is achieved by placing a point source at one focus and observing the quality of the image at the other focus which is theoretically stigmatic.

A retro-sphere placed with its center of curvature at the image will return the wavefront to the source for examination. Wavefront errors due to surface defects are doubled in this case.

In the HIRDLS imager, the secondary is actually operated at its null foci. That is, a point in the center of FS1 is imaged stigmatically into the center of FS2. Figure x.x.x in section 4.5.2 of this document shows a suitable picture of the secondary and its foci.

14.4 Germanium lens 1

While the vendor may wish to test the individual surfaces on this lens, the acceptance test must be done in transmission. Raytrace exploration for this lens in isolation shows that there is no pair of conjugate images which come close to low aberration. Therefore an auxiliary lens has been designed which corrects the aberration of L1 in transmission.

The layout has been optimized for use at $\lambda = 3.39$ microns for several reasons. The source is a HeNe laser with a very well behaved single transverse mode beam. The laser is readily available at low cost. This wavelength permits the use of low cost high quality

materials for the null corrector lens - in this case, IR grade fused silica. Finally, as the wavelength is shorter than the shortest HIRDLS wavelength, there is adequate sensitivity for wavefront measurement. The lens should be accepted for wavefront quality *before* the anti-reflection coating is applied as the coating at 3.39 microns may have quite high reflectivity.

In the layout for this test shown in figure x.x.x below, Ge L1 is on the left.

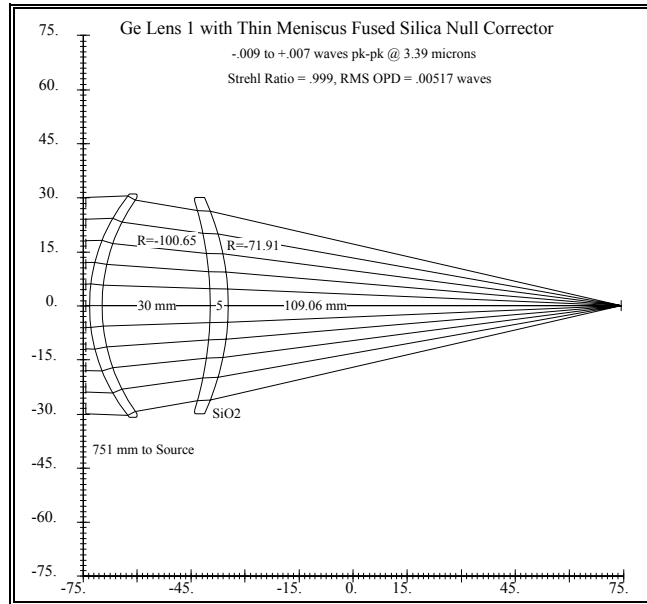


Figure x.x.x A single element of fused silica with L1 will produce an excellent wavefront null.

Figure x.x.x below shows the highly corrected wavefront produce by the null test for L1.

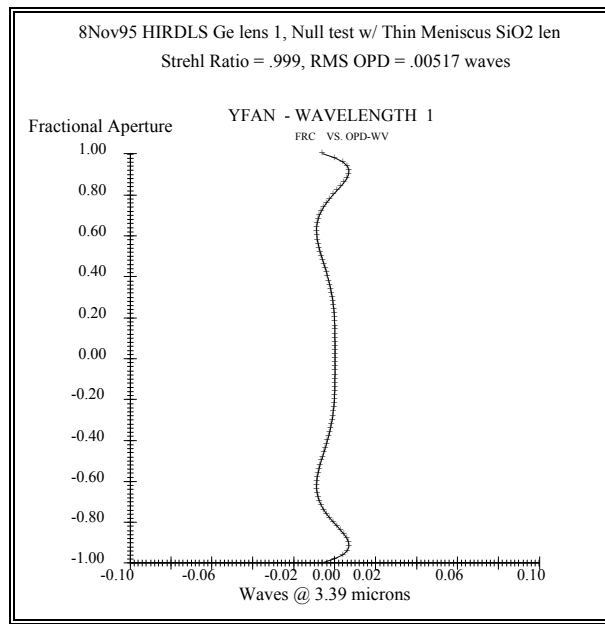


Figure x.x.x A Strehl ratio of .999 at 3.39 microns is produced in the L1 null test.

14.5 Germanium lens 2

Similar to L1, L2 in isolation has no low aberration conjugate. In addition, because it is a more aggressive lens (shorter focal length and oversized aperture), a singlet auxiliary lens could not be found which gives a high quality null test.

Figure x.x.x below shows a doublet null lens with L2 in the null configuration. The material is IR grade fused silica with spherical surfaces.

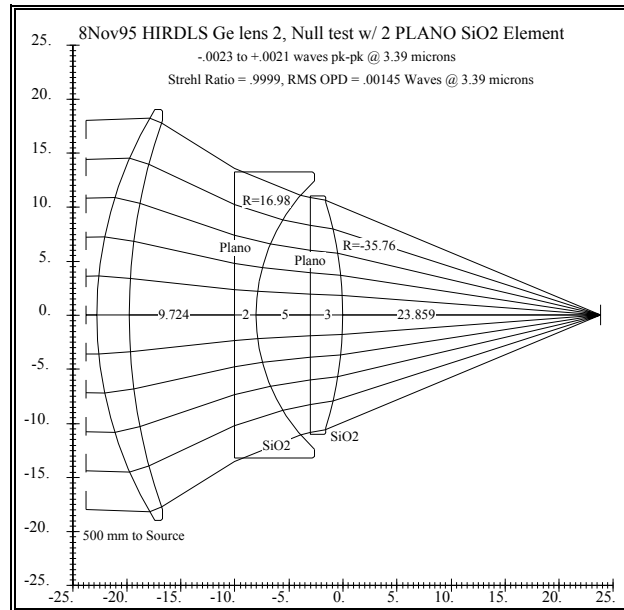


Figure x.x.x A null test for L2 produces excellent results at 3.39 microns

Figure x.x.x below shows the highly corrected wavefront produced by the null test for L2.

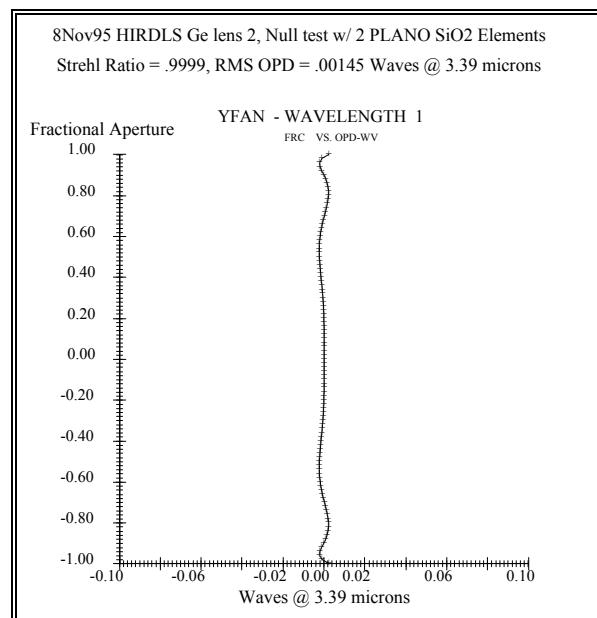


Figure x.x.x The null test for L2 gives nearly a perfect wavefront at 3.39 microns

14.6 The Space View toroid relay mirror

A simple center-of-curvature test would show a severely astigmatic image, but possibly could be done with a Foucault knife-edge test along each of the astigmatic image lines.

A null test at a corrected optical center-of-curvature has been designed for this mirror. The correction is accomplished by a pair of tilted plates which compensate for the astigmatism of the toroid and, being oppositely tilted, introduce no coma into the image. The configuration is shown in figure x.x.x below.

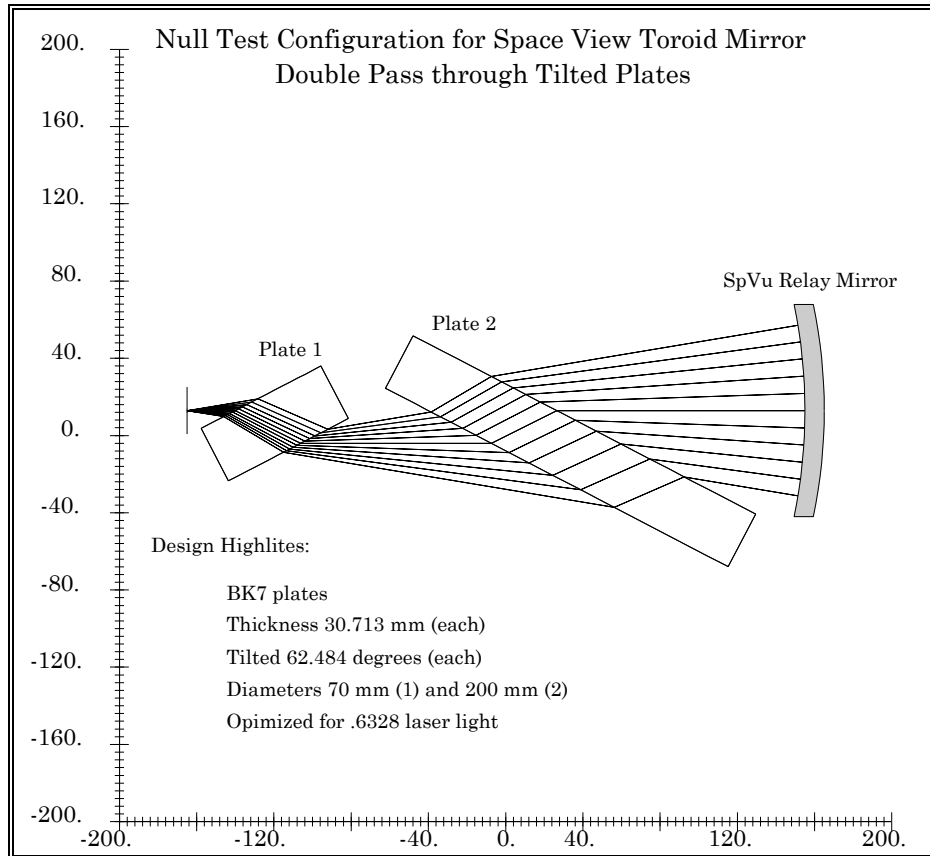


Figure x.x.x Null test configuration for the toroid relay mirror

The plates have identical thicknesses (30.713 mm) and equal tilts (62.484 degrees). Their locations in the space between the source and the mirror is arbitrary. The source is centered on the mirror even with the plates in place.

Image quality is more than adequate given the purpose of this relay mirror, and the image is coma-free and low aberration over a substantial field. Thus the source and image can be safely separated up to ~10 mm.

Over most of the 10 mm field, the image at .6328 (the design wavelength) has an RMS diameter of ~0.030 mm, 3- σ diameter of ~0.054 mm, and full diameter of ~0.080 mm. The system is well behaved even in white light which does not contain deep blue.